Towards a Reliable Fatigue Life Prediction in Metallic Crack Patching

Ansätze für die zuverlässige Abschätzung der Lebensdauer geklebter Pflaster aus Faserkunststoffverbunden zur Reparatur von Ermüdungsrissen in metallischen Bauteilen

Von der Fakultät für Maschinenwesen der Rheinisch-Westfälischen Technischen Hochschule Aachen zur Erlangung des akademischen Grades einer Doktorin der Ingenieurwissenschaften genehmigte Dissertation

vorgelegt von

Ulrike Silke Martens,
geb. Schlauch

Berichter:	Univ.-Prof. Dr.-Ing. Kai-Uwe Schröder
	Prof. Dr.-Ing. Martin Wiedemann
Tag der mündlichen Prüfung:	02.12.2021

Aachener Berichte aus dem Leichtbau
herausgegeben von Univ.-Prof. Dr.-Ing. Kai-Uwe Schröder

Band 4/2021

Ulrike Martens

Towards a reliable fatigue life prediction in metallic crack patching

Shaker Verlag
Düren 2022

Bibliographic information published by the Deutsche Nationalbibliothek
The Deutsche Nationalbibliothek lists this publication in the Deutsche Nationalbibliografie; detailed bibliographic data are available in the Internet at http://dnb.d-nb.de.

Zugl.: D 82 (Diss. RWTH Aachen University, 2021)

Printed in Germany.

ISBN 978-3-8440-8691-1
ISSN 2509-663X

Shaker Verlag GmbH • Am Langen Graben 15a • 52353 Düren
Phone: 0049/2421/99011-0 • Telefax: 0049/2421/99011-9
Internet: www.shaker.de • e-mail: info@shaker.de

Abstract

The topic of "Ageing Aircraft" is one of the big issues in today's operational aircraft. Fatigue cracks for instance are of great concern when looking at old metallic aircraft structures. [1, 2] Increasing the aircraft's operational service life in terms of flight hours and flight cycles is of great interest not inly from a financial point of view. Contemporary demands for sustainability are of great concern in aviation industry. The aim to the delay the replacement of cracked components and to reduce inspection times and effort results in the need for effective and lasting repair methods. Adhesively bonded repair patches made of fibre reinforced polymers (FRP) can restore the component's structural integrity without structural degradation.

Research into metallic crack patching goes back to the 1980s. Since then, effective design methods have been developed and improved to a very high level of accuracy. The majority of today's research still focuses on the general verification of patch efficiency and the improvement of the preliminary patch design methods. But, the actual difficulty is the reliable service life prediction. Cyclic mechanical loading combined with continuously changing environmental influences can significantly detract the repair's functionality over time. Hence, fatigue life assessments using the initial repair properties is limited due to their degrading characteristics. However, a full exploitation of the potential on the other hand can only act up with a reliable fatigue life prediction.

In a comprehensive analysis of the design process the present study reveals effective starting points for prospective research. It shows why additional studies on patch effectiveness cannot lead to improve the reliability of bonded patches. With a coupon test series the theory is supported that the effect of even more precise preliminary patch design methods is insignificant concerning service life extension and that the focus of future studies has to be set on the assessment of service loads and their impact on the structural integrity. To this, a concluding test series shows how the method of infrared thermography enables significant improvements in the comprehension of the fatigue behaviour of a crack patched metallic structure.

Kurzfassung

Im Bereich der Luftfahrt sind alternde Flugzeugflotten und die damit einhergehende Ermüdungsproblematik ein wichtiges Thema. [1, 2] Nicht nur aus wirtschaftlicher Sicht ist die Verlängerung der Einsatzfähigkeit alternder Komponenten von großem Interesse. In Zeiten des immer größer werdenden Bestrebens nach nachhaltigen Lösungen ist das Thema Reparatur aktueller denn je. Der Einsatz geklebter Reparaturpflaster aus Faserkunststoffverbunden kann dazu beitragen, das Wachstum von Ermüdungsrissen in metallischen Bauteilen im laufenden Betrieb deutlich zu reduzieren ohne die Tragfähigkeit der Struktur zu vermindern.
Obwohl bereits seit den 1980er Jahren im Bereich geklebter Reparaturpflaster geforscht wird und effektive Berechnungsmethoden verfügbar sind um ihre Wirksamkeit zu quantifizieren, konzentriert sich der Großteil aktueller Studien immer noch auf den Nachweis der generellen Wirksamkeit oder der Verbesserung der Vorauslegung. Die eigentliche Problematik liegt jedoch in der zuverlässigen Abschätzung der Betriebsdauer. Zyklische mechanische Beanspruchungen sowie stetig wechselnde Umwelteinflüsse führen dazu, dass die Funktionsfähigkeit des Pflasters mit der Zeit abnimmt. Die ursprünglich ermittelte Reduktion der Spannungsintensität an der Rissspitze ist im Einsatz also nicht dauerhaft gültig und daher nur bedingt nutzbar um die tatsächliche Lebensdauer vorhersagen zu können. Die vollständige Ausschöpfung des Potenzials geklebter Reparaturen gelingt jedoch vor allem dann, wenn das Langzeitverhalten verlässlich und sicher vorhergesagt werden kann.
In einer umfassenden Analyse des Auslegungsprozesses zeigt die vorliegende Arbeit auf, wo weiteres Forschungspotenzial zu finden ist. Anhand einer praktischen Laborstudie wird die These untermauert, dass durch eine noch genauere Vorauslegung kein essentieller Beitrag dazu geleistet wird, die tatsächliche Einsatzsdauer zu erhöhen, sondern der Fokus weiterer Studien auf die Abschätzung realer Belastungen und ihrer Folgen gelegt werden sollte. Hierzu wird in einer abschließenden Testreihe gezeigt, wie mit Hilfe der Infrarotthermografie das Schädigungsverhalten unter dem Pflaster unter zyklischer Belastung visualisiert werden kann. Die Möglichkeit Risswachstum und lokale Schädigungen in der Klebefuge zeitgleich beobachten zu können, trägt dazu bei, das Verständnis des Langzeitverhaltens im Einsatz zu erhöhen.

Contents

1 Adhesively Bonded Aircraft Repair

During operation, an aircraft is exposed to multiple different loads. With continued aircraft use the relevance of wear and deterioration increases, embraced by the term "Ageing Aircraft". Ageing effects comprise a number of degradation processes such as material fatigue, corrosion, wiring degradation, increased wear/deterioration rates, reduced aerodynamic and system performance or similar [3, 4]. Fatigue is one of the most prevalent ageing effects resulting from frequent aircraft use. Small cracks caused by the load history grow due to cyclic loading and detract the structural stiffness. Common crack starters are sharp corners or holes. A crack repair can sizeably prolong the operational lifetime of cracked components. Conventional riveted or bolted metallic doublers weaken the already detracted load-bearing capacity of cracked components by additional holes. Adhesively bonded patches made of fibre reinforced polymers can significantly enhance the fatigue life of such components without further structural impairments. Theoretically, it is even possible to completely restore the structural integrity with bonded patches and to thereby prevent further crack growth. In practice, conventional repairs are still the preferred solution even though patch repairs can perform better. This is caused by the poor failure predictability of bonded patches. The best repair solution is worthless as long as its performance cannot be estimated reliably.

1.1 Maintenance Requirements

In the early years of aircraft design, fatigue cracking was not considered in the design process. A variety of severe failures in operational aircraft caused by fatigue cracking lead to the conclusion that, that apart from static properties also the fatigue behaviour has to be taken into account. The actual service

life often considerably exceeds the aircraft's designed nominal life and the continuous exposure to atmospheric pressure and service loads make cracks even more dangerous. The fact that fatigue cracking cannot completely be prevented, even when considered in the design process, results in different design philosophies. These philosophies partly include, that even damaged or cracked structural components need to withstand service loads. [5]

Safe life refers to structural parts, that are designed to be safe against failure. After a predefined service period, the parts are replaced, whether cracks occurred or not. Parts designed in accordance with the safe life philosophy are usually statically determined, so that failure cannot be compensated.

Fail safe corresponds to structural parts, which are designed with a redundancy against failure. These parts need good accessibility to perform necessary maintenance measures and in the case of significant damages to be easily replaceable.

Damage Tolerant design tolerates damages in structural parts to a certain degree. These parts need good maintainability, so that damages can be detected, before they reach a critical size.

Flaw tolerant safe life philosophy accepts defined flaws in structural parts, as long as they do not grow during the predefined service life. [5]

In order to ensure the aircraft's airworthiness, the decrease of structural load-bearing capacity is countered by periodic maintenance activities. Compulsory periodic inspections, the so-called "maintenance checks" or "letter checks" are common practice. In particular the UK Aerospace Maintenance, Repair, Overhaul & Logistics Industry (MROL) [6] defines these letter checks as follows:

A-check "This check is carried out approximately every 80 to 100 aircraft flight hours, which is every 7 to 9 days. It needs about 10 to 20 man-hours and is usually performed overnight while the aircraft is at the gate or in a hangar."

B-check "The B-check is a more thorough maintenance check and is normally carried out every two months (approximately 500 to 600 aircraft flying hours). This maintenance is carried out in a hangar and requires approximately 100 to 300 man-hours depending upon the size and complexity of the aircraft."

C-check "The C-Check is very thorough and comprehensive. Virtually the entire aircraft goes through an exhaustive series of checks, inspections and overhaul work. The C-Checks typically occur every two years and require 10,000 to 30,000 man-hours, depending on the aircraft type and take two to four weeks to complete."

D-check "This check is the most comprehensive and occurs approximately every 6 years. It is a check that, more or less, takes the entire airplane apart for inspection and overhaul. Such a check can usually demand up to 50,000 man-hours and it can generally take up to 2 months to complete, depending on the aircraft and the number of technicians involved. It must be performed at a suitable maintenance base."

Schedules vary depending on the airliner and aircraft type. Every maintenance check leads to aircraft downtime which is always costly. Cracks typically arise from holes or sharp corners due to periodic loading and unloading. Big temperature differences and other environmental influences can further detract the aircraft from structural integrity. Repair measures can be time-consuming and thereby costly in terms of lost revenues and aircraft availability. This illustrates the high demand for cheap and flexible repair solutions in order to reduce aircraft downtimes. According to the MROL the overall maintenance costs of an aircraft amount to 13 % of the entire operating costs (as a comparison: overall fuel account for 17 %). [6] Significant differences in "inspection, damage assessment, and repair requirements" [7] can be found between components from different structural classes. Structures are classified into three categories:

Primary structure is "a structure that is critical to the safety of the aircraft".

Secondary structure refers to "a structure that, if were to fail, would affect the operation of the aircraft but not lead to its loss".

Tertiary structure corresponds to "a structure in which failure would significantly affects the operation of the aircraft". [7]

Demands for repair solutions are manifold and have to be chosen situationally. Depending on the class of the component and the severity of the crack, repair measures vary from drilling out the crack tip and local stiffening of the structure to the replacement of the entire component. For fatigue cracks it is common practice to use mechanically fastened (riveted or bolted) metallic doublers that restore the component's structural integrity after removing the

damage. This procedure is well established and its mechanical performance has a good reproducibility and also predictability. But, as rivet or bolt holes can on the other hand act as crack starters themselves, this procedure also leads to a weakening of the parent structure concerning its fatigue life. [7] Further, depending on the geometry of the region to be restored, the doubler needs to be geometrically fit to the curvature of the metal structure. As an alternative "the use of bonded composite doublers offers the airframe manufacturers and aircraft maintenance facilities a cost-effective method to safely extend the lives of their aircraft." [8] Compared to metallic repairs, one of the main advantages is the flexibility of the uncured patch that facilitates the application to curved structures. Furthermore, compared to conventional methods using bolted or riveted doublers, there is no additional weakening of the parent structure caused by additional drilled holes and the load is transferred over the entire bonded region, whereas for mechanically fastened patches loads are transferred locally. Also the good stiffness to weight ratio of FRP patches results in a minor material requirement. [7] Successful applications in civil engineering, marine industry and military aircraft exhibit the great potential of this technology. [7, 9, 10, 11, 12] The major disadvantage on the other hand is the poor predictability of the patch performance under service conditions, compared to the conventional method.

1.2 Service Conditions and Damage Review

The idea of metallic crack patching goes back to research from the 1980s and since then has continuously improved over time. [2, 13, 14] The system of a bonded patch repair can basically be divided into three components, see Fig. 1.1.

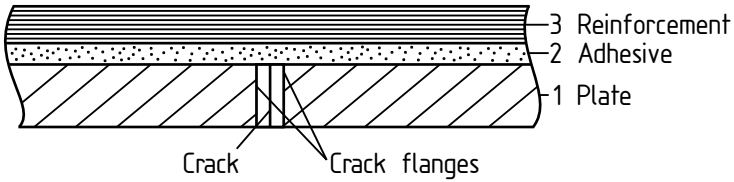

Figure 1.1: Components of a crack patched structure shown in a lateral cut

These components are:

1. Parent cracked metallic structure, denoted with “P”,
2. Polymeric adhesive layer, denoted with “A” and
3. Composite reinforcement, denoted with “R”.

The basic principle of a bonded repair is to reduce the crack growth rate in the cracked component. The bonded patch bridges the crack and thereby reduces the stress at the crack tip, determined by the stress intensity factor K. The stress intensity factor K is a measure for the severity of the crack and determines the crack growth rate. It is proportional to the crack length a. Hence, the reduction of the stress intensity factor K is equivalent to reduced crack growth rates.
Patch functionality is strongly dependent on the bonding strength. As long as the patch is properly bonded to the substrate, noticeable reductions in crack growth rates can be achieved. But, for bonded patches the repeated load cycles and continuously changing environmental conditions cause ageing and material strength degradation over time. For adhesive bondings, predictability becomes more and more difficult with increasing service life. [15] The difficulty to reliably predict the mechanical behaviour of a patch repair under service loads is based in the long-term joint degradation. Degradation mechanisms are usually classified into material, stress and environment based mechanisms. [16, 17] These mechanisms can be summarized as follows:

Material degradation accounts for adherends, adhesive and their interface. [17] Adhesive joints composed of dissimilar components that all exhibit a completely different structural behaviour under service loads result in complex stress states. [18]

Stress degradation is most critical under cyclic and mixed-mode loading. [17] The mechanical behaviour is dependent on the stress state, which is the stress ratio R for cyclic loading. The fatigue behaviour of a metallic material differs significantly from the one of a polymeric material such as FRP or polymeric adhesives. Even if the polymeric matrix of the composite can have comparable characteristics to the adhesive, the presence of reinforcing fibres leads to major differences in the mechanical behaviour.

Environmental degradation is caused by different aspects such as temperature changes, moisture, thermally induced residual stresses and many

more. [19, 17] Environmental mechanisms that are considered to be most prominent in joint degradation are temperature changes, moisture and water. [20, 17] For polymers, the effect of the temperature dependency and environmentally conditioned ageing is much stronger than for metals. Additionally, cyclic thermal loading of multi-material joints result in complex stress states due to different coefficients of thermal expansion. [21] Degradation of adhesive joints due to moisture is composed of physical, chemical and/or mechanical processes which all can result in catastrophic bond failure. [22]

The joint quality is further dependent on the surface preparation and the joining process. The application of an additional primer can lead to increased bonding performance for instance. Due to viscoelasticity, especially the properties of polymeric materials can change significantly over time.
Degradation includes more than the material strength reduction. Next to the metallic crack growth, other damage mechanisms can occur. Possible damages are summarized in Fig. 1.2.

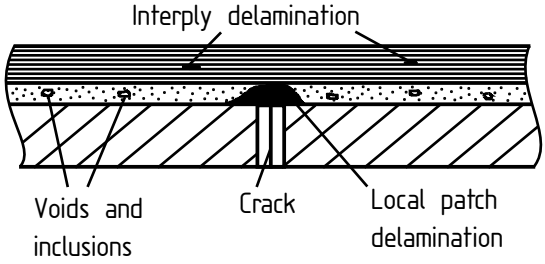

Figure 1.2: Possible damage mechanisms of a crack patched structure shown in a lateral cut

Small damages in the adhesive like inclusions or voids can result from the joining process and might expand during loading. The same applies for the patch, resulting in local (inter-ply) delamination. Here, place and size of the delamination is responsible for the severity of the damage. Local patch delamination in the middle part around the crack might lead to increased crack growth rates, but do not directly result in sever damage. Delamination from the patch boundary in contrast can lead to severe patch detachment. [23]

1.3 Service Life Determination

The useful time of engineering components is directly linked to the component's reliability. The term "engineering reliability" is defined to be "the probability that an item will perform a required function without failure under stated conditions for a stated period of time." [24] This approach tries to give a "time-based concept of quality" for engineering products that are likely to fail. The application of conventional reliability engineering onto the engineering system of bonded patches enables the identification of starting points for improvement measures with respect to a possible service life extension. Classical reliability engineering considers a product's reliability to be a major parameter of the operational life, measuring its quality over time. Failure prediction is difficult since it is always based on assumptions and thus prediction quality is directly depending on the assumption quality. "Reliability is therefore an aspect of engineering uncertainty" and thus is a question of probability. [24] In the context of metallic crack patching this means that the desired increase in reliability has to go along with a decrease in the number of uncertainties.
A more illustrative approach is the so-called "bathtub curve", depicted in Fig. 1.3. The curve shows the hazard rate over time for the product's life-

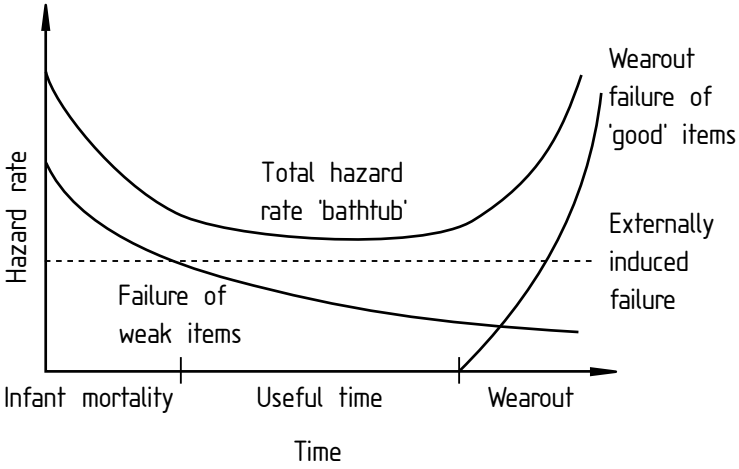

Figure 1.3: The "bathtub curve" in reliability engineering [24]

cycle. It is mainly divided into three parts – the time of infant mortality, or

infancy, the useful time and wear-out. The beginning of a product's life-cycle can be described by decreasing the hazard rate. Failure during infancy usually occurs due to a poor design, problems in manufacture or material flaws. The middle part is characterised by a more or less constant hazard rate. Here, failure is caused by overloading, or similar which usually occurs randomly. In contrast, the end of the product life-cycle is described by an increasing hazard rate and wear-out effects determine the failure behaviour. [24, 25] It has to be noted, that the curve describes only the probability of failure. Ageing effects that have not yet lead to failure are not considered. [25] Material fatigue is normally located in the wear-out phase. To increase reliability, the middle part of useful time needs to be strengthened.
Concluding, the useful time of a product's life-cycle can be increased by decreasing the number of uncertainties. Precisely, this can either be achieved by moving the transition between infant mortality and useful time forward or by delaying the beginning of the wear-out phase, or even both at the same time. The question to be answered is, at which point in the patch design process starting points for possible improvements can be found.

1.4 Thesis Scope Definition

The goal within this thesis is to identify and present new opportunities to increase the service life of a bonded patch repair and is approached as follows:

1. **Analysis and breakdown of the patch design process**
   Based on a direct comparison of the general fatigue design process with the one for patch repairs possible pitfalls are identified and a general design process specifically for bonded repair patches is proposed. A clear distinction between the initial patch design on the one hand and the prediction of patch performance on the other is proposed. This distinction provides the framework requirements for the for the following studies (see Chapter 2).

2. **Assessing the patch design process and prediction methods**
   The first of the two practical analyses focusses on the **patch design process**. The analysis focusses on the question whether or not or rather at which point the classical fatigue life prediction methodology has to be reassessed. In an exemplary coupon test series the fatigue life prediction quality for patched components using conventional methods is evaluated (see Chapter 3).

3. **A possibility to improve performance predictions**
   The second practical analysis focusses on the **performance prediction**. In order to decrease uncertainties in the performance prediction the method of infrared thermography is presented as a method that is able to give shape and form to the continuous damage processes of a patch repair: Patch delamination and crack growth can be monitored at the same time. This is a great step forward in the targeted analysis of damage processes which in return can be used to enhance damage controllability and thereby to redefine patch wear-out (see Chapter 4).

4. **Conclusion and outlook**
   Concluding, all fundamental findings are summarized and continuative research fields are pointed out. One decisive question is the continuous damage observation during service, that rounds off the understanding of the entire damage process. A promising methodology that assembles patch and sensor is introduced (see Chapter 5).

2 Analysis and Breakdown of the Overall Patch Design Process

From the beginning of patch design the focus has been set on the determination of the stress intensity factor of crack patched components K^*. Calculation methods – both, analytical and numerical – continuously improved over time. But, even today's research still deals with comparable topics: Numerous studies can be found that confirm the general efficiency of bonded patches for a specific repair configuration, prove the quality of the analytical models, or try to further optimize the initial patch design. [26, 27, 28, 29, 30] These studies deal with the determination of the initial stress intensity factor K^* and mainly compare results on coupon test level under ideal conditions without taking service loads and degradation into account. In total, findings seem to stay on an academic level and cannot achieve the increase in reliability needed to really advance the topic of crack patching. In order to find out possible starting points for improvements, the entire patch design process is therefore analysed with respect to possible weak points.

2.1 The Fatigue Design Process

The general fatigue design process is based on fatigue crack propagation in metallic components. Adaptions for other materials are possible. A short introduction into the principles of fatigue design helps to arrange the process steps needed for the fatigue design of crack patched components.

2.1.1 Linear Elastic Fracture Mechanics and the K-Concept

The term "fracture mechanics" comprises the so-called linear elastic fracture mechanics LEFM and the plastic fracture mechanics (PFM) approach. Based

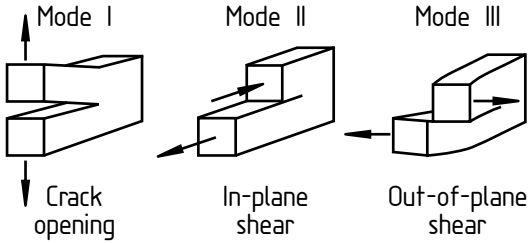

Figure 2.1: Loading modes that enable a crack to propagate [32]

on the predominant material behaviour – linear elastic or plastic – different concepts to describe the damage progress can be found. Since fatigue cracks grow at stresses below the static allowable stress values, plastic deformation zones are comparably small and the LEFM approach is commonly used. [31] Also for crack patching the K-concept is used to describe the impact of the patch on metallic crack growth. [2]
Fracture mechanics is a broad field. To restrict this summary to the important information needed here, a few assumptions have to be made:

- The metallic part is flat,
- the metallic part is thin-walled,
- only in-plane loads are applied,
- cracks are loaded only in mode I-direction (crack-opening),
- the reinforcing patch is only loaded in tension,
- local plasticity at the crack tip is small (K-concept)
- fatigue loads with constant amplitude are applied and
- crack closure concepts are not taken into account.

Crack opening modes are classified depending on the three principal load directions, see Fig. 2.1. “Mode I” describes tension loading (crack opening), “mode II” stands for in-plane shear mode and “mode III” represents the out-of-plane shear mode. Mixed-mode loadings are possible. In the following, only mode I loading is considered, because crack opening is the most severe mode for fatigue crack growth. [1]

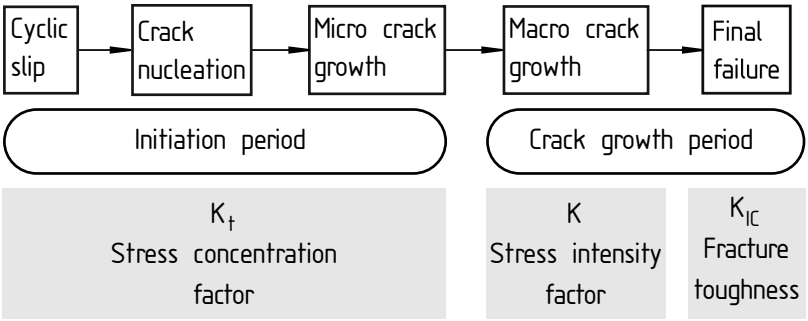

Figure 2.2: Different phases of the fatigue life and relevant K_I factors [1]

Depending on the crack size, the K-concept comprises different K_I values, see Fig. 2.2. During crack initiation crack size is on a micro scale. In the initiation period, the factor that describes the severity of the crack is the stress concentration factor K_It. The crack growth period is defined for cracks on macro scale. Here, the stress intensity factor K_I is used to determine the crack growth behaviour. The fracture toughness K_IC is a material property that defines the transition between stable crack growth and abrupt final fracture. For a patch repair, the crack is already on macro-scale, so the interesting factor is the stress intensity factor K_I that describes the stable crack growth rate.
The stress intensity factor is a geometry and load based factor that allows for the assessment of crack growth rates. The stress intensity factor is dependent on the crack size, location and geometry as well as on the crack opening mode and the load magnitude. [1] It describes the intensity of a crack without giving any information on stress or displacement distributions in the surrounding area. [31] For a cracked plate loaded in mode I, the stress intensity factor can be determined using

$$K_\mathrm{I} = \sigma Y_\mathrm{I} \sqrt{\pi a}, \tag{2.1}$$

where σ denotes the stress, a is the crack length and Y_I is a dimensionless geometry factor. [1] So far, Eq. 2.1 refers to quasi-static loading conditions. Fatigue loads with stresses varying between the values σ_min and σ_max can be considered replacing σ with $\Delta\sigma = \sigma_\mathrm{max} - \sigma_\mathrm{min}$, which leads to the dynamic stress intensity factor

$$\Delta K_\mathrm{I} = \Delta\sigma Y_\mathrm{I} \sqrt{\pi a}. \tag{2.2}$$

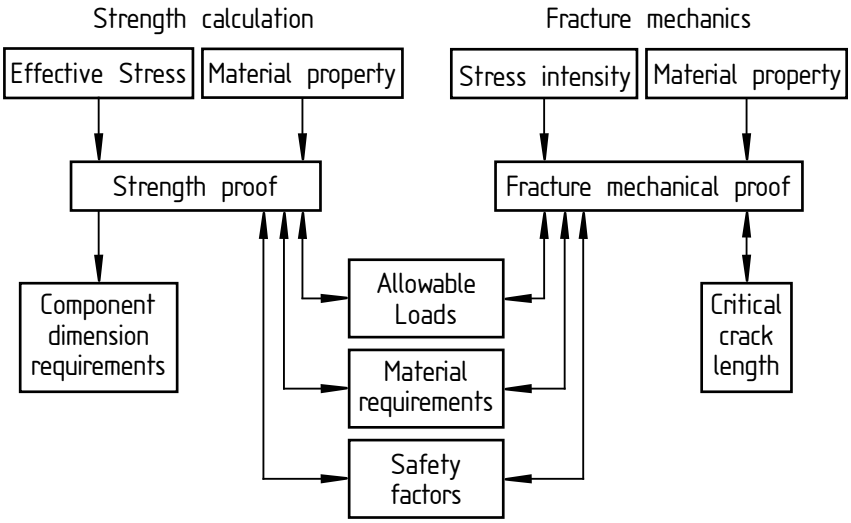

Figure 2.3: Schematic design procedure combining fatigue strength and fracture mechanical proof according to [31]

2.1.2 The Preliminary Design Process

The fatigue design process aims at the prevention of crack initiation. The process is usually composed of two parallel process steps – the fatigue strength proof and the crack growth assessment, see Fig. 2.3. Strength proof calculations show that under the given loading conditions, the component is not critical for fatigue cracking. Should fatigue cracks occur nonetheless, the fracture mechanical proof provides a method to identify the critical crack length. For aircraft components there is no standardized maximum allowable crack length. The critical length is defined individually. [33] For the assessment of crack endangered components both procedures are essential. Together, necessary design requirements on material properties, component dimensions, allowable loads, safety factors and the critical crack length can be identified.

2.1.2.1 Strength Proof

In principle, effective stresses are calculated based on geometry and load assumptions before they are compared with the allowable stress determined

by the material used $j\,\sigma_{\text{applied}} \leq \sigma_{\text{allowable}}$. The factor j is a safety factor that has to be chosen according to the application. [31] For a design that complies with this relation, fatigue crack is unlikely to occur.

2.1.2.2 Fracture Mechanical Proof

When a component fulfils the strength proof, a fracture mechanical proof has to be made in order to assess the fatigue life of the component if a crack occurs even though crack initiation was unlikely to occur. Remembering that a patch repair applies for cracks on macro-scale, the fracture mechanical proof will be crucial for the preliminary patch design as well.
The characteristic value for crack assessment, is the stress intensity factor K_{I}. For a given design (geometry, material etc.) it can be determined by using Eq. 2.2. In parallel, based on a fracture mechanical laboratory test, material constants such as the material fracture toughness K_{IC} can be determined. Similar to the strength proof, the allowable stress intensity factor $K_{\text{I,allowable}}$ results from the relation $j\,K_{\text{I,allowable}} \leq K_{\text{IC}}$. The general procedure is shown in Fig 2.4. With the fracture mechanical proof critical loads, the critical crack size, material strength requirements and the safety factor against leaving the stable crack growth regime can be determined. [31]

2.1.3 Performance Prediction

In the preliminary design process, it is the goal to design a component in a way that fatigue loads are not critical and that if a fatigue crack occurs nonetheless, crack growth is in a non-critical stable crack growth regime. Spotting a fatigue crack during maintenance activities requires the assessment of the remaining fatigue life of the cracked component. Now, not only stress intensity, also the resulting crack growth rates have to be assessed. At this point, actual service conditions have to be considered.
For the performance prediction of a cracked component under service loads, crack growth rates need to be rated. The crack growth rate is determined by the relation between the crack length a and number of load cycles applied N. With increasing crack length, the crack growth rate also increases. This can be explained with the linear relationship between the stress intensity factor K_{I} and the crack length a. [1] Plotting crack length a vs. number of load cycles N, as shown in Fig. 2.5, the crack growth rate can be evaluated as the curve gradient $\mathrm{d}a/\mathrm{d}N$.

As a measure of stress intensity, K_{I} is directly linked to the crack growth

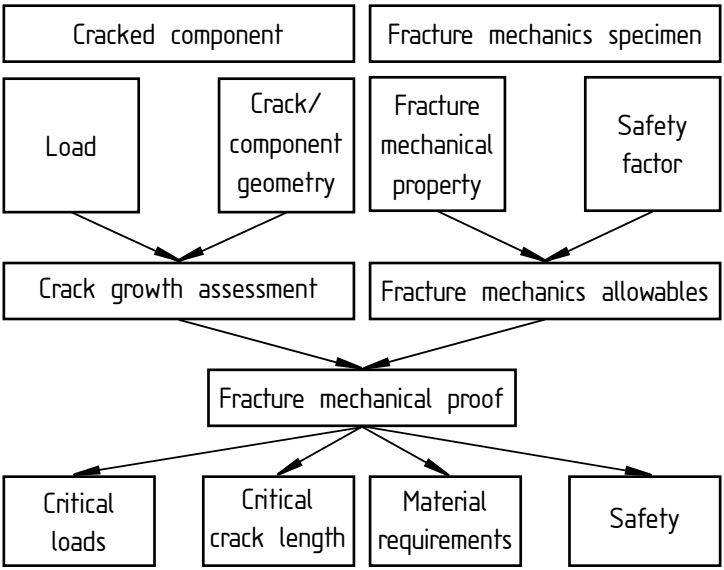

Figure 2.4: Schematic procedure of the fracture mechanical proof according to [31]

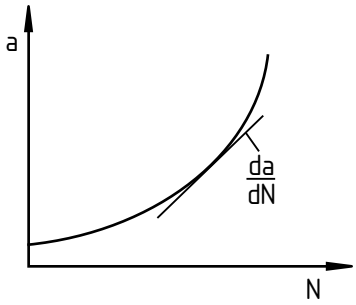

Figure 2.5: Crack length a versus number of load cycles N

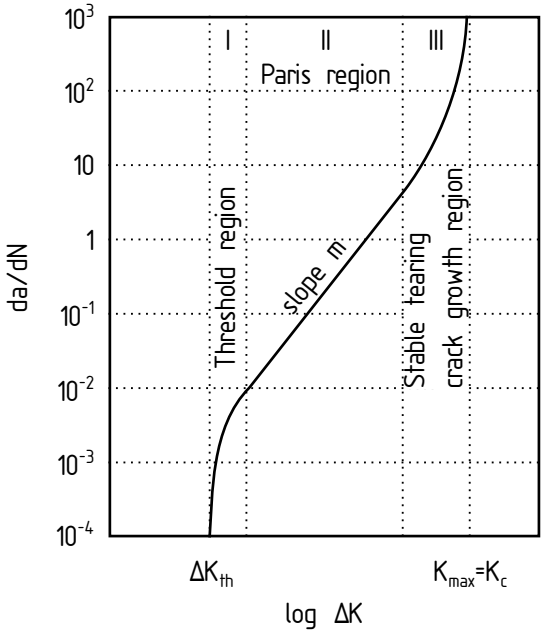

Figure 2.6: Three regions of crack growth rates as a function of ΔK [1]

rate $\mathrm{d}a/\mathrm{d}N$. The three regions of crack growth, presented in Fig. 2.2, can be illustrated in a double log plot of $\mathrm{d}a/\mathrm{d}N$ vs. ΔK_I, see Fig. 2.6. The three regions are

i the threshold region,

ii the Paris region for stable crack growth described by the stress intensity factor K_I and

iii the stable-tearing crack growth region for cracks that cannot further be described by stable crack growth.

The threshold value ΔK_th describes macroscopic cracks for which the stress intensity is too low to cause crack growth. [1]
For metallic crack patching, the region of interest is the stable crack growth region, also called “Paris region”. It can be described using the so-called

"Paris law". The Paris law is described by the power function

$$\frac{\mathrm{d}a}{\mathrm{d}N} = C\Delta K_{\mathrm{I}}^{m}. \tag{2.3}$$

Here, C and m are material constants. Substituting the function for the stress intensity factor K_{I} as given in Eq. 2.2, the Paris region can be described by

$$\frac{\mathrm{d}a}{\mathrm{d}N} = C(Y_{\mathrm{I}}\sqrt{\pi a})^{m}\Delta\sigma^{m}. \text{ [1]} \tag{2.4}$$

Other approximations describing the stable crack growth region can be found, but not evaluated.
Being able to describe the crack growth rate also enables us to determine the remaining fatigue life of a cracked component, provided that geometry, material properties and load assumptions are available. The value of interest is the number of load cycles N that can be applied before a crack of initial length a_{initial} reaches a predefined critical crack size a_{critical}. Here, two factors are required – the crack growth resistance $\mathrm{d}a/\mathrm{d}N = f(K)$ and the crack driving force described by $K_{\mathrm{I}} = f(a)$. It needs to be mentioned that even though there are well-established methods for metallic materials, the prediction accuracy is limited. [1] Paris law is a well-established possibility to describe the crack growth rate $\mathrm{d}a/\mathrm{d}N = f(\Delta K, R)$. Results are rated to be rather conservative. [31] Integrating of Paris law within the crack length boundaries a_{initial} and a_{critical} now gives the number of remaining load cycles. As Paris law (and also other comparable methods) use the assumption of a constant geometry factor to approximate the crack growth behaviour, in practice this approach is quite inaccurate and not recommended to be used. Instead, a numerical integration is suggested. [31]
For the numerical integration the following equation applies

$$N_{\mathrm{remaining}} = \Sigma N_{\mathrm{part}} = \Sigma\frac{\Delta a_{\mathrm{part}}}{(\mathrm{d}a/\mathrm{d}N)_{\mathrm{part}}}. \tag{2.5}$$

The correlation between crack growth $\Delta a_{\mathrm{part}}/(\mathrm{d}a/\mathrm{d}N)_{\mathrm{part}}$ and the remaining number of load cycles N is plotted in Fig. 2.7. As can be seen, the $1/(\mathrm{d}a/\mathrm{d}N)$ vs. a curve can be divided into equal intervals of width Δa_{part}. The sum of all life cycles between the two boundary values a_{initial} and a_{critical} is the approximate remaining fatigue life. [31]

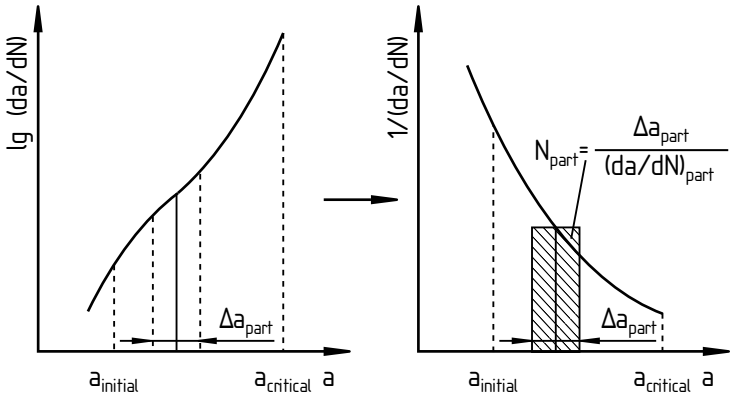

Figure 2.7: Numerical integration of the fatigue life between a_{initial} and a_{critical} [31]

2.2 Theory of Crack Patching

The use of adhesively bonded repair patches can significantly enhance the fatigue life of a cracked component. The bonded patch effectively reduces stresses at the crack tip and thereby also crack growth rates resulting in an increased fatigue life. Here, a proper patch design is significant for the effective stress reduction. The driving force for crack growth is the stress intensity at the crack tip which can be described by the stress intensity factor K. Considering a centre cracked plate loaded perpendicular to the crack, the increase in stress at the crack tip can be illustrated, see Fig. 2.8. The dotted lines show stress trajectories which represent the load paths through the component. The stress has to circle the crack which results in a local stress concentration at the crack tip. It applies that larger cracks lead to a bigger crack opening than short ones, which further increases the stress peak. The higher the stress peak, the faster the crack growth. The stress intensity factor is a measure of the crack growth rate and as a function of crack length a it increases with increasing crack length.
The application of a bonded patch now reduces the stress peak at the crack tip and thereby also the stress intensity factor K. The reduction of K is the relevant aim of crack patching. [34] Thus, the determination of the stress intensity factor for the crack patched component is crucial for the patch design process. The crack in the parent metallic structure has to be covered completely by the FRP patch, see Fig. 2.9. The application of a patch that

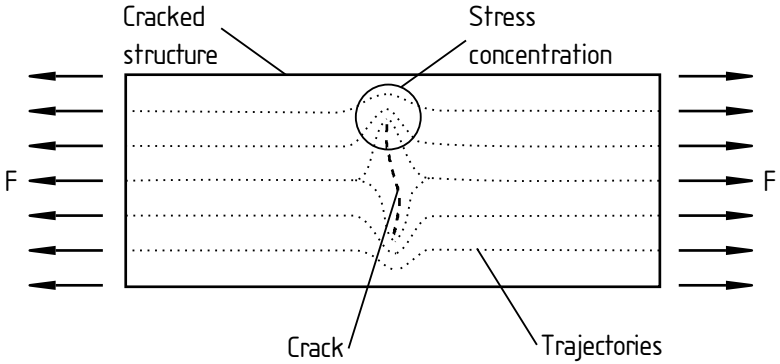

Figure 2.8: Load distribution in a cracked structure

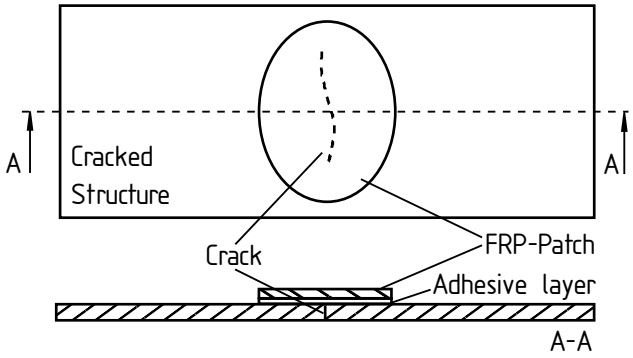

Figure 2.9: Composition of a crack patched component

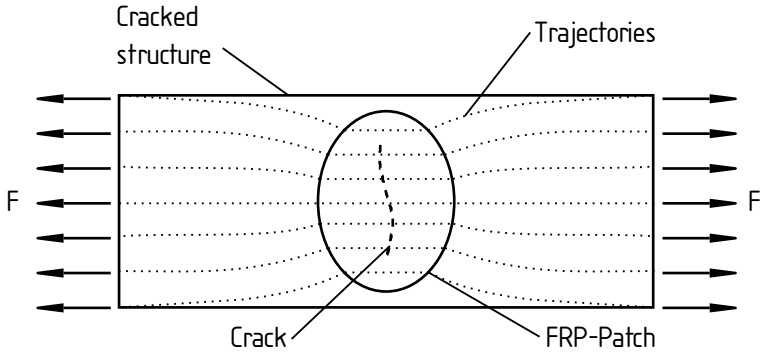

Figure 2.10: Load redistribution through the patch [35]

increases the local stiffness, also called doubler, leads to a stress redistribution. The increased local stiffness attracts the loads, as illustrated in Fig. 2.8. The patch does not only attract the loads, it also bridges the crack which means that load is transferred through the patch and thereby over the crack. This results in a stress peak reduction at the crack tip. Furthermore, the stiff patch holds the crack flanks together, which results in smaller crack opening angles and thus in yet another reduction of the load impact on the crack tip. Crack patch theory even promises the possibility of entirely restoring the component integrity when ideal conditions can be met.
Remembering the components of a crack patched structure, as shown in Fig. 1.1, the adhesive layer is in fact comparably thin with respect to the metallic component and the patch, but it has a major function. It is not only responsible for joining the components, it acts as an expansion gap between them. Even though crack opening is reduced by the patch, the displacement of the crack flanks in the parent structure is noticeably bigger than the expansion of the comparatively stiff FRP patch. In order to make sure the patch does not simply peel off, the difference in strain needs to be compensated by the adhesive. A detail drawing of the lateral cut is shown in Fig. 2.11. A comparison of the unloaded and the loaded structure illustrates the load transmission from the metallic plate into the patch via the adhesive layer. The high shear deformation of the adhesive can be seen as well as the impulse to out-of-plane bending caused by eccentricity due to single-sided patch application. For simplicity reasons, out-of-plane bending is neglected in the derivation of K. [2] Additionally, safety factors that display the reduced ef-

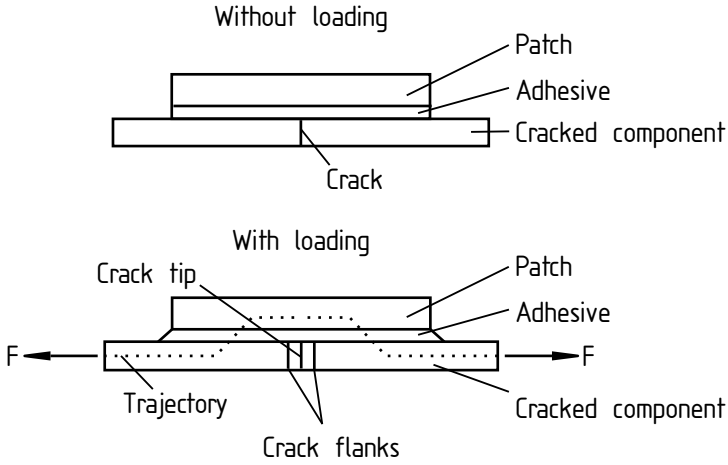

Figure 2.11: Load transmission through the adhesive layer

ficiency caused by single-sided repairs compared to symmetrical ones can be applied. [35]
The patch area can be divided into different "regions [...] of structural integrity requirement". [36] The inner zone close to the crack is assigned to be "damage tolerant" as local disbonds do not have a major impact on metallic crack growth and the damage growth is "slow and stable". [36] The tapered patch boundary on the other hand is correlated to the "safe life" principle, since disbonds grow into regions of increasing patch thickness, which goes along with increasing patch disbond. These two zones are illustrated in Fig. 2.12. To analyse the adhesion properties of the patch repair, literature proposes one representative specimen configuration for each zone – the double overlap-joint fatigue specimen (DOFS) for the damage tolerant zone around the crack and the skin doubler specimen (SDS) for the tapered edges, see Fig. 2.13. [36] As out-of-plane bending is neglected in the first approximation, the specimens represent the double-sided symmetric repairs, see Fig. reffig:representativespecimens.

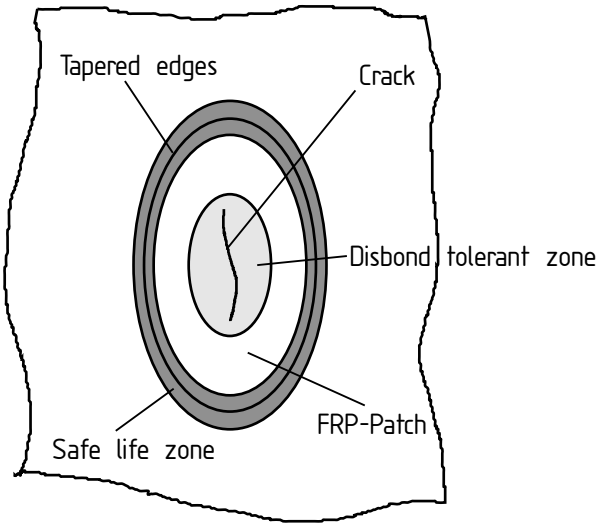

Figure 2.12: Damage tolerant and safe life zone in the adhesive zone of a patch repair, as proposed in [36]

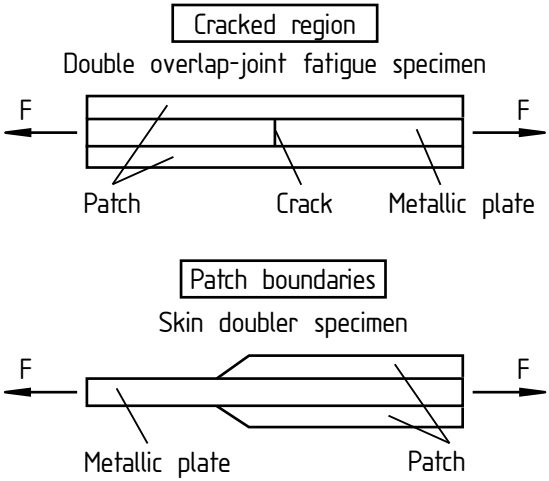

Figure 2.13: Specimens representing the damage tolerant zone around the crack and the safe life zone at patch termination [36]

2.3 The Fatigue Design Process of Bonded Patches

Service loads can cause a number of different failure mechanisms in crack patched structures. A proper fatigue design considers all possible damages, which are:

1. metallic crack growth,
2. damage in the parent structure at the patch boundaries,
3. patch fatigue,
4. shear failure in the adhesive and
5. patch peel off, caused by peel stresses in the adhesive.

The type of damage depends on the individual load history and might vary for repairs of other structures. [37] As in the general fatigue design, also for a patch repair "the design approach [...] must include two major aspects: (a) design of the patch to achieve acceptable reduction in stress intensity and consequently an acceptable rate of crack growth in the parent structure under the service loading, and (b) prediction of fatigue durability of the patch system, based on estimated loads.
To achieve (a) the available design models, based on analytical or finite element (FE) procedures can provide an assessment of (i) reduction in stress intensity in the case of cracks and (ii) stresses in the patch and adhesive.
The requirement to achieve (b) is a generic fatigue database for the patch or reinforcement system which is valid over a range of similar geometries and environmental conditions (moisture absorption and temperature) to the specific repair." [38] These two major aspects (a) and (b), as stated by Baker et al. correspond to the process steps "preliminary design" and "performance prediction" as already described for the general fatigue design process (see 2.1).

2.3.1 The Preliminary Design Process of Bonded Patches

The general preliminary fatigue design targets at reducing the probability of crack initiation in the best possible way. For a patch repair, the component is

already cracked. The intention here is to design a repair that reduces crack growth effectively. Again, both the strength proof as well as the fracture mechanical proof have to be performed.

2.3.1.1 Strength Proofs for Bonded Patches

In the first step of the preliminary design process, fatigue strength of the patch system has to be proven. The strength proof procedure, as described for the general fatigue design process, has to be employed for all critical areas, which are:

- normal stresses in the parent structure around the patch $\sigma^{\mathrm{P}}_{\mathrm{max}}$,
- normal stresses in the patch $\sigma^{\mathrm{R}}_{\mathrm{max}}$,
- shear stresses in the adhesive $\tau^{\mathrm{A}}_{\mathrm{max}}$ and
- peel stresses in the adhesive $\sigma^{\mathrm{A}}_{\mathrm{max}}$.

Analytical formulas to determine the effective stresses in a patched component can be found in the relevant literature, see for instance [35, 39, 40].

2.3.1.2 Fracture Mechanical Proof for Bonded Patches

The fracture mechanical proof makes use of the K-concept, which therefore has to be adapted for bonded patches. Basically, the initial formula of the stress intensity factor, Eq. 2.1, is also valid for the crack patched structure. The only difference is, that a reduction factor θ has to be added. The stress intensity factor K^*_{I} of a repaired structure then has the general form

$$K^*_{\mathrm{I}} = \theta\,\sigma\sqrt{\pi a}. \tag{2.6}$$

The stress intensity factor K^*_{I} can generally be determined using the superposition principle, see [32]. The determination of K_{I} in the two-stage approach according to Rose's model for symmetric and single-sided repairs, as described in [35], combines the superposition principle with the inclusion analogy. A definition of the different variables used in Rose's method are depicted in Fig. 2.14. The origin of the coordinate system is positioned in the centre of the crack of length $2a$ with the x-axis parallel and the y-axis perpendicular to the crack expansion direction. Maximum patch dimensions

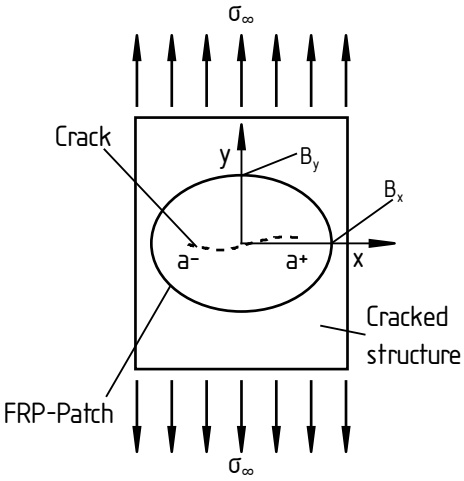

Figure 2.14: Position of the coordinate system and definition of variables

in x and y direction are defined with the variables B_x and B_y respectively. The symbol σ_∞ denotes the applied stress and the stress intensity factor K_I^* is usually determined for double-sided repairs in a first step. The reduction factor θ can then be adapted for single-sided repairs, general bending, thermal stresses or other parameters that influence patch efficiency.
The additional parameter that have to be considered are incorporated into the schematic procedure of the fracture mechanical proof described in Fig. 2.4 and illustrated in Fig. 2.15. Here, the elements "cracked component" and "fracture mechanics specimen" from the general fracture mechanical proof, depicted on the right-hand side, are extended by the "bonded patch". The parent material remains the same, meaning that the fracture mechanical parameters like K_IC are still the same. In contrast, crack growth assessment now has to be performed for the patched component. Repair geometry and possible additional loads resulting from bending effects, thermal loads or similar add to the given crack and component geometry and the already applied loads. Next to the critical crack length, additional information such as patch stiffness requirements, or critical additional loads, can be extracted.

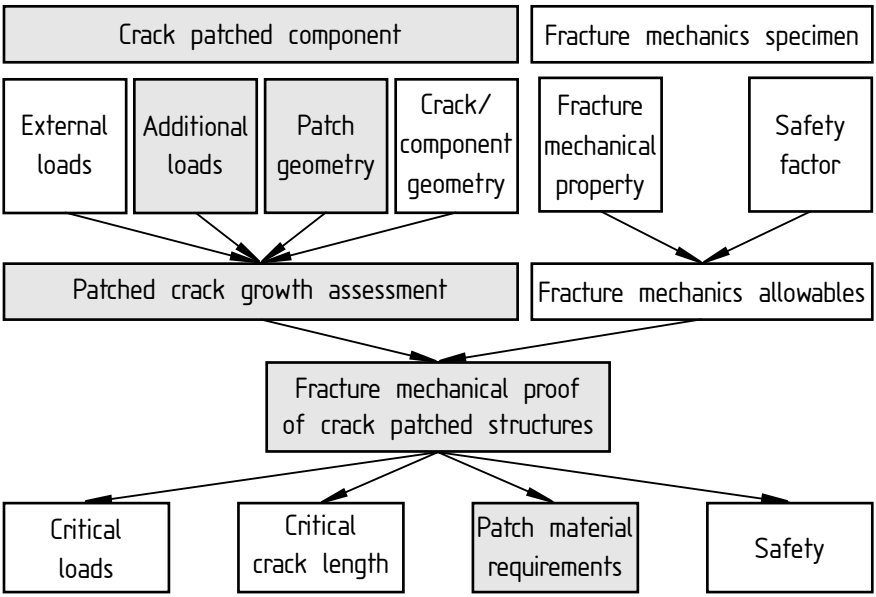

Figure 2.15: Schematic procedure of the fracture mechanic proof for a crack patched metallic structure

2.3.2 Performance Prediction of Bonded Patches

Up to now, there is no prediction method available that is able to describe the damage behaviour of crack patched structures in a realistic manner, including all possible degradation mechanisms and stress conditions. Current studies show, that disbond occurs in repair patches, even when the strength proof criteria are fulfilled. [41] Common methods for the fatigue performance prediction are based on the initial stress intensity factor K and neglect that it is actually not a constant value, as described in Sec. 2.1.3. For a metallic crack the stress intensity factor is a function of crack length $\sqrt{a}$ and thus increases with increasing crack length. The disregard of the increasing crack length a might be a sufficient approach for fatigue life estimations, as long as no other factors have an impact on the actual stress intensity. But, the efficiency of a patch repair is strongly dependent on many other loads as well. Here, the stress intensity factor K^* is not only a function of crack length $\sqrt{a}$, but is also linearly dependent on the reduction factor θ. During service, various loads can have an impact on θ. These loads are rather difficult to predict and thus it is not surprising that fatigue life predictions of bonded patches sometimes work out and sometimes do not.
Reliable methods for the estimation of the service fatigue life require the knowledge on the actual crack growth behaviour under service loads. Generally, it is possible though to make fatigue life estimations using the instantaneous stress intensity factor K_{I}^* together with the constants C and m of the parent material. But this approach neglects the influence of service loads and the actual stress state. The general fatigue design process as described above is based on 2D-models for both unpatched and patched components. Fatigue crack growth in a metallic sheet with in-plane loading results in an approximately 2-dimensional stress state, while the stress state in a crack patched component is 3-dimensional even when only in-plane loading is applied. For instance, inter-ply delamination in the patch or local patch delamination result from out-of-plane stress components. As these out-of-plane stress components are neglected in the K-concept for crack patched structures, a full three-dimensional finite element analysis is required to capture the overall stress state. [42] To be able to validate 3-dimensional finite element analyses it is indispensable to have a global picture of the internal or subsurface degradation processes under service loads.

2.4 Service Life Extension of Bonded Patches

With respect to the given boundary conditions, patch design aims at gaining the best possible reduction in stress intensity at the crack tip. Theoretically, it is even possible to completely inhibit further crack growth with a properly designed patch. Descriptively speaking, for a patch repair, the increase in stress intensity over increasing crack length is an upper bound, so that the stress intensity factor K^*_{ideal} of a patched component is always below the one of the same component without patch K_0. A second upper bound called K_∞ can be found for a properly designed patch, which is constant over crack length a. Thus, with increasing crack length a the stress intensity factor K^*_{ideal} asymptotically approaches a threshold value K_∞. The correlation between stress intensity K and crack length a is shown in Fig. 3.13. [2]

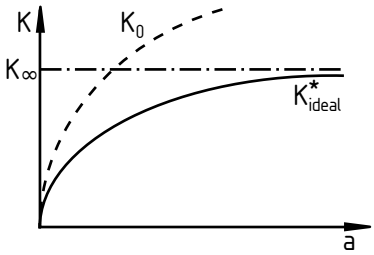

Figure 2.16: Upper bound of K^* for a crack patched structure [2]

The horizontal line shows the threshold value K_∞, the dashed line describes the course of K_I of a cracked component without patch and the continuous line the stress intensity factor of an ideally patched component K^*_{ideal}. Patch design now aims at the best possible reduction in stress intensity, namely K^*_{real} close to the ideal factor K^*_{ideal}. Classical fatigue life prediction methods make use of the initial stress intensity factor K. This seems to be appropriate for cracked metallic components as well that do not loose strength due to environmental conditions. But, obviously a prediction that does not include joint degradation during service does not result in reliable fatigue life estimations. [19, 17] As long as the long-term service behaviour cannot be predicted, the actual service life of a bonded patch is restricted from a safety point of view, which means that its full capacity cannot be exploited. Related to the bathtub curve there are two possibilities to increase the useful service

time of engineering components – the reduction of infant mortality and the delay of the wear-out phase. This study will have a closer look at these two opportunities.

2.4.1 The Preliminary Design Process – Opportunities to Reduce Infant Mortality

The infant mortality of a patched component is directly linked to the preliminary patch design. To minimize the infant mortality of bonded patches the patch needs to be designed in a way that minimizes the stress intensity at the crack tip effectively. Analytical patch design methods provided by Rose in 1988 [2] have proven to be very effective and are therefore common practice in the patch design process. Numerous numerical and practical investigations corroborate the validity of the stress intensity factor K_{I}^{*} of a patched component, determined by Rose's method. [43, 44] Since the 1980s, the concept has been revised and extended to a very high level of accuracy. [2, 13, 9, 45] Hence, when the recommended patch design guidelines are followed, the resulting stress intensity factor can be quantified and used for the preliminary fracture mechanical proof. However, in the case of a field repair for instance ideal conditions cannot always be met. The available space might be limited, elliptical patches might not be producible, laboratory conditions are not available and access to numerical simulation methods might be limited. The impact of conceivable differences between an ideally designed patch and a realistic patch needs to be determined on coupon test level, where long-term effects can be neglected. The quality of the predetermined stress intensity factor K_{I}^{*} and the resulting fatigue life prediction has to be evaluated.

2.4.2 Performance Prediction – Starting Points to Delay Wear-out Failure

The second opportunity to prolong the useful time is to delay the wear-out phase. One solution is to decrease the slope of the wear-out-curve, denoted with "wear-out failure of 'good' items" in Fig. 1.3. This means that the intercept point of the wear-out-curve with the curve describing "failure of weak items" is put off to a later date coming along with the delay of the transition between "useful time" and "wear-out". The task of the design engineer is to predict decisive service loads of any kind and to estimate their impact on the long-term service behaviour in order to estimate the fatigue life of a bonded

joint. [19] It is obvious that the prediction of variable service loads that can further affect one another is a highly ambitious goal which makes fatigue life predictions a challenging task. To be able to decrease the slope of the wear-out-curve, a realistic assessment of the long-term behaviour is essential. There are two opportunities to decrease the slope of the wear-out-curve. One is to improve patch performance in long-term service applications. The long-term performance of a patch is strongly dependent on the individual service loads. Improvements could be achieved on a chemical level by improving the bonding performance of the adhesive tape and/or the application process. This study focusses on the mechanical aspects, the bonding process will not be addressed here. There have already been comprehensive studies on the patch application process, taking it to a very high level, see [46]. The other, interesting opportunity is to reconsider the definition of patch "wear-out". Wear-out failure is defined from the safety point of view, trying to guarantee a right-side failure. This means that when a patch is somehow damaged, it is considered as wear-out. Thus, patches are considered as wear-out that can still fulfil their functionality at least for a determined life span. Having a look at the diagram shown in Fig. 2.17, the progress of the stress intensity factor of an unpatched component $K_{\mathrm{I},0}$ and the one of an ideally patched component $K^*_{\mathrm{I,ideal}}$ determine the boundaries for a real patch. Even when designing an ideal patch configuration, with continued use, the course of the real stress intensity factor $K^*_{\mathrm{I,real}}$ of patched components deviates from the ideal one. Depending on the impact of the service loads the actual course of $K^*_{\mathrm{I,real}}$ over a lies somewhere between the one of an ideally patched component and the one of a component without patch, see Fig. 2.17.

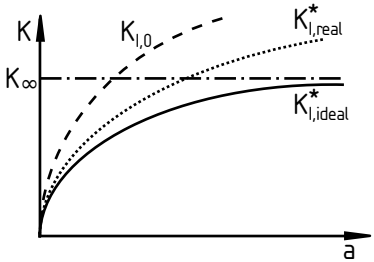

Figure 2.17: Course of the stress intensity factor K_{I} of a crack patched structure under service loads

In order to use the full capacity of a bonded patch it is therefore indispensable to be able

1. to predict the actual service loads reliably and
2. to describe the overall damage behaviour as a reaction to the service loads.

Different studies on the condition or so-called structural health monitoring (SHM) systems can be found in literature, see for instance [23]. These systems provide already good opportunities to monitor patch delamination during service. Results can be used to improve service load prediction. To be able to describe the overall damage behaviour as a reaction to the service loads, a monitoring system is needed that enables to continuously monitor all kind of (subsurface) damage processes at the same time.

3 Quality Assessment of Patch Design and Performance Prediction

In metallic crack patching, research still focuses on the preliminary patch design process and the determination of the stress intensity factor K_{I}^{*} of a patched component. In order to find out whether or not further improvements in the patch design process can have a measurable effect on the patch performance and thereby on a reduction of the infant mortality of the repaired component, a test series is defined. The idea is to test crack-patched specimens in a coupon test series. No environmental influences degrade the joint properties so that only the mechanical loading affects the joint quality. Patch design differs from the ideal conditions used in the presupposed theoretical approach. The comparison of the (semi-)analytical fatigue life predictions with the tested fatigue life gives an indication on the robustness of the preliminary patch design process.

3.1 Test Requirements

The performance of a patch repair depends on many factors. The initial crack tip stress reduction results for instance from the choice of materials, the joining process, or patch geometry, and dimensions. The idea of the test series is to find out how robust preliminary fatigue life estimations for patched components are when using Paris' law combined with Rose's method to determine the initial stress intensity factor K_{I}^{*}. To start with, service effects as environmental or temperature changes are left out and tests are performed under laboratory conditions. This way, it can be found out whether or not further improvements in the determination of K_{I}^{*} are productive with respect to a reduced infant mortality. The test series is designed to determine the

robustness of the theoretical stress intensity factor K_I^* against divergences between theory and practice concerning the initial crack tip stress reduction. As fatigue cracks often arise from drilled holes, the exemplarily chosen application is a rivet hole in an aluminium component with protruding rivet heads. Their respective dimensions can be found in Fig. 3.1.

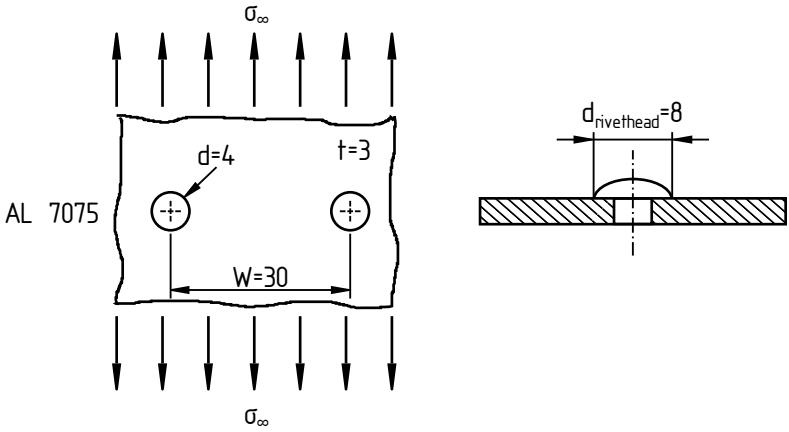

Figure 3.1: Exemplary application

Requirements result from the application boundary conditions and can be summarized as follows:

- patch preparation and application should be as simple as possible,
- patch application to rivet holes with several rivet lines should be possible,
- when necessary, it should be possible to repair two adjoining holes.

To be able to apply patches to two neighbouring holes results in circular patches, with the protruding rivet head causing a central hole. Thus, ring-shaped patches are used. Basically, there are two possibilities for a repair. The first is, that two neighbouring holes need to be stiffened or repaired, and the second one is that only one hole is affected and for the other holes around there is no need for repair action. The outer diameter is thus either restricted by the neighbouring hole or a neighbouring patch. The patches are supposed to be made of carbon fibre reinforced plastics (CFRP). In the

coupon test series the fatigue life of different patch configurations (variable thickness and variable outer diameter) is determined. In comparison, fatigue lives are estimated using Paris' law together with the theoretical ideal stress intensity factor K_{I}^{*}. Here, the patch effect is captured indirectly by the resulting fatigue life.

3.1.1 Specimen Geometry

The specimens were designed to be in accordance with the specifications for a centre-cracked-tension (CCT) specimen as defined in ASTM E647 [47], which is a common standard for fatigue tests. The rectangular specimen including the central rivet hole is sketched in Fig. 3.2. The material, its thickness, as well as the hole diameter and the corresponding rivet pitch result from the given application. The sheet material is made of aircraft aluminium 7075 with a thickness of $t = 3$ mm. Specimen width w is restricted by the clamping dimensions and results to be $w = 70$ mm, which adds up to a specimen length $= 200$ mm according to the ASTM standard [47]. Perpendicular to the load direction, hand-sawn crack starters with a length of about $l_{crack} = 2$ mm each can be found at either side of the hole. The initial crack length results to be $2a_0 = 8$ mm. The minimum rivet hole pitch of $W = 24$ mm results from the

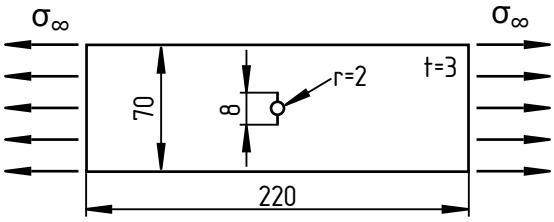

Figure 3.2: Specimen geometry

rivet hole diameter (d=4 mm). Semi-tubular pan head rivets of $d = 4$ mm have a rivet head diameter of $d_{\mathrm{rivethead}} = 8$ mm as defined in [48]. Thus, the inner diameter of the ring patch is set to be $d_{\mathrm{inner}}^{\mathrm{R}} = 8$ mm. A sketch of the specimen geometry including the patch can be found in Fig. 3.3. The outer diameter $d_{\mathrm{outer}}^{\mathrm{R}}$ is variable. Patch dimensions result from a preliminary design process, as described in the following section 3.2 after the presentation of the mechanical loads.

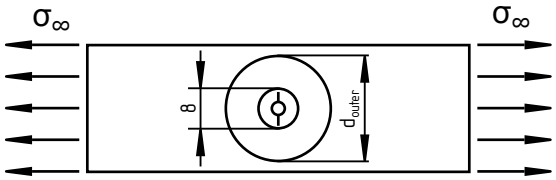

Figure 3.3: Specimen geometry with ring patch

3.1.2 Mechanical Loading

Fatigue at rivet holes can be caused by eccentric bending, bearing stresses, edge pressure or fretting corrosion, but mainly develop from a high notch stress concentration. Also, the rivet pitch as well as the number of rivet lines is decisive for the resulting stress values and thereby of the joint fatigue strength. Under low cycle fatigue, no plastic stress relief can occur resulting in a reduced sheet fatigue efficiency. [40] The qualitative stress distribution at rivet lines is sketched in Fig. 3.4. As depicted, under mechanical loading,

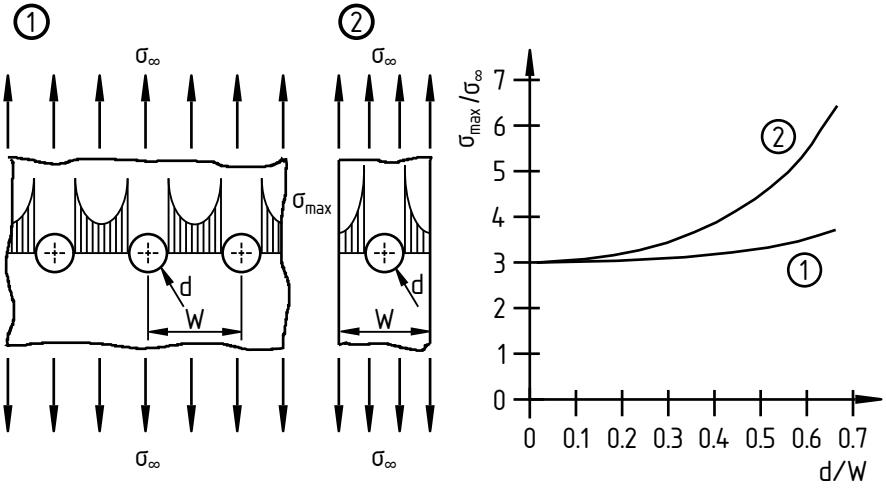

Figure 3.4: Elastic stress peaks at rivet holes for an infinte plate (1) and a finite strip (2) [40]

local stress peaks occur at the hole edges. The use of rivets further increases these stress peaks. For the given specimen geometry the ratio of hole diame-

Table 3.1: Loads applied

Fatigue Loads	
stress ratio R	0.1
Mean stress σ_{m}	64.9 MPa
Stress amplitude σ_{a}	53.1 MPa
Frequency f	10 Hz

ter d over rivet pitch W is $d/W = 0.05$. The diagram on the right-hand side of Fig. 3.4 shows that up to a ratio of $d/W \approx 0.1$ there is no difference in elastic peak stresses between an infinite plate and a finite strip, which means that the effect of a finite strip can be neglected here. For an infinite plate and a single hole, the stress peak is three times higher than the nominal tensile stress, leading to a fatigue efficiency of 1/3 compared to the unnotched sheet. To counteract high stress peaks at notches, local doublers can stiffen the highly stressed areas. [40, 49] In the case of rivet holes with protruding rivet heads, local adhesively bonded ring-shaped stiffeners and – for cracked structures – repair patches are suitable. [50]
Mechanical loads of aircraft structural components vary constantly during one flight cycle. The combination and variation of static and dynamic loads lead to a complex stress state that is difficult to reproduce on coupon level. As an example, the load variation of a wing during one single flight is sketched in Fig. 3.5. [1] The different flight phases start, climb, cruise, descent and landing exhibit all completely different load cases. That accumulates to a certain damage state over time. The precise implementation of such a load distribution for a coupon test is time-consuming, inefficient and thus expensive. It is therefore common practice to translate the overall load into one equivalent load cycle $\sigma_{\mathrm{eqivalent}}$ that induces a comparable damage to the structure as one single flight does. This is usually done by the rainflow count or a similar method, see for instance [1]. Resulting stresses used for the test series presented are listed in Table 3.1.

3.2 Preliminary Patch Design

Test requirements result in ring-shaped patches with a variable outer diameter. Also, patch thickness can freely be chosen. Limitations result from the

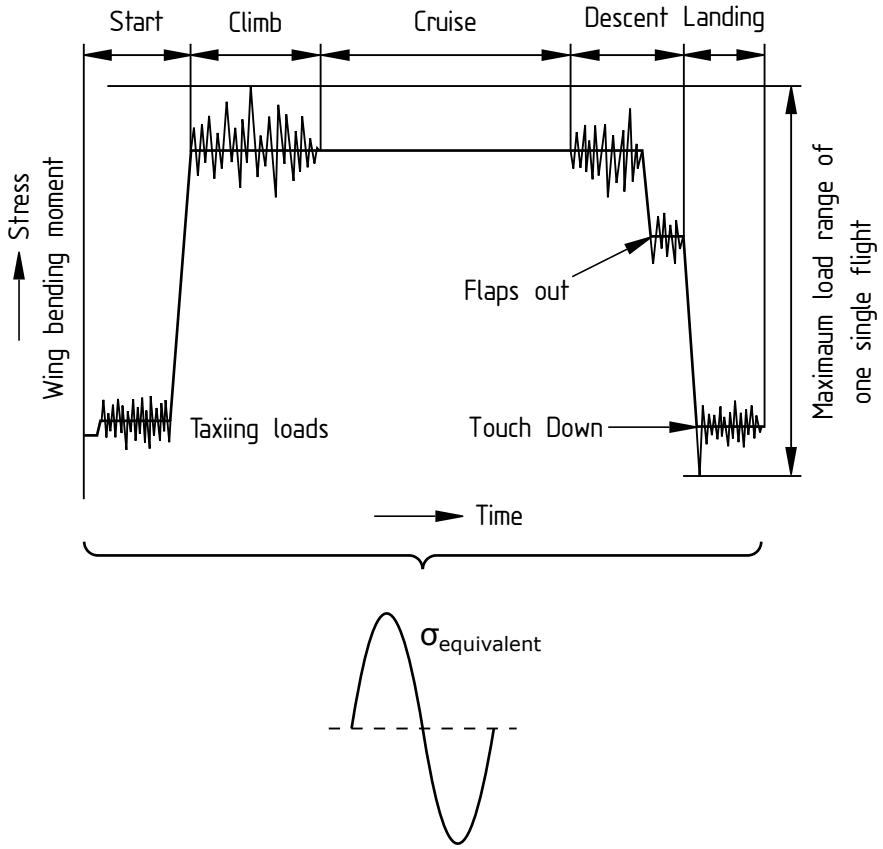

Figure 3.5: Varying loads on a wing structure during one single flight [1]

stresses in the component, which are the peel and shear stresses in the adhesive σ^{A}_{max} and τ^{A}_{max}, the maximum stress in the parent structure around the patch σ^{P}_{max} and the maximum stress in the reinforcing patch σ^{R}_{max}. Therefore, patch diameter and thickness is chosen with respect to the allowable stresses. For each variable, three different values are tested to capture the tendencies of the corresponding influence on the crack growth rates.
Minimum and maximum outer patch diameter d^{R}_{outer} are defined by the two stiffening procedures – stiffening two neighbouring holes and repairing a crack, respectively. The rivet pitch leads to a minimum outer patch diameter of $d^{R}_{outer} = 24$ mm for the stiffening of two neighbouring holes. The maximum outer patch diameter is $d^{R}_{outer} = 48$ mm, limited by the neighbouring hole. For patch manufacturing reasons, the smallest patch diameter is chosen to be $d^{R}_{outer} = 22$ mm and the biggest to be $d^{R}_{outer} = 50$ mm based on the rivet pitch. As a third medium value, a diameter of $d^{R}_{outer} = 36$ mm is additionally tested.
The range for the patch diameter is limited by the geometry of the application and the requirements given. The patch thickness on the other hand is not limited by the application geometry and can be chosen according to the mechanical properties. The patch thickness should be high enough to reduce fatigue crack growth effectively. On the other hand it has to be ensured that allowable stresses are not exceeded. Therefore, The effect of the patch thickness on the maximum stresses in the adhesive τ^{A} and σ^{A}, on the stress in the parent structure around the patch σ^{P}, on the stresses in the reinforcing patch σ^{R} and on the stresses at the crack tip have to be evaluated.
In the following assessment, the different patch diameters chosen are additionally taken into account to make sure that strength criteria can be met. For the presented estimations it needs to be considered that

- the given models do not entirely cover the damage behaviour of the patch,
- strength allowables are given for specific adherends with a defined preconditioning and in a defined environment and that
- only static strength allowables are available.

Thus, the given estimations are only a very rough estimation of the resulting stress state. The real behaviour can differ considerably and the static strength does not give information on the damage process under loading conditions.
Relevant material data used to determine the maximum stresses are listed in

Table 3.2. For the protection of data privacy, only reference values can be used for the patch material data. Paris constants of the plate material have been taken from [31].

Table 3.2: Material data ring patch tests

PLATE MATERIAL		Aluminium 7075
Thickness	t^{P}	3 mm
Young's modulus	E^{P}	71877 MPa
Poisson's ratio	ν^{P}	0.33
Tensile strength	R_{m}^{P}	438.95 MPa
Fracture toughness	K_{IC}^{P}	2.5 MPa $\sqrt{\mathrm{m}}$
Paris constant	C^{P}	1.88 E-6
Paris constant	m^{P}	2.05
PATCH MATERIAL		UD CFRP prepreg
Ply thickness	t^{R}	0.129 mm
Young's modulus in fibre direction	E^{R}	175000 MPa
Tensile strength	R_{m}^{R}	2000 MPa
ADHESIVE		Film adhesive FM® 94M
Thickness	t^{A}	0.13 mm
Shear modulus	G^{A}	823 MPa
Shear strength at 24°C	$\tau_{\mathrm{allowable}}^{\mathrm{A}}$	43.7 MPa
Peel strength at 24°C	$\sigma_{\mathrm{allowable}}^{\mathrm{A}}$	46.1 MPa

3.2.1 Maximum Stresses in the Adhesive

The decisive design parameters for adhesive joints are the shear stress τ^{A} and the peel stress σ^{A}. To fulfil the design requirements, the maximum stresses $\tau_{\mathrm{max}}^{\mathrm{A}}$ and $\sigma_{\mathrm{max}}^{\mathrm{A}}$ need to be smaller than the shear strength $\tau_{\mathrm{allowable}}^{\mathrm{A}}$ and the tensile strength $\sigma_{\mathrm{allowable}}^{\mathrm{A}}$ of the adhesive.

3.2.1.1 Patch Diameter $d_{\mathrm{outer}}^{\mathrm{R}}$

As explained in Section 2.2, the representative model to determine adhesive shear stresses is the DOFS, while the model used to determine the critical peel

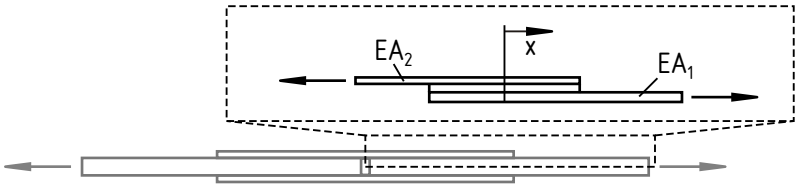

Figure 3.6: Quarter model of the DOFS specimen

stresses is the SDS. Hence, for the determination of the maximum stresses the corresponding models are used.

Shear Stresses τ^{A}

To describe the shear stress distribution in a DOFS in load direction (x-direction), a quarter model is chosen as the specimen is double symmetric, see Fig. 3.6. The quarter model leads to comparable results as the SDS and further considers the influence of the stiffness ratio S. Stresses determined using the DOFS are below the ones using the SDS. Patch sizing against the quarter model is therefore conservative. The shear stress distribution of an overlap joint follows a bathtub-curve with its maximum values at the free ends of the overlapping adherends. [51] For adherends of different stiffness, the distribution is not symmetric in load direction (x-axis) and the position of the global maximum value depends on the stiffness ratio S, see also Fig. 3.7. All relevant formulas can be found in [40]. The tensile stiffness EA is the product of the material's strength, or Young's modulus E and the corresponding area A at which the load is applied. The stiffness ratio S is defined to be

$$S = \frac{(EA)_2}{(EA)_1} = \frac{(EA)^{\mathrm{R}}}{(EA)^{\mathrm{P}}}.$$

The maximum value can be found at the free end of the adherend with the higher tensile stiffness $(EA)_{\max}$. According to [40], the maximum shear stress in the adhesive at the free edges can be derived to be

$$\tau^{\mathrm{A}}_{\max} = \sigma_\infty \frac{t^{\mathrm{P}}}{B_y} \frac{\beta_{\mathrm{QM}}}{2} \left[\coth\left(\frac{\beta_{\mathrm{QM}}}{2}\right) + \frac{(1-1/S)}{(1+1/S)} \tanh\left(\frac{\beta_{\mathrm{QM}}}{2}\right) \right]. \quad (3.1)$$

The factor t^{P} is the thickness of the plate, $B_{y,\max}$ the patch boundary in y-direction (see 2.14), and β_{QM} describes the influence of the adhesive stiffness

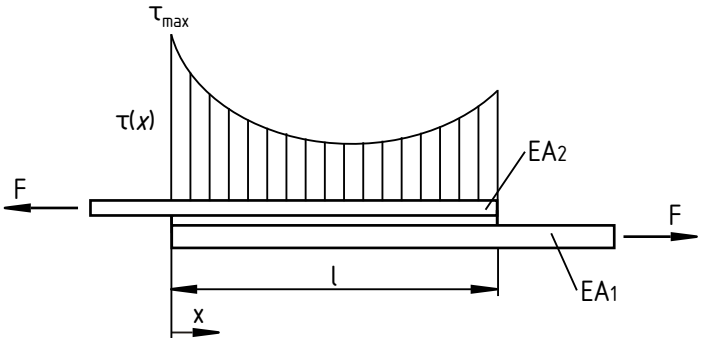

Figure 3.7: Shear stress distribution in a joint with adherends of different tensile stiffness EA

on the joint

$$\beta_{\mathrm{QM}} = \sqrt{\left(1 + \frac{1}{S}\right) \frac{G^{\mathrm{A}} B_y^2}{E^{\mathrm{P}} t^{\mathrm{P}} t^{\mathrm{A}}}}. \text{ [40]}$$

Here, G^{A} is the shear modulus of the adhesive, E^{P} Young's modulus of the plate and t^{A} the thickness of the adhesive.
For the given test series the shear stress distribution is determined for all combinations of patch diameter and thickness variations. Exemplarily, Fig. 3.8 depicts the shear stress distribution of all three diameter along the overlap length for a number of CFRP plies equal to $n_{\mathrm{ply}} = 15$. The effect of the patch diameters on the shear stress reduction can clearly be seen. In the case of a small patch with a diameter of $d^{\mathrm{R}}_{\mathrm{outer}} = 22$ mm the shear stresses are highest with a maximum shear stress of $\tau^{\mathrm{A}}_{\mathrm{max}}(d^{\mathrm{P}}_{\mathrm{outer}} = 22\,\mathrm{mm}) = 44.12$ MPa, which is slightly above the allowable shear stress of the adhesive $\tau^{\mathrm{A}}_{\mathrm{allowable}} = 43.7$ MPa. But, with increasing diameter, the load transfer is shifted to the edges and the maximum shear stress is considerably reduced to $\tau^{\mathrm{A}}_{\mathrm{max}}(d^{\mathrm{P}}_{\mathrm{outer}} = 36\,\mathrm{mm}) = 26.96$ MPa and $\tau^{\mathrm{A}}_{\mathrm{max}}(d^{\mathrm{P}}_{\mathrm{outer}} = 50\,\mathrm{mm}) = 19.41$ MPa.

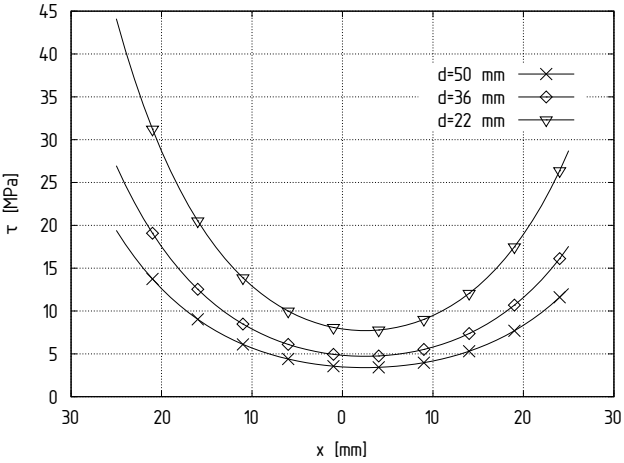

Figure 3.8: Influence of the patch diameter on the shear stress distribution

Peel Stresses σ^{A}

Peel stresses are critical in the safe life zone at the patch boundary, represented by the SDS, see [35]. The maximum peel stress is given to be

$$\sigma^{\mathrm{A}}_{\max} = \tau^{\mathrm{A}}_{\max,\mathrm{SDS}} \left[\frac{3t^{\mathrm{R}}(E')^{\mathrm{A}}}{(E')^{\mathrm{R}} t^{\mathrm{A}}} \right]^{\frac{1}{4}}. \tag{3.2}$$

In this equation, t^{R} is the thickness of the reinforcing patch and $(E')^{\mathrm{A}}$, $(E')^{\mathrm{R}}$ are the specific Young's moduli

$$(E')^{i} = \frac{E^{i}}{1-\nu},$$

of the adhesive and reinforcement, respectively including the corresponding Poisson's ratio ν. The analytical models used in the following sections are based on the assumption that $\nu^{\mathrm{R}} = \nu^{\mathrm{P}}$ and thus the term ν refers to the plate and the reinforcement in equal measure.
As the SDS formulation of the peel stress is independent of the x-coordinate, the patch diameter has no influence on the maximum peel stress. The corre-

sponding shear stress $\tau^{\mathrm{A}}_{\mathrm{max,SDS}}$ can be determined using

$$\tau^{\mathrm{A}}_{\mathrm{max,SDS}} = \frac{\beta_{\mathrm{SDS}} F}{w} \frac{(E')^{\mathrm{R}} t^{\mathrm{R}}}{(E')^{\mathrm{R}} t^{\mathrm{R}} + 2(E')^{\mathrm{P}} t^{\mathrm{P}}} \tag{3.3}$$

Here, w denotes the specimen width and F the applied force $F = \sigma_\infty t^{\mathrm{P}} w$. The characteristic adhesive factor β_{SDS} for the skin doubler specimen results from the relation

$$\beta_{\mathrm{SDS}} = \sqrt{\frac{G^{\mathrm{A}}}{t^{\mathrm{A}}} \left(\frac{2}{(E')^{\mathrm{P}} t^{\mathrm{P}}} + \frac{1}{(E')^{\mathrm{R}} t^{\mathrm{R}}} \right)}.$$

3.2.1.2 Patch Thickness t^{R}

As expected, the influence of the patch thickness on the stress state in the adhesive is higher than the influence of the diameter, as the stiffness ratio S is the significant sizing variable. For the determination of the stress values, the shear stress distribution according to [40] and the peel stresses in the SDS are evaluated again.

Shear Stresses τ^{A}

With increasing patch thickness, also the maximum shear stress increases. [40] The maximum number of plies results from the shear stress closest to the limit value of $\tau^{\mathrm{A}}_{\mathrm{allowable}} = 43.7$ MPa. A patch with $n_{\mathrm{ply}} = 15$ layer CFRP induces a maximum shear stress of $\tau^{\mathrm{A}}_{\mathrm{max}}(n_{\mathrm{ply}} = 15) = 44.12$ MPa, which is slightly above the material limit. Thus, the maximum thickness is chosen to be $t^{\mathrm{A}}_{\mathrm{max}} = 15\, t_{\mathrm{CFRP}} = 1.935$ mm.
For the minimum value, the recommendation to achieve a stiffness ratio of $S = 1$ [40] is used. The closest value of $S = 0.95$ applies for a number of $n_{\mathrm{ply}} = 9$ layer CFRP, which is therefore chosen to be the minimum number of plies. Again, the medium value of $n_{\mathrm{ply}} = 12$ is tested supplementary.
The increase of $\tau^{\mathrm{A}}_{\mathrm{max}}$ with increasing patch thickness is derived using Eq. 3.1 and plotted in Fig. 3.9. In this plot it can be seen that the global maximum shear stress changes its position with increasing patch thickness. The maximum shear stress is always located at the free end of the adherend with the higher stiffness. [40] Between $n_{\mathrm{ply}} = 9$ and $n_{\mathrm{ply}} = 12$ layer CFRP the stiffness ratio changes from a value slightly below the balanced bonding of $S = 1$ to a value $S > 1$. Therefore, also the position with the highest probability for initial patch disbond shifts.

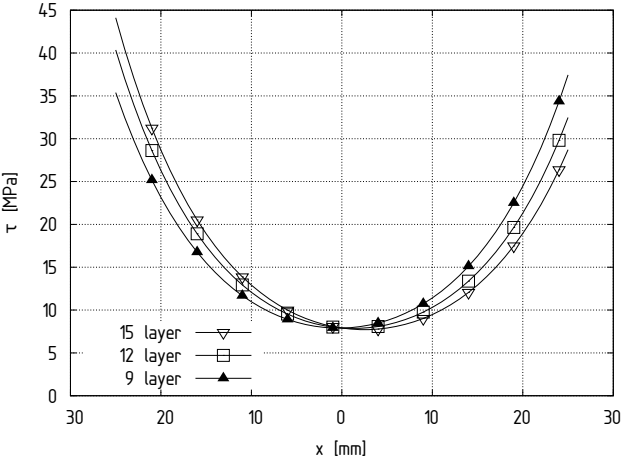

Figure 3.9: Influence of the patch thickness on the shear stress distribution

Peel Stresses σ^{A}

Patch thickness also affects the peel stresses. With increasing patch thickness also the peel stresses increase. Taking the maximum thickness of the selected values to be $t^{\mathrm{R}}_{\max} = 1.935$ mm, the maximum peel stress results to be $\sigma^{\mathrm{A}}_{\max} = 42.96$ MPa (see Eq. 3.2) which is still below the allowable peel stress $\sigma^{\mathrm{A}}_{\mathrm{allowable}} = 46.1$ MPa and therefore, the patch configurations to be tested meet all adhesive strength requirements.

3.2.2 Maximum Stress in the Parent Structure around the Patch $\sigma^{\mathrm{P}}_{\max}$

The efficient stress in the plate around the patch boundaries results from the stresses in the patch at the marginal patch position in y-direction, here, the outer patch diameter $d^{\mathrm{R}}_{\mathrm{outer}}$

$$\sigma^{\mathrm{P}}_{\max} = \sigma(x = 0, y = d^{\mathrm{R}}_{\mathrm{outer}}) = (1 + S)\sigma_{\infty}\Phi. \tag{3.4}$$

The factor Φ is given by

$$\Phi = \frac{1}{Z}\left[4 + 2\frac{B_y}{B_x} + 2\frac{B_x}{B_y} + S\left(3 + \nu + 2\frac{B_y}{B_x}\right) + S\lambda\left(1 - \nu - 2\nu\frac{B_y}{B_x}\right)\right],$$

with

$$Z = 3(1+S)^2 + 2(1+S)\left(\frac{B_y}{B_x} + \frac{B_x}{B_y} + \nu S\right) + 1 - \nu^2 S^2.$$

and the biaxiality λ of the applied stress, which is $\lambda = 0$, as no stress is applied in x-direction. All relevant formulas can also be found in [35]. As can be seen in Eq.3.4, only the patch thickness has an influence on the maximum stress in the parent structure around the patch. With increasing patch thickness, also the maximum stress increases. Therefore, the thickest patch of 15 layer CFRP is relevant for the proof. The maximum stress in the parent structure around the patch for a 15 layer patch results to be $\sigma^{\mathrm{P}}_{\mathrm{max}}(n_{\mathrm{ply}} = 15) = 148.22$ MPa. Compared with a static strength of $R^{\mathrm{P}}_{\mathrm{m}} = 438.5$ MPa the safety against static failure is $j^{\mathrm{P}}_{\mathrm{static}}(n_{\mathrm{ply}} = 15) = 2.96$. The fatigue strength of aluminium materials can be approximated to be $\sigma^{\mathrm{P}}_{\mathrm{allowable,fatigue}} \approx 0.6\, R^{\mathrm{P}}_{\mathrm{m}}$ [52], resulting in a safety factor of $j^{\mathrm{P}}_{\mathrm{fatigue}}(n_{\mathrm{ply}} = 15) = 1.78$. The maximum stress in the parent structure around the patch is therefore not expected to be critical.

3.2.3 Maximum Stress in the Reinforcement $\sigma^{\mathrm{R}}_{\mathrm{max}}$

Normal stresses in the patch result from the load redistribution through the patch in load direction. Hence, the maximum stress in the reinforcement is given by

$$\sigma^{\mathrm{R}}_{\mathrm{max}} = \frac{F\big|_{y=0}}{t_{\mathrm{R}}}. \tag{3.5}$$

With $F\big|_{y=0}$ the load F along the x-axis that results from the applied stress and is partly transferred through the plate and partly transferred through the patch in the reinforced region. A formulation for $F\big|_{y=0}$ is given by

$$F\big|_{y=0} = \sigma_\infty t_{\mathrm{P}} \left[1 + \frac{S}{Z}\left(1 + 2(1+S)\frac{B_y}{B_x}(1-\nu\lambda) + (1+S-\nu S)(\lambda-\nu)\right)\right].$$

For more detailed information on the presented equations see [2].
The analytical model describing the maximum stress in the reinforcing patch is independent of the patch diameter, only the patch thickness is relevant, see Eq. 3.5. Understandably, the maximum stress in the reinforcing patch decreases with increasing patch thickness. Thus, in this case the thinnest patch of 9 layer CFRP is relevant for the proof. The maximum stress in the

reinforcement results to be $\sigma^{\mathrm{R}}_{\max}(n_{\mathrm{ply}} = 9) = 363.82$ MPa. As the allowable stresses for the used material are unknown, an appraisal using literature values is performed. For HT-CFRP, the maximum tensile strength lies around $R^{\mathrm{R}}_{\mathrm{m}} = 2000$ MPa [53] and its fatigue strength for $R = 0.1$ at around $\sigma^{\mathrm{R}}_{\mathrm{fatigue}} \approx 0.6\, R^{\mathrm{R}}_{\mathrm{m}}$ [54]. The resulting safety factors are $j^{\mathrm{R}}_{\mathrm{static}}(n_{\mathrm{ply}} = 9) = 5.5$ and $j^{\mathrm{R}}_{\mathrm{fatigue}}(n_{\mathrm{ply}} = 9) = 3.5$. In conclusion, for the given configuration, patch failure is not expectable. The strength proof is thus completed.

3.2.4 Stresses at the Crack Tip

The main task of the repair (and stiffener) patch is to reduce the stress peak at the rivet hole and the crack tip, respectively. To neutralize the stress peak at the hole, an elliptical patch shape is the ideal solution. [40] For crack repairs elliptical patches are recommended as well. [2] But, also circular patches reduce the stress peaks and lead to enhanced fatigue life.

3.2.4.1 Patch Diameter $d^{\mathrm{R}}_{\mathrm{outer}}$

The patch diameter has no significant influence on stress reduction in the sheet metal. But, a bigger diameter promotes a shear stress relaxation in the adhesive layer and thus also has a positive effect on the repair efficiency. [13, 40] Important for the stress peak reduction is the aspect ratio B_x/B_y [2, 40], since only continuous elliptical patches can entirely neutralize the stress peak at the hole edges. It applies that aspect ratios $B_x/B_y > 1$ have a positive effect on the stress peak reduction in the plate. Therefore it is expected, that an increasing patch diameter has a positive effect on the fatigue life.

3.2.4.2 Patch Thickness t^{R}

The patch thickness has a relevant influence on the stresses at the crack tip. In first approximation applies that the thicker the patch, the smaller the stress peak. But, it also applies that the thicker the patch, the higher the peel stresses in the adhesive and the higher the bending effect. [55] To decrease the stress peak efficiently, a stiffness ratio of $S = 1 - 2$ is recommended. [40] For the test configuration this means that the stiffness ratio varies between $S(n_{\mathrm{ply}} = 9) = 0.95$, $S(n_{\mathrm{ply}} = 12) = 1.26$ and $S(n_{\mathrm{ply}} = 15) = 1.57$ and thereby (nearly) in the recommended range.

3.2.4.3 Fatigue Crack Growth Reduction

For the stress peak reduction in the plate there are no analytical models available that help to capture the effect of the patch directly. A small example helps to classify the reduction of crack growth rates by circular ring-shaped patches.
Even though the stress peak cannot completely be neutralized using a circular ring-shaped patch, the stress peak can be reduced. Comparing an infinite plate with hole with an infinite plate without hole, both under uniaxial tension, the stress peak at the hole is three times higher than the nominal stress in the plate. The efficiency factor of a rivet row is defined to be the ratio of the transferable stress $\sigma_{\text{transferable}}$ to the material strength σ_{B}

$$\eta = \frac{\sigma_{\text{transferable}}}{\sigma_{\text{B}}} \tag{3.6}$$

and thus the fatigue efficiency of the plate without hole is three times higher than the one of the plate with hole. Put differently, the fatigue efficiency is reduced to $\eta_{\text{hole}} = 1/3\,\eta_{\text{plate}}$ by the hole. [40]
Wiedemann provides one example saying that a ring patch, as shown in Fig. 3.10, is able to increase the fatigue efficiency to $\eta_{\text{repair}} = 0.78$. [40] This

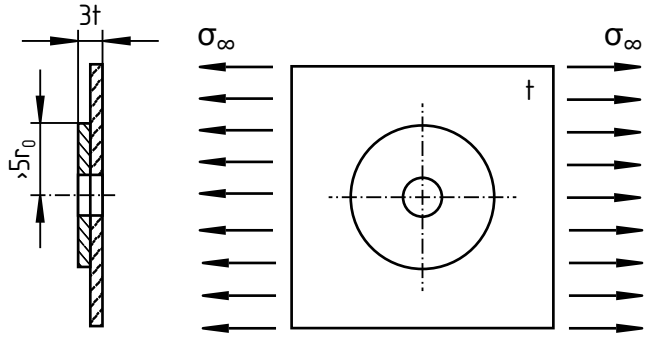

Figure 3.10: Ring patch configuration with the efficiency of $\eta_{\text{repair}} = 0.78$ [40]

means, that the local stress peak is reduced from $\sigma^{\text{P}}_{\text{max}} = 3\,\sigma_{\text{transferable}}$ to $\sigma^{\text{P}}_{\text{max}} \approx 1.282\,\sigma_{\text{transferable}}$. Now, what does this stress peak reduction mean for the component's fatigue life? The effect can be assessed using Paris' law. In the example provided, material constants from Al 7075 are used. Inserting

the ΔK_{I}-function (Eq. 2.2)

$$\frac{\mathrm{d}a}{\mathrm{d}N} = C^{\mathrm{P}} \left(Y_{\mathrm{I}}\sqrt{\pi a}\right)^{m^{\mathrm{P}}} (\Delta\sigma)^{m^{\mathrm{P}}} \tag{3.7}$$

illustrates the strong influence of $\Delta\sigma$, which is the variation of the applied stress σ_∞.
Replacing

$$\Delta\sigma = (1-R)\sigma_\infty = (1-R)\eta\sigma_{\mathrm{transferable}}. \tag{3.8}$$

in Eq. 3.7, results in

$$\frac{\mathrm{d}a}{\mathrm{d}N} = C^{\mathrm{P}} (\Delta Y_{\mathrm{I}}\sqrt{\pi a})^{m^{\mathrm{P}}} ((1-R)\eta\sigma_{\mathrm{transferable}})^{m^{\mathrm{P}}}. \tag{3.9}$$

Comparing the plate with a drilled hole without patch and the one with a ring patch results in the ratio of

$$\frac{\frac{\mathrm{d}a}{\mathrm{d}N}(\sigma^{\mathrm{P}} = 3\sigma_{\mathrm{transferable}})}{\frac{\mathrm{d}a}{\mathrm{d}N}(\sigma^{\mathrm{P}} \approx 1.282\sigma_{\mathrm{transferable}})} \approx 5.713, \tag{3.10}$$

using the material constant $m^{\mathrm{P}} = 2.05$ for Al 7075 [31]. This means that a peak stress of $\sigma^{\mathrm{P}}_{\mathrm{max}} = 3\,\sigma_{\mathrm{transferable}}$ results in a crack growth rate $\mathrm{d}a/\mathrm{d}N$, a crack growth rate $\mathrm{d}a/\mathrm{d}N$ 5 times higher than the one for a reduced peak stress of $\sigma^{\mathrm{P}}_{\mathrm{max}} \approx 1.282\,\sigma_{\mathrm{transferable}}$.
Of course, the comparison does not entirely cover the given application in patch configuration and dimensions. But, it reveals that when stress peaks cannot entirely be neutralized by the patch, the stress peak reduction still has a significant effect on the fatigue crack growth.

3.2.5 Resulting Test Procedure

The preliminary analyses result in nine different patch configurations. Additionally, specimens without patches are tested as a reference. For statistical reasons, each configuration is tested three times. Table 3.3 summarizes the different test configurations, specimens numbered from D02 to D36. Based on the results from more or less comparable applications, it is expected that all patch configurations have a positive effect on the fatigue life compared to the unpatched specimens. The influence of the patch thickness is expected to be higher than the influence of the diameter.

Table 3.3: Specimen design – patch variation

$\varnothing_{\text{patch}}$ \ n_{ply}	No Patch	9	12	15
no patch	D02–D09			
22 mm		D10–D12	D19–D21	D28–D30
36 mm		D13–D15	D22–D24	D31–D33
50 mm		D16–D18	D25–D27	D34–D36

3.3 Theoretical Fatigue Life

The definition of the test parameter allows for the determination of the remaining fatigue life of the different patch configurations. For the fatigue life assessment, the corresponding stress intensity factors of the patched specimens $K^*_{\text{I,i}}$ are estimated using Rose's model.

3.3.1 Determination of the Stress Intensity Factors K_{I} of the Specimens without Patch

The stress intensity factor of an unpatched specimen can be determined by

$$K_{\text{I}} = Y_{\text{I}} \sigma_\infty \sqrt{\pi a}.$$

The cyclic stress intensity factor is determined using

$$\Delta K_{\text{I}} = K_{\text{I,0,max}}(1 - R).$$

For a component with a central hole and edge cracks, the geometry factor Y_{I} can be described by a function of total crack length $2a$, as provided [31] and shown in Fig. 3.11. Rose's model comes from the assumption of a Griffith crack without the central hole. A comparison of the geometry factor Y_{I} for a finite strip with a central hole with edge cracks and a finite strip with a Griffith crack is provided by [1], see Fig. 3.12. It can be seen that from a ratio $2a/W = 0.25$ on there is no significant difference between the two geometry factors Y_{I}. For the given specimen width of $W = 70$ mm, the geometry factors coincide from a total crack length of $2a = 17.5$ mm.

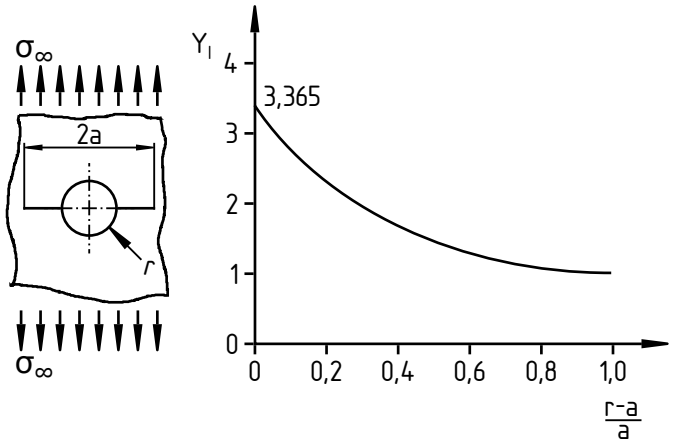

Figure 3.11: Geometry factor Y_I as a function of total crack length $2a$ as provided by [31]

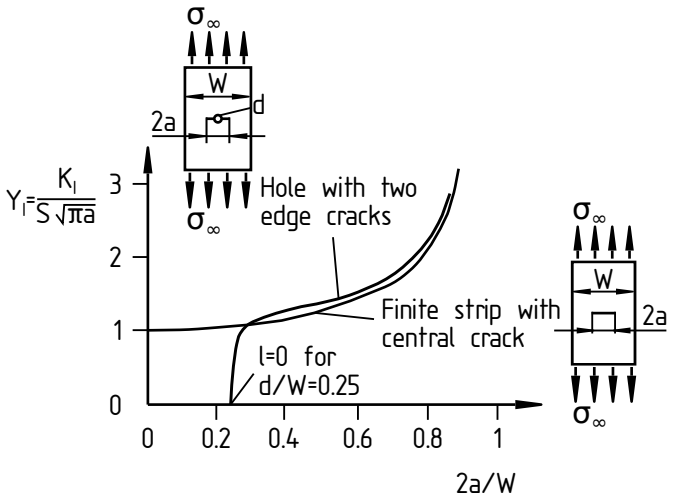

Figure 3.12: Geometry factor Y_I for a strip with a crack and a strip with a hole with two edge cracks as shown in [1]

3.3.2 Determination of the Stress Intensity Factors K_{I}^{*} of the Patched Specimens

The determination of the stress intensity factor of the crack patched specimens is based on the equations given in [13]. Compared to the unpatched component, Rose's model assumes a Griffith crack, so that the effect of the central hole is left out and the geometry factor $Y_{\mathrm{I}} = 1$. The reduced stress intensity factor K for the repaired component is given by

$$K_{\mathrm{I}} = \theta \sigma_{\infty} \sqrt{\pi a}.$$

One option to determine the stress intensity reduction factor θ is based on numerical analyses and given by the relation

$$\theta = \left[\frac{1 + 2.23ka}{1 + 4.776ka + 7(ka)^2} \right]^{1/2}. \tag{3.11}$$

The numerical solution given in Eq. 3.11 results in a slight overestimation of the reduction in stress intensity K_{I}, but only in the short crack region. The factor k can be determined by

$$k = \frac{G^{\mathrm{A}}}{\beta t^{\mathrm{A}} t^{\mathrm{P}} E^{\mathrm{P}}} \tag{3.12}$$

with

$$\beta = \sqrt{\frac{G^{\mathrm{A}}}{t^{\mathrm{A}}} \left[\frac{1 - \nu_{\mathrm{P}}^2}{E^{\mathrm{P}} t^{\mathrm{P}}} + \frac{1 - \nu_{\mathrm{R}}^2}{E^{\mathrm{R}} t^{\mathrm{R}}} \right]}. \tag{3.13}$$

For a symmetric repair, the stress intensity factor K_{I} can now be determined. For a single-sided repair, the maximum stress intensity factor K_{I}^{*} is composed of the membrane stress part K_{mean} and the bending part K_{b}

$$K_{\mathrm{I}}^{*} = K_{\mathrm{mean}} + K_{\mathrm{b}}.$$

The factor K_{mean} corresponds to the stress intensity factor K_{I} of a symmetric repair. The bending factor K_{b} has to be determined individually using the root mean square factor K_{rms}, which is given by

$$K_{\mathrm{rms}}^2 = K_{\mathrm{mean}}^2 + \frac{1}{3} K_{\mathrm{b}}^2. \tag{3.14}$$

Alternatively, K_{rms} can be determined using Eq. 3.11, where the spring constant k has to be adapted for single-sided repairs. The spring constant k^* for single-sided repairs is given by

$$k^* = \frac{k}{\bar{\omega}^2},$$

with

$$\bar{\omega}^2 \approx 2 + \frac{3t^{\mathrm{P}}}{2t^{\mathrm{R}}} + \frac{3\beta t^{\mathrm{P}}}{\bar{\kappa} t^{\mathrm{R}}} \left(1 + \frac{t^{\mathrm{P}}}{t^{\mathrm{R}}}\right) + +(1+S)\left(2 + \frac{3t^{\mathrm{P}}}{2t^{\mathrm{R}}}\right) \frac{\bar{z}^2 t^{\mathrm{P}}}{I_t} +$$
$$+(1+S)\frac{\beta}{\bar{\kappa}} \left(1 + \frac{t^{\mathrm{P}}}{t^{\mathrm{R}}}\right) \frac{\bar{z}(t^{\mathrm{P}})3}{t^{\mathrm{R}} I_t} \left(\frac{3\bar{z}}{t^{\mathrm{P}}} - 1\right) \bar{\kappa}^4 = \frac{(E')^{\mathrm{A}}}{4t^{\mathrm{A}}} \left[\frac{1}{D^{\mathrm{P}}} + \frac{1}{D^{\mathrm{R}}}\right]$$

and

$$\begin{aligned}
D^{\mathrm{P}} &= (E')^{\mathrm{P}}(t^{\mathrm{P}})3/12, \\
D^{\mathrm{R}} &= (E')^{\mathrm{R}}(t^{\mathrm{R}})3/12, \\
\bar{\kappa}^4 &= (E')^{\mathrm{A}}/(4t^{\mathrm{A}})(1/D^{\mathrm{P}} + 1/D^{\mathrm{R}}), \\
I_t &= I^{\mathrm{P}} + I^{\mathrm{R}}(E')^{\mathrm{R}}/(E')^{\mathrm{P}}, \\
I^{\mathrm{P}} &= (t^{\mathrm{P}})3 + t^{\mathrm{P}}\bar{z}^2, \\
I^{\mathrm{R}} &= (t^{\mathrm{R}})3/12 + t^{\mathrm{R}}(t^{\mathrm{P}} + t^{\mathrm{R}} - 2\bar{z})^2/4, \\
\bar{z} &= S(t^{\mathrm{P}} + t^{\mathrm{R}} + 2t^{\mathrm{A}}))(2 + (1+S)).
\end{aligned}$$

With the spring constant k^* for single-sided repairs, the corresponding root mean square factor can be approximated by

$$K_{\mathrm{rms}} = \frac{\sigma_\infty}{1+S}\sqrt{\pi a}\,\theta(k^* a).$$

Inserting the result for K_{rms} into Eq. 3.14, the factor K_{b} can be found. Together with the factor K_{mean} for a symmetric repair, the stress intensity factor K_{I}^* for a single-sided repair can then be determined. The stress intensity factor ΔK_{I}^* for cyclic loading results from

$$\Delta K_{\mathrm{I}}^* = K_{\mathrm{I,max}}^*(1-R).$$

3.3.3 Theoretical Upper Bound K_∞

Theoretically, crack growth can be completely inhibited, as long as the stress intensity factor – here K_I^* – lies below the upper limit K_∞. Equations used to determine K_∞ are given by [13]. In the elastic regime of the adhesive, this limit can be determined using

$$\Delta K_{\infty,\mathrm{el}} = \frac{\sigma_0}{\sqrt{k}}. \tag{3.15}$$

The maximum allowable shear stress of the adhesive $\tau_{\max}^{\mathrm{A}}$ can be used to determine the adhesive yield stress

$$\sigma_{\mathrm{Y}}^{\mathrm{A}} = \frac{\tau_{\max}^{\mathrm{A}}}{\beta t^{\mathrm{P}}}. \tag{3.16}$$

The upper bound $K_{\infty,\mathrm{pl}}$ including adhesive plasticity results from the relation

$$\Delta K_{\infty,\mathrm{pl}} = K_{\infty,\mathrm{el}} \left[\frac{P^3 + 3P - 1}{3P^2} \right]^{1/2}, \tag{3.17}$$

with

$$P = \frac{\sigma_0}{\sigma_{\mathrm{Y}}^{\mathrm{A}}}. \tag{3.18}$$

For each configuration, the evaluation incorporates a possible exceeding of the adhesive shear yield strength $\tau_{\max}^{\mathrm{A}}$.

3.3.4 Stress Intensity Factors and Fatigue Life Estimation

The progression of the stress intensity factor K_I^* with increasing crack length a is evaluated for the different patch configurations, as listed in Table 3.3. Remembering that only the aspect ratio of the patch, which is $B_x/B_y = 1$ for the circular patch, and not the diameter influences the theoretical results, only the effect of the patch thickness is analysed. Results are shown in Fig. 3.13. Plot 3.13 a) shows the result for $n_{\mathrm{ply}} = 9$ layers, plot 3.13 b) the result for $n_{\mathrm{ply}} = 12$ layers and plot 3.13 c) the result for $n_{\mathrm{ply}} = 15$ layers. Each plot contains the upper bound K_∞ as well as the courses of $K_{0,\mathrm{Griffith}}$ and

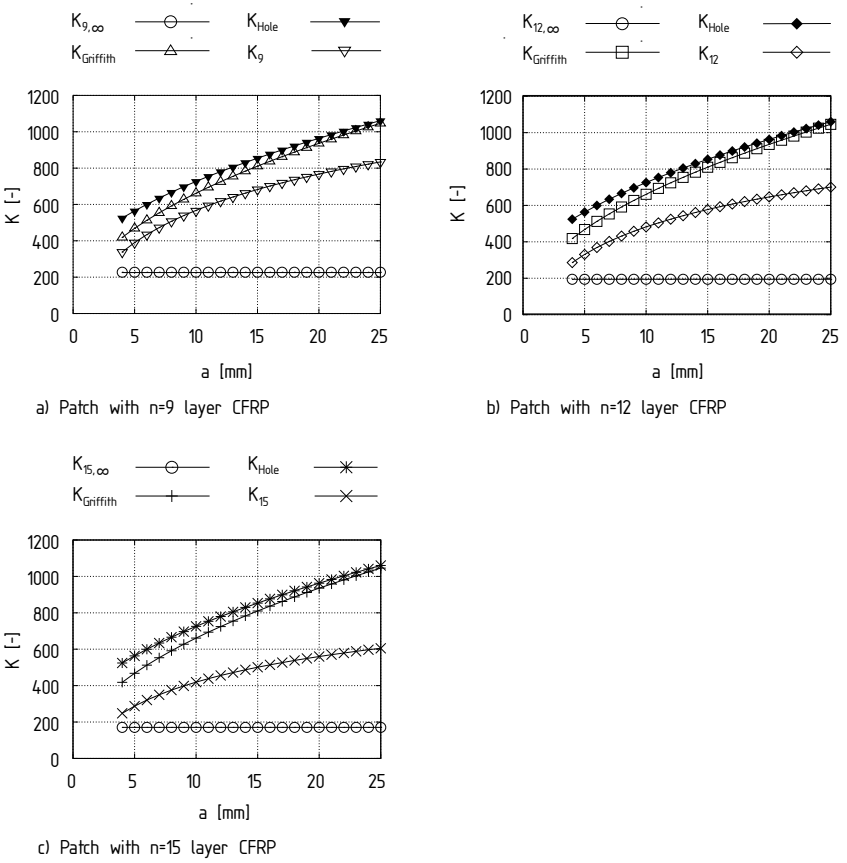

Figure 3.13: Comparison of theoretical stress intensity factors

$K_{0,\mathrm{hole}}$ of the unpatched specimens as a comparison. The graphs show that crack growth cannot be completely prohibited by any patch configuration, as K_{I}^{*} is already bigger than K_{∞} from the initial crack length a_i. But, for all patches applies that the stress intensity factor of the patched component $K_{\mathrm{I,i}}^{*}$ is smaller than the one of the unpatched component K_{Hole} and K_{Griffith}, meaning that crack growth rates can be slowed down for all patch configurations. Comparing the crack growth rates of the patched specimens among each other, the effect of the increasing patch thickness can be identified. The thicker the patch the lower the stress intensity $K_{\mathrm{I,i}}^{*}$.
Fatigue crack growth predictions are based on Paris' law using the material constants C^{P} and m^{P} as given in Table 3.2. Crack growth rates $\mathrm{d}a/\mathrm{d}N$ for a specimen without patch and specimens with $n_{\mathrm{ply}} = 9$, $n_{\mathrm{ply}} = 12$ and $n_{\mathrm{ply}} = 15$ layers CFRP are plotted in Fig. 3.14 as a function of the crack length a. For the unpatched specimens, the crack growth rate is only determined for the central hole with edge cracks. The graphs show the influence

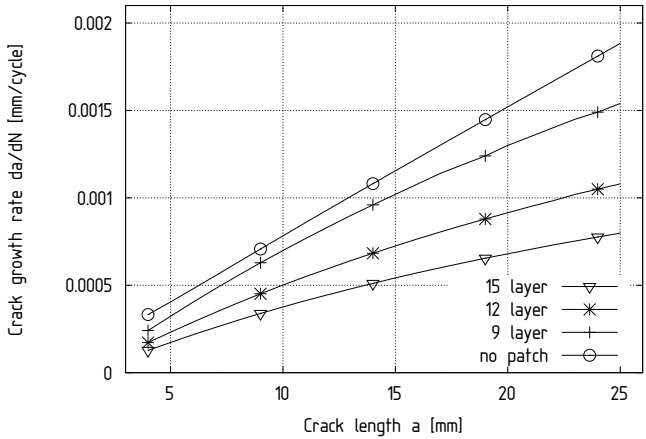

Figure 3.14: Theoretically determined crack growth rates of the three patch-thickness values compared to the unpatched specimen

of increasing patch thickness on the crack growth rate $\mathrm{d}a/\mathrm{d}N$. In accordance with the course of the stress intensity factors $K_{\mathrm{I,i}}^{*}$ the crack growth rate $\mathrm{d}a/\mathrm{d}N$ decreases with increasing patch thickness. The effect of patch thickness becomes stronger in the longer crack regime. What is more, it has

to be noted, that a linear increase in thickness has a non-linear effect on the crack growth rate. The difference between a patch thickness of 1.161 mm (9 layer) and a thickness of 1.548 mm (12 layer) is bigger than the difference between patches of 1.548 mm thickness and 1.935 mm thickness (15 layer). Thus, in the tested range one can say that, the thinner the patch, the bigger the influence of one additional layer CFRP on the crack growth reduction. The remaining fatigue life within a certain crack length range can be determined using the relation

$$N_{\text{remaining}} = \frac{1}{\left(\frac{m^{\text{P}}}{2} - 1\right) C^{\text{P}} (\Delta\sigma\sqrt{\pi}\, Y_{\text{I}})^{m^{\text{P}}}} \left[\frac{1}{a_{\text{min}}^{m^{\text{P}}/2-1}} - \frac{1}{a_{\text{max}}^{m^{\text{P}}/2-1}} \right]. \text{ [31]} \tag{3.19}$$

Exemplarily, the remaining fatigue life is are evaluated for a crack length range of $a = 7$ mm to $a = 14$ mm. Results are listed in Table 3.4. This

Table 3.4: Estimated fatigue life for $a = 7 - 14$ mm using Paris' law

Specimen configuration	Number of load cycles $N_{\text{remaining}}$
No patch	7795.7
9 layer	10006.05
12 layer	13931.25
15 layer	19539.55

means that within the evaluated range, an increase in fatigue life between 128.35% and 250% can be expected.

3.4 Test Description and Test Results

As listed in Table 3.3, there are 10 different specimen configurations. To capture statistical scatter, each configuration with a patch is tested three times. Additionally, six specimens without a patch are tested, three with and three without the same heat treatment as the patched specimens. To achieve a high bonding quality, specimen preparation is done carefully according to the recommended application process by Cytec[I], see [56]. For the

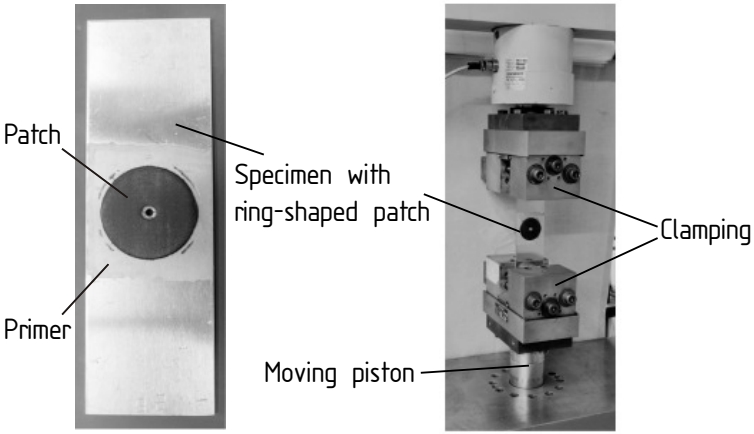

Figure 3.15: Picture of a specimen after thermal treatment and the test configuration

optimum joint performance, the corrosion prohibiting primer BR$^{\ddot{o}}$ 6747-1 is used. As recommended in the data sheet of the FM$^{\ddot{o}}$94M film adhesive, aluminium sheets are cleaned with acetone before etching the surface according to ASTM D-2651-79G [57].
The patches are made of an epoxy-based unidirectional (UD) CFRP prepreg. Circular punches are used to cut the specimens to the right dimensions. The patches are applied using one layer film adhesive orientating the fibres in load direction. The heat treatment is performed in a thermal chamber using vacuum to apply additional pressure. A picture of one specimen is shown in Fig. 3.15. The test machine is a servo-hydraulic test machine of type 85 Schenck POZ 160 with a static nominal load of +/-160 kN. One exemplary clamped specimen with patch is depicted in Fig. 3.15. The crack length a is measured (from the metallic side) at defined load cycles N with passive IrT. A more detailed description of this technique can be found in Chap. 4. Thus, for each specimen the crack length a can be displayed as a function of the corresponding load cycle N. It has to be noted that final failure is not recorded for all specimens. Therefore, test curves do not necessarily show the entire test length.

For each patch configuration, one exemplarily chosen specimen is presented to illustrate the test results. At first, the unpatched reference specimens show that the thermal treatment during patch application does not affect the fatigue properties of the material chosen, see Fig. 3.16. For the tests

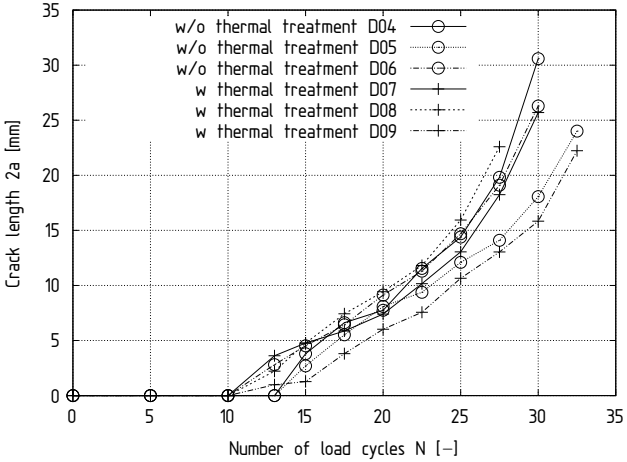

Figure 3.16: Crack length a over number of load cycles N for specimens without patch

performed, no difference between the specimens with and without thermal treatment can be found in the test results.
From the a over N curve, the crack growth rate $\mathrm{d}a/\mathrm{d}N$ can be determined as a function of the crack length a, see Fig. 3.17. The curve progression is approximated using a function of type

$$a = c_1 N^2 + c_2 N + c_3. \tag{3.20}$$

The constants $c_1 - c_3$ are fitted to the measured a over N gradient. To evaluate the influence of the two different variables, the effect of patch diameter and patch thickness on the crack growth rates are examined separately.

3.4.1 Influence of the Patch Diameter

The influence of the patch diameter on the crack growth rate is shown in Fig. 3.18. Here, the effect of the diameter variation compared to the un-

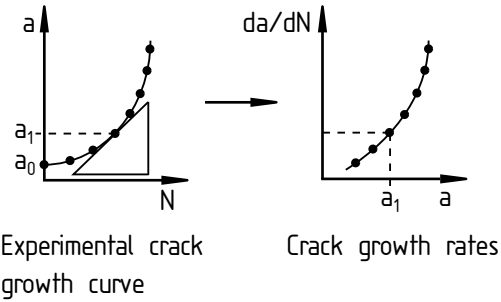

Figure 3.17: Determination of crack growth rates from fatigue test results according to [1]

patched reference specimen is plotted in form of the crack growth rate $\mathrm{d}a/\mathrm{d}N$ as a function of crack length a for a 9 layer patch in Fig. 3.18 a), for a 12 layer patch in Fig. 3.18 b) and for a 15 layer patch in Fig. 3.18 c). The graphs show that the increase in patch diameter reduces the crack growth rate, even though theory says that the diameter has no significant influence on the crack growth rate. In fact, the failure crack length can be increased. For the 9 layer patch, shown in Fig. 3.18 a), a patch of $d^{\mathrm{R}}_{\mathrm{outer}} = 22$ mm can already reduce the crack growth rate, but has no relevant effect on the maximum crack length. A slight but still not significant increase in maximum crack length can be recorded for $d^{\mathrm{R}}_{\mathrm{outer}} = 36$ mm. On the other hand, the crack growth rate on the other hand can considerably reduced, also compared to the $d^{\mathrm{R}}_{\mathrm{outer}} = 22$ mm patch. The increase to a patch diameter of $d^{\mathrm{R}}_{\mathrm{outer}} = 50$ mm shows a clear increase in maximum crack length, but no further decrease in crack growth rate. A similar behaviour can be seen for the 12 layer patch, shown in Fig. 3.18 b) and the 15 layer patch, shown in Fig. 3.18 c), respectively. Both figures illustrate that the increase in patch diameter decreases the crack growth rate. For the tested configuration, there seems to be a threshold curve, as all curves overlap for the thickest patch, see Fig. 3.18 c). A significant increase in maximum crack length can only be recorded for a patch diameter of 50 mm. Obviously, the crack bridging effect at longer crack length leads to a delay of final failure.

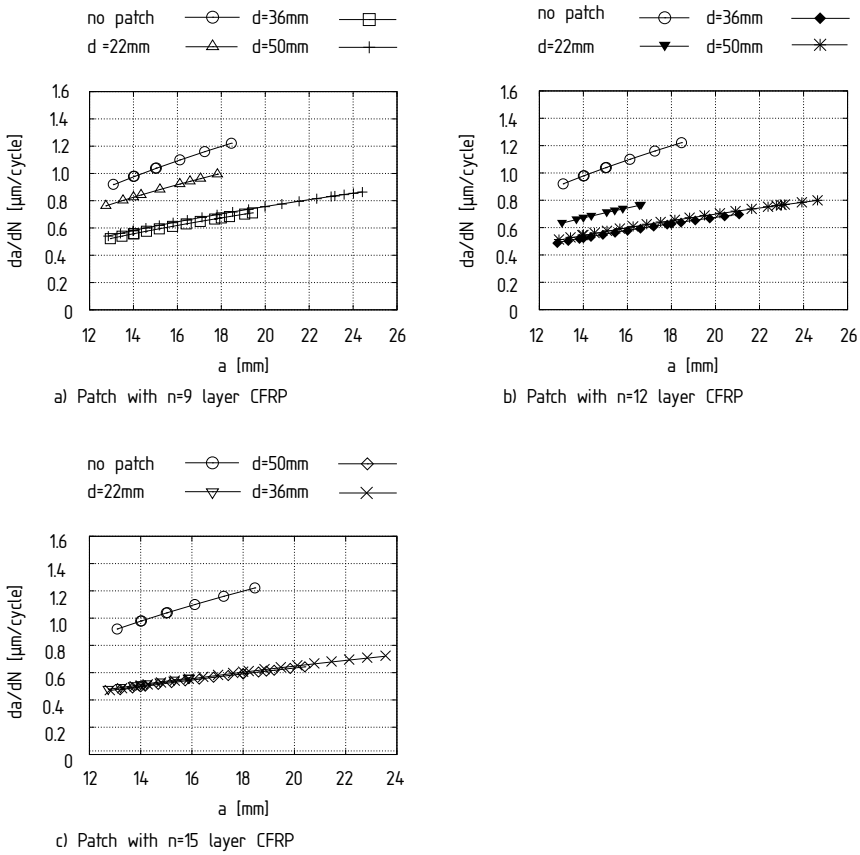

Figure 3.18: Influence of the patch diameter on fatigue crack growth rates da/dN

3.4.2 Influence of the Patch Thickness

The influence of the patch thickness on the crack growth rate is shown in Fig. 3.19. The curves are now sorted by the patch diameter to illustrate the influence of the patch thickness on the crack growth rate. As before, for each diameter, the effect of the thickness variation compared to the unpatched reference specimen is plotted in the form of the crack growth rate $\mathrm{d}a/\mathrm{d}N$ as a function of the crack length a. Fig. 3.19a) shows the results for an outer patch diameter of $d^{\mathrm{R}}_{\mathrm{outer}} = 22$ mm, Fig. 3.19b) for a diameter of $d^{\mathrm{R}}_{\mathrm{outer}} = 36$ mm and Fig. 3.19c) for a diameter of $d^{\mathrm{R}}_{\mathrm{outer}} = 50$ mm. The diagrams in Fig. 3.19 show that with increasing patch thickness, the crack growth rate can constantly be reduced. As seen before, for patches of the same diameter, the maximum crack length is not affected. The maximum crack length can be increased with increasing diameter and crack growth rates are reduced with increasing thickness.

3.5 Comparing Theory and Practice

To compare the test results, the evaluation range has to be defined. For this test series, the maximum initial crack length measured for all specimens is $a_{\mathrm{initial}} = 7$ mm, while the smallest maximum crack length detected is $a_{\mathrm{max}} = 14$ mm. These two values define the evaluation range. To determine the fatigue life between two distinct points, a numerical integration as presented in Eq. 2.5 is used. The remaining fatigue life of all specimens is shown in Fig. 3.20. The bars show the arithmetic mean of the test results for each configuration including error bars. Additionally, the results gained via numerical integration and the ones using Paris' law are depicted. Results show that for thin patches the fatigue life prediction is very conservative. With increasing patch thickness, estimations become more critical. To make results measurable, a safety factor is defined. In the context of fatigue life prediction, the term "critical" means that the remaining fatigue life is overestimated by the prediction method used. Failure of the specimen occurs before reaching the forecasted life span. The term "failure" is a question of definition including the definition of a critical crack length as well as final rupture of the specimen. It has to be defined individually for each application.

Material and component fatigue are always subjected to a certain statistical scatter. To increase the prediction quality, the scatter or statistical spread s

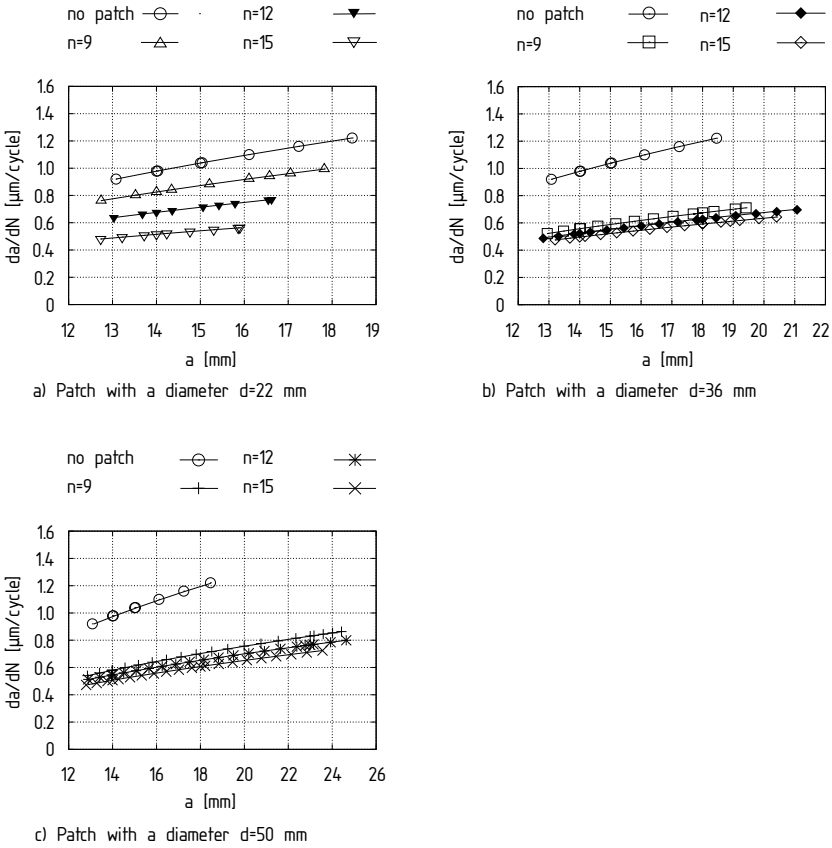

Figure 3.19: Influence of the patch diameter on fatigue crack growth rates da/dN

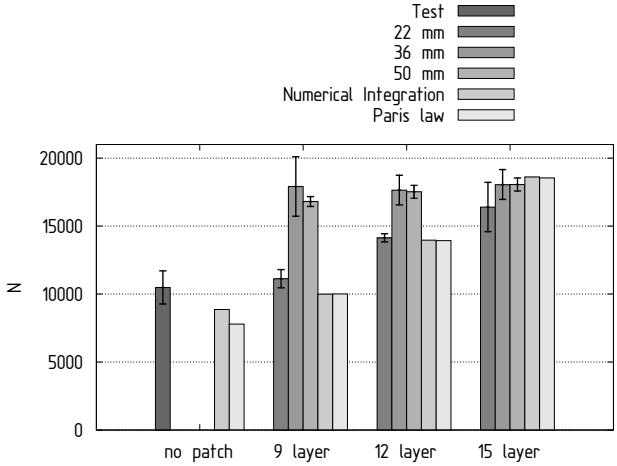

Figure 3.20: Remaining fatigue life cycles from test data and analytical considerations

should be considered. The statistical spread can be defined using for instance the sample variance

$$s = \sqrt{\frac{1}{n_{\text{sample}} - 1} \sum_{i=1}^{n} (\tilde{N}_i - \bar{N})^2} \tag{3.21}$$

where n denotes the sample number and $\tilde{N}_i$ are the number of load cycles at failure of each specimen i. The term $\bar{N}$ is the arithmetic mean of the sample n. The safety can be defined comparing the predicted fatigue life $\tilde{N}_{\text{predicted}}$ with the test samples. As soon as the predicted fatigue life $\tilde{N}_{\text{pre}}$ exceeds the sample scatter, the prediction becomes critical. Thus, the prediction method is defined to be critical for

$$jN_{\text{predicted}} > \bar{N} - s, \tag{3.22}$$

and thus the safety factor results to be

$$j = \frac{\bar{N} - s}{N_{\text{prediction}}}. \tag{3.23}$$

Table 3.5: Prediction quality assessment

		num. Int. j	Paris j
no patch		1.04	1.18
9 layer	22 mm	1.04	1.04
	36 mm	1.57	1.57
	50 mm	1.64	1.64
12 layer	22 mm	0.99	0.99
	36 mm	1.18	1.18
	50 mm	1.20	1.21
15 layer	22 mm	0.78	0.78
	36 mm	0.91	0.91
	50 mm	0.95	0.94

A safety factor of $j = 1$ means that the predicted number of load cycles corresponds to the actual number of load cycles applied within the defined crack length range, a safety factor $j < 1$ means that the prediction is critical and the fatigue life is overestimated.
The resulting safety factors for all specimen configurations can be found in Table 3.5. Comparing fatigue life estimations from Paris' law with the ones from the numerical integration, nearly the same values for the remaining fatigue life can be found. In the evaluated region, obviously neither the neglection of increasing crack length nor the use of the material constants from the plate material seem to have a negative effect on the prediction quality. For all specimen configurations the safety factor is close to "1", meaning that the prediction quality is very accurate, but not always conservative. For the specimens without patch, the safety factor is slightly higher than "1". This means that for unpatched specimens the prediction quality is good and tends to be conservative.
The analytical evaluation of the stress intensity factor K_{I}^{*} does not include the diameter. However, experiments show the positive influence of the diameter on the fatigue life. A plot of the safety factor j as a function of patch

diameter d is shown in Fig. 3.21. The horizontal line indicates the limit value of $j = 1$. For all three patch thicknesses, the safety factors increase

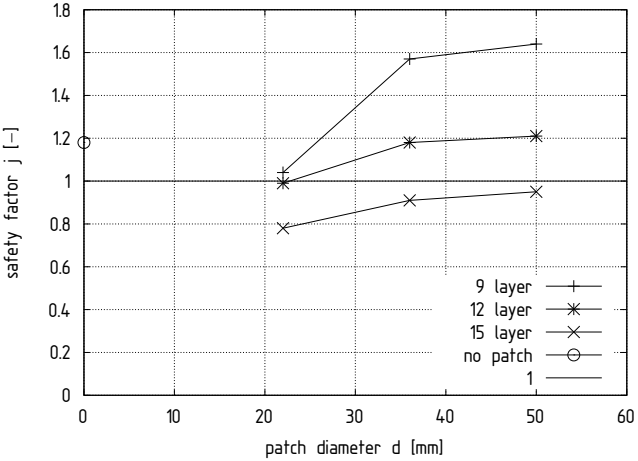

Figure 3.21: Safety factors of the fatigue life predictions using Paris' law

with increasing patch diameter. This means that with increasing diameter the prediction becomes more conservative. The effect is strongest for the thinnest patch with 9 layer CFRP. For a patch diameter of $d^{\mathrm{R}}_{\mathrm{outer}} = 22$ mm, the safety factor is around $j \approx 1$ for the 9 and 12 layer patches and even below the limit for the 15 layer patch ($j < 1$). For the 15 layer patch, the safety factor is still below 1, while it reaches values of around $j = 1.2$ and $j = 1.64$ for the 12 and 9 layer patches, respectively. Numerical integration and Paris' law are in very good accordance.
To sum up, fatigue tests give information on the crack length after a certain number of load cycles, while analytics result in a value for the stress intensity factor K^*_{I}, which is a measure for crack growth rates. A comparison of theory and practice can thus only be carried out indirectly by comparing the remaining fatigue life. Here, the determination of the crack growth rate $\mathrm{d}a/\mathrm{d}N$ goes along with an approximation of a versus N to gain a fitted function $a = f(N)$, that can be differentiated. For the analytical solution on the other hand, an approximation method like the Paris' law or numerical integration is needed to describe the crack growth rate as a function of the stress intensity factor, which usually uses material constants that in fact would have

to be determined for each tested patch configuration. Hence, either method includes its own inaccuracies and numerical errors. But, using a simple curve fitting procedure for the tests on the one hand and the material constants of the plate material for the theoretical approach on the other, the comparison of the resulting crack growth curves are in very good agreement. In the given example, the remaining fatigue life determined by using Paris' law leads to results which are comparable with the ones gained by numerical integration. In total, Rose's analytical model combined with Paris's law seems to be fairly robust for fatigue life predictions on coupon level, even when the patch geometry differs significantly from the theoretical models. However, it can also be concluded that predictions cannot be regarded to be conservative and the influence of an increased patch thickness tends to be overestimated. Overall, fatigue life predictions for the unpatched specimens are not significantly better than the ones for the patched components. Thus, more detailed analyses of the stress intensity factor K_{I}^{*} of crack patched structures are not expected to have a relevant impact on the prediction quality. In order to make bigger improvements, the consideration of continuously changing repair properties in the prediction methodology is recommended.

4 A Method to Improve the Performance Prediction

Damage processes in structural bonded aircraft repairs are mainly subsurface events. Varying mechanical and environmental loading during service can lead to a reduced repair functionality. The impact of multiple varying loads on the mechanical properties defines the long-term efficiency of the repair. The huge number of uncertainties that influence the service behaviour of a patch repair reduces the performance predictability drastically. Therefore, a comprehensive knowledge of the long-term properties under variable loading conditions is essential for a reliable prediction of the remaining service life. A realistic prediction of the actual service loads is one part of the challenge. The other is to predict the reaction of the object to certain loads. Decisive damage mechanisms in crack patched components are metallic crack growth and local patch disbond, which are both subsurface defects. The ability to monitor hidden damages under loading provides a fully new insight into the failure procedures of crack patched structures. With a monitoring method that is able to present the subsurface damage processes enables targeted studies on the parameters that determine the actual fatigue life, such as temperature changes, moisture, humidity or similar. Understanding the damage behaviour increases the ability to control the damage behaviour and thereby increases also the reliability of fatigue life estimations. Results and figures used in this chapter are based on preliminary publications, [58] and [59].

4.1 Requirements on the Monitoring System

One possible approach towards more reliable fatigue life predictions of crack patched components is to gain a comprehensive understanding of the on-

going damage processes under loading conditions. As subsurface processes are not visible from the outside, the demand for non-destructive inspection techniques arises to be able to visualize and thereby to assess the structural condition over time. For the improvement of the performance prediction, the influence of different loading mechanisms on the damage behaviour needs to be monitored. It has to be noted, that a differentiation has to be made between material degradation and physical damage. Material degradation is normally not detectable with common monitoring methods, whereas physical damages are. [23] Therefore, the present report focusses on physical damage only.
In the first step, the demands on the monitoring system have to be specified. In the given case, these demands can be summarized as follows: The method should

- be non-destructive,
- be applicable to all test levels,
- be easy to handle for the qualitative and comparative evaluation,
- comprise the ability to perform quantitative analyses,
- be applicable to moving objects under cyclic loading,
- be able to monitor metallic crack growth, patch disbonding at the patch metal interface and desirably inter-ply delamination at the same time and
- it should be applicable to tests under variable environmental conditions.

The terminology for non-destructive observation methods is not always consistent. In most cases, the term of non-destructive inspection, or simply NDI is used. It has to be noted that several non-destructive monitoring methods are commonly used for service inspections such as the detection of delaminations or similar, which is not the intention of the present study. To prevent misunderstandings, in the given context the term *non-destructive evaluation* (NDE) is preferred. In literature, several non-destructive measurement methods can be found in the context of crack patching. These methods are usually classified with respect to damage inspection, namely into methods for the inspection of adhesion failure, delaminations and disbonds and methods for the inspection of cracks in the parent structure under the patch. [60, 38]

For online damage evaluation, different conditions apply than for off-line damage inspection. During inspection, the damage may not be detectable in the unloaded case with one specific method, whereas it may well be detectable under loading conditions using another method. Other techniques might be applicable to non-moving objects but not to moving ones. Considering the specific demands of the given application, this classification does not apply to the term NDE as it is used here.

4.2 The Method of Infrared Thermography

Among others, the diverse techniques of IrT are already common practice in the quality assessment of bonded structures and composite parts in the aviation industry. [61] IrT methods largely meet the given requirements: IrT is non-destructive, it can be used for tests from coupon size to component size level, and is, at least to a certain extent, applicable under changing environmental conditions. Thermal image evaluation can be performed in a qualitative, a comparative and a quantitative manner. [62] The first two are rather simple to perform, while quantitative analyses can be elaborate. Different IrT methods have further shown good results in detecting subsurface defects in crack patching, both for NDI and NDE [63, 64, 65]. The term IrT is a generic term comprising different thermography methods. All methods have in common that they measure a heat flow in terms of infrared radiation. The technique of IrT can be divided into "active" and "passive" methods depending on the heat source. Active methods use an external energy source that actively induces a heat flow within the object, which then can be detected. Active IrT can be subdivided related to the thermal excitation method. Common active methods are for instance (optical) lock-in thermography (LT), or pulse phase thermography (PPT). On the contrary, passive IrT measures the internal heat flow and is thus not further divided. [66] Active IrT methods are common practice in NDI and passive IrT is common practice in the evaluation of crack growth.
Crack growth analyses using passive thermography, as well as the subsurface defect inspection using active techniques are only a few examples for the common practice in IrT. [66, 67, 68] Several studies can also be found in the context of crack patching. Active thermography methods show good efficiency in subsurface crack and disbond detection and inspection. [63, 69]

The method of LT can be applied to detect artificially introduced defects at the patch-metal interface as well as between different layers in the unloaded state. It is further capable to monitor patch disbond under fatigue loading. [64] Aside from that, be used to monitor patch disbond growth in a qualitative and quantitative manner. [70, 71, 72]
Compared to other methods, IrT has proven its applicability to monitor cracks underneath FRP patches [73, 63] as well as patch disbond or interlaminar patch delamination [73, 63, 74, 64]. Also the principle observability of stress concentrations in the substrate underneath the patch under fatigue loading conditions has bee proven. In terms of monitoring the crack growth behaviour of pure metallic structures under quasi-static [75, 76, 77] and cyclic loading passive IrT showed promising results. [78]
To sum up, subsurface defects are usually assessed using active thermography methods in the unloaded state, while passive thermography can be used to monitor damage propagation in loaded components. Here, the aim is to combine both, which means monitoring subsurface damage procedures under mechanical loading. Hence, passive IrT and active IrT is evaluated. For active methods, the method of optical LT is chosen. For the interpretation of thermal images it is important to know the basic principles and relevant features of the monitoring method used. A general survey of the operating mode of infrared thermography helps to arrange and to assess the test results. Functionality, possible benefits and drawbacks are therefore displayed.
Infrared radiation hitting a body is divided into the three components absorptance $A_{\tilde{\lambda}}$, reflectance $R_{\tilde{\lambda}}$ and transmittance $T_{\tilde{\lambda}}$

$$A_{\tilde{\lambda}} + R_{\tilde{\lambda}} + T_{\tilde{\lambda}} = 1, \tag{4.1}$$

which are all functions of the wavelength $\tilde{\lambda}$. The theoretical model of the black body says that any incident infrared radiation can be absorbed, which means that Eq. 4.1 can be reduced to

$$A_{\tilde{\lambda}} = 1, \tag{4.2}$$

where the absorptance α becomes independent of the wavelength λ. [79] This principle is used in IrT. Since reflectance interferes with the measurement, it should be close to zero. A surface with black body characteristics is therefore preferred for improved measurement results. [80] In practice, this means that the object's surface is covered by a thin layer of matt black coat for all tests presented in this study. Additionally, a refrigerated pack is mounted right behind the component to increase the thermal contrast to the surrounding environment.

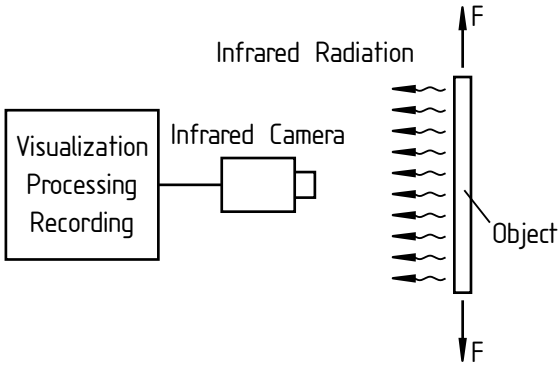

Figure 4.1: Sketch of the test setup for passive IrT

4.2.1 Passive Thermography

Literature describes passive IrT as a rather qualitative method, which is therefore often used for the comparative and qualitative assessment of damages procedures. [66] One common application is the observation of fatigue crack growth in metallic components. [81, 82] The principle of passive thermography is based on the instantaneous detection of temperature differences and changes. A sketch of the test setup illustrates the operation mode as it is used in the test series presented, see Fig. 4.1. Infrared radiation emanating from the loaded specimen is detected by an infrared camera. Changes or local differences are recorded. The camera is connected to a computer with a data processing and visualization software that enables to optically display the temperature distribution on the surface of the component surface. For more detailed analyses of the damage behaviour it is possible to perform advanced data processing methods that allow for qualitative assessments. [83, 84] For qualitative and comparative analyses as performed here, data processing methods provided by the camera software are sufficient.

The correlation between mechanical loading and temperature evolution is based on the so-called thermomechanical coupling. Looking for instance at a metallic structure loaded in tension movements in the atomic lattice structure go along with energy conversion processes, e.g. temperature evolution. [85] Linear-elastic tension results in a temperature decrease, while linear-elastic compression leads to a temperature increase. [86, 85] Similarly, also during plastic deformation irreversible energy conversion results in a temperature

increase. [87] Crack initiation and crack growth go along with local stress hot spots resulting in local plastic deformations. The formation of a plastic zone around the crack tip can thus be identified as a local temperature hot spot. [88]
Fatigue loading leads to a continuous temperature increase. Irreversible microstructural processes resulting from the time-depending thermoelastic coupling and the plastic energy dissipation lead to a continuous increase of the mean temperature. [89, 90, 91, 92] The identification of thermal hot-spots occurs by temperature difference ΔT to the surrounding material. An increasing mean temperature can therefore lead to reduced detectability.

4.2.2 Optical Lock-In Thermography

Active IrT methods make use of external thermal excitation to induce a heat flow. The principle setting of optical LT is sketched in Fig. 4.2. For optical IrT methods, the heat flow is commonly generated using an external heat source, such as a halogen lamp for instance. The method of LT uses an oscillating signal that periodically heats up the object from one side. The temperature modulation unit can either be positioned at the same side as the infrared camera or at the opposite side. [80] Results presented in the following are obtained from a test assembly having the thermal excitation and the measurement unit at the same side, as depicted in Fig. 4.2. The modulation is controlled by a computer unit and similarly as for passive thermography data processing helps to visualize the temperature distribution in the form of thermal images. Due to the oscillating temperature signal, phase and

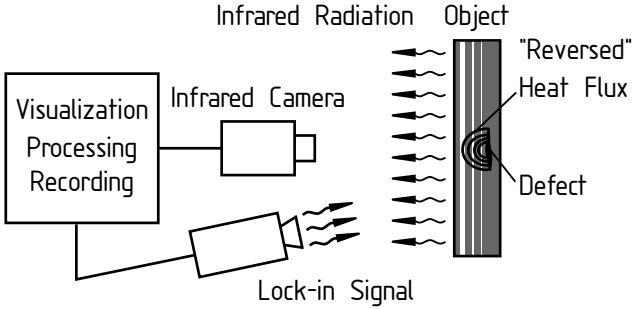

Figure 4.2: Principle of lock-in thermography according to Gleiter [93]

amplitude images are created showing the amplitude and phase shift of the thermal response. Here, phase images are chosen for test evaluation since they are usually considered to be more robust against "optical infrared surface features" [66] compared to amplitude images. [94] For the evaluation it has to be kept in mind that in contrast to amplitude images, phase images were found to be unable to display the specimen elongation of moving objects. [95] The heat flow through the component, which is created by the pulsed temperature signal follows the heat-flow equation. [96] In a homogeneous and isotropic material, the one-dimensional heat flow can be described by the differential equation

$$c_p \, \rho \frac{\partial}{\partial \bar{t}} = \kappa \frac{\partial^2 T(z, \bar{t})}{\partial z^2}. \tag{4.3}$$

In this equation T is the temperature, c_P is the specific heat, ρ is the material density, κ the thermal conductivity, $\bar{t}$ denotes the time and z the depth coordinate. [96] Depending on the assumptions made and the boundary conditions chosen, different solutions of this equation can be found in literature describing the temperature variation in the material depth as a time function.

At material boundaries the heat flow is partly "reversed". A homogeneous isotropic material and a uniform thermal stimulation provided, the result is an oscillating temperature profile, which is uniformly distributed on the surface. The time-depending varying temperature profile can be mathematically described by a wave function, the so-called thermal wave, even though it is physically not identical to electromagnetic waves. [97, 96, 98] For further information on thermal wave theory it should be referred to the relevant literature. [96, 97, 98] Any thermal discontinuity in the material results in local heat flow changes. [99] Literature often refers to this as the "reflection" of thermal waves. Differences in thermal properties lead to differences in the "reflection" of the thermal wave, which will be displayed on the thermal image. Since the thermal wave is not an electromagnetic wave, the term "reflection" may not be appropriate, but the theory of thermal waves and its physical meaning is already extensively discussed in literature and shall not be focused on here. The infrared camera system now records the oscillating surface temperature in time and space. Material discontinuities can be made out on the thermal image as local differences in temperature. To create an illustrative idea of the measurement principle, the wave analogy is helpful yet. Fig. 4.2 shows the principle effect of discontinuities such as defects on the temperature distribution. [66, 93] One solution for the heat flow differential

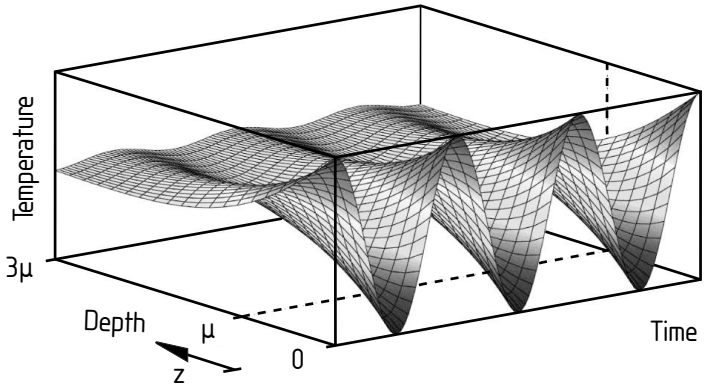

Figure 4.3: Temperature distribution as a function of time and depth

equation, Eq. 4.3, which is often referred to, is given by

$$T(z,\bar{t}) = T_0\, e^{z/\mu}\, \cos(2\,\pi\, f\, \bar{t} - \frac{2\,\pi\, z}{\kappa}).\ [66] \tag{4.4}$$

Here, μ is the so-called thermal diffusion length which comprises the thermal conductivity κ, the modulation frequency $\omega = 2\pi f$, the density ρ and the specific heat c_P in the function

$$\mu = \sqrt{\frac{2\,\kappa}{\omega\,\rho\,c_P}}.\ [66] \tag{4.5}$$

Funcion 4.4 is plotted in Fig. 4.3. With the thermal diffusion length, the possible measurement depth can be described as a function of the thermal modulation frequency. Thus, defect detection is restricted to a near surface region. [66] The software of the computer system connected uses a Fourier analysis to convert the signal into amplitude and phase images that are directly connected to the temperature distribution. In addition to the parameters given in Eq. 4.5, different additional factors further influence the measurement quality, such as surface roughness, or density changes from rolling processes. Thus, no general method is available to estimate the best measurement settings. Another aspect to be considered is that several stimulation periods are needed to obtain thermal images. [67] Here again, a general specification of the number of lock-in periods needed cannot be given, because

this aspect is also dependent on different parameters and has therefore to be evaluated individually. In conclusion, the lock-in parameter setting is rather based on experimental experience than on calculation.

4.3 Derivation of the Test Procedure

The following test series aims at approaching the question whether or not the NDE method of IrT is generally capable to analyse these two mechanisms under fatigue loading is approached. The aim is to optically analyse the reciprocal effects of metallic crack growth and patch disbond in single-sided patch repairs with either passive IrT or optical LT, or even both methods. A special focus has to be set on the adhesive bonding, as the bonding quality significantly controls the damage behaviour. A number of different test series is performed in order to approach the question of how metallic crack growth and patch disbond can be analysed individually and at the same time working round to possibilities and constraints of the two chosen monitoring methods. To be able to interpret thermal images, the two damage mechanisms are analysed separately at first. Only when the appearance of each defect and its propagation is examined individually, it is possible to analyse the combination of both. The design of the test procedure follows these four questions:

1. Is it possible to visualize multiple defects at the same time and to distinguish a metallic crack from patch delamination?
2. What does adhesive damage progress look like on thermal images?
3. What are the indicators to detect metallic crack growth?
4. What information can be gained while monitoring a patched component that can improve the understanding of the fatigue damage process?

4.3.1 Test Setup to Visualise Multiple Damages

Image interpretation is difficult for specimens with several different possible damage types, as long as neither the sort of damage nor its position is known. Therefore, simplifications have to be made. The easiest degree of freedom to be limited is the damage progress. Thus, the specimen to be analysed is not loaded. Remembering that subsurface irregularities are not detectable with passive IrT without loading, this implies that only the method of LT can be

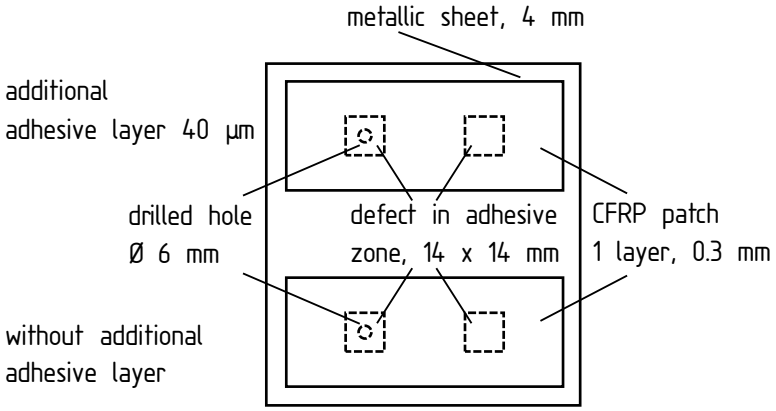

Figure 4.4: Specimen geometry of the preliminary test

used. Artificially introduced damages make sure that size and location of the damage is known. The specimen design is sketched in Fig. 4.4. Since fatigue cracks often occur at drilled holes, a simple metallic plate with drilled holes, 6 mm in diameter, is chosen to represent the damaged parent structure. To simulate the repair patch, strips of carbon fibre reinforced plastics are bonded to the plate. Two different patch configurations are tested, one with an extra adhesive layer (upper patch) and the other one using the epoxy itself for joining the two components (lower patch). Under each strip two defects can be found. To simulate local patch disbond, small squares of newsprint are used. For each strip one is placed directly over the hole (left-hand side) and the other just between patch and metal (right-hand side). To make sure that no other inter-laminar defects influence the results, only one layer CFRP prepreg material is applied. The defect on the right-hand side is used to calibrate the lock-in parameter to the defect depth, while the defect on the left-hand side is designed to find out whether or not metallic defects can be detected under disbonded areas.

Table 4.1: Material data preliminary test

Plate material		S235JR+AR
Thickness	t^{P}	4 mm
Patch material		MD CFRP prepreg C W410-TW2/2-E323/42%/6k
Ply thickness	t^{R}	0.6 mm
Adhesive		Film adhesive DuploTEC 10400
Thickness	t^{A}	0.04 mm

4.3.2 Test Configuraton to Monitor the Adhesive Damage Progress

To analyse patch disbonding and adhesive failure under fatigue loading, a conventional DOFS specimen is chosen. This specimen geometry is considered to represent the inner part of a double-sided patch repair, as illustrated in Fig. 4.5. As mentioned before, LT is not designed for the analysis of mov-

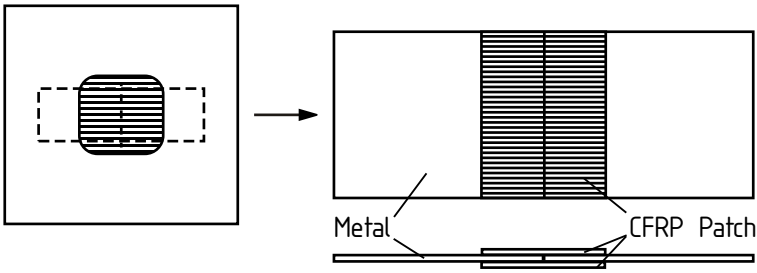

Figure 4.5: Patch Repair

ing objects since it is not a continuous measurement technique. Remembering that for LT one single image is created by applying several lock-in periods onto the specimen, which means that the creation of only one picture is time-dependent. Hence, under mechanical loading the damage size and occurrence can vary while taking the picture. Even though piston movement is rather small, the specimen is not in a steady state during the imaging process. So it

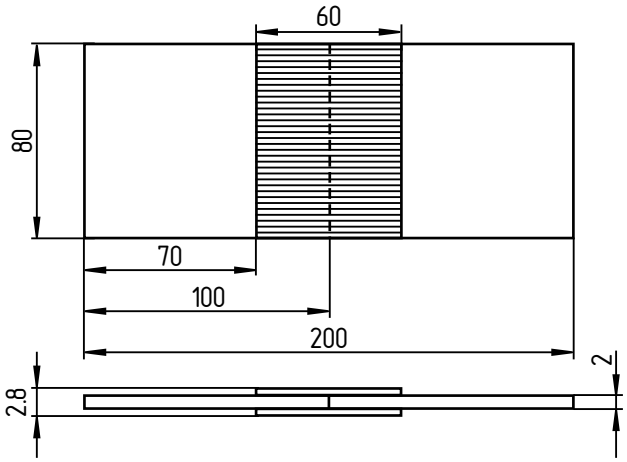

Figure 4.6: Specimen geometry DOFS

is important to understand that pictures gained via LT can only give a qualitative idea on damage size and and outlines, but do not give exact values. To be able to monitor the damage progress, several images have to be taken using LT. Therefore, the specimen width is increased compared to the standard geometry. The dimensions chosen are depicted in Fig. 4.6. To make sure that delamination occurs only at the patch metal interface, only one layer of CFRP is used. With these modifications the specimen configuration is considered to be appropriate for the analyses with passive IrT and LT.

Table 4.2: Material data DOFS

Plate material		Aluminium 5083
thickness	t^{P}	3 mm
Patch Material		MD CFRP prepreg C W410-TW2/2-E323/42%/6k
Ply thickness	t^{R}	0.6 mm

4.3.3 Indicators for Metallic Crack Growth

The easiest way to monitor metallic fatigue crack growth is to use metallic specimen without patch, or a single-sided repair patch monitored from the unpatched side. Due to its minor dimensions, crack detectability might be limited, especially using LT. One indicator for the crack length could be the plastic zone around the crack tip that forms during the loading process. A simple estimation of its size helps to arrange expectations. Presuming plane stress conditions and a circular shaped plastic zone, for Al 5083 the size of the plastic zone can be estimated to have a diameter of

$$r^P = \frac{1}{\pi}\left(\frac{K_I}{R_{p0.2}}\right)^2 \approx 0.027889 \text{ mm. [31]} \tag{4.6}$$

This dimension lies within the resolution of the camera and might therefore be detectable on the thermal images as long as the loacl temperature increase is high enough.

4.3.4 Test Configuration to Monitor the Progress of Multiple Damages

To stay with the application of a rivet hole, the specimen geometry chosen has a central hole, see Fig. 4.7. In contrast to the test series presented in Chapter 3, no protruding rivet head is presumed here and thus the hole is completely covered by the patch. Single-sided repair patches are applied in order to be able to also monitor only metallic crack growth. Again, only one layer of CFRP is used to avoid inter-laminar failure that can detract the interpretation of the thermal images. The material data listed in Table 4.2.

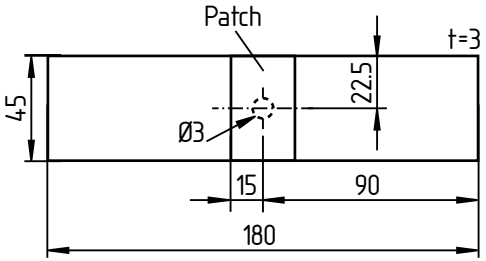

Figure 4.7: Specimen geometry fatigue test with combined defects

4.4 Test Description and Test Results

The camera system used for all tests is of type ImageIR$^{\circ}$ 8380 S (InfraTec GmbH, Dresden, Germany) in combination with a tele-zoom lense ($\bar{f}$ = 50 mm). It uses a Stirling cooler and has a noise equivalent temperature difference of 20 mK. The corresponding technical data is listed in Table 4.3. The thermal stimulation device used for optical LT is a halogen lamp of type

Table 4.3: Technical data of ImageIR$^{\circ}$8380 S

Spectral range	Image format	Temperature resolution	Temperature measurement range
2.0–5.7 μm	(640x512)IR pixel	25 mK at 30°C	-40–150°C
IFOV Instantaneous field of view	Framerate	Integration time	
0.3 mrad	300 Hz	1–20000 μs	

H25s (Hedler$^{\circ}$ Systemlicht GmbH, Runkel, Germany) with a power of 2.5 kW using two identical bulbs of 1.25 kW beam power each. For thermal image analyses the analysis software "IRBIS$^{\circ}$ 3 professional" is used for passive IrT and "IRBIS$^{\circ}$ 3 Active Online" (both InfraTec GmbH, Dresden, Germany) is used for LT. All specimens are coated with Dupli-Color Aqua matt black (MOTIP DUPLI GmbH, Haßmersheim, Germany) spray colour. Mechanical tests are performed with a servo-hydraulic test machine of type 85 Schenck POZ 160 with a static nominal load of +/-160 kN. All dimensions are given in mm. The test results of all tests performed are in good agreement. Therefore, for each test one specimen is exemplarily chosen to present the results.

4.4.1 Feasibility Check – Vizualisation of Metallic Damage and Patch Delamination

The preliminary test is a feasibility study and the specimen is not loaded. Thus, mechanical properties are secondary and the specimen preparation is kept simple. The metallic material used is a simple aluminium plate and a

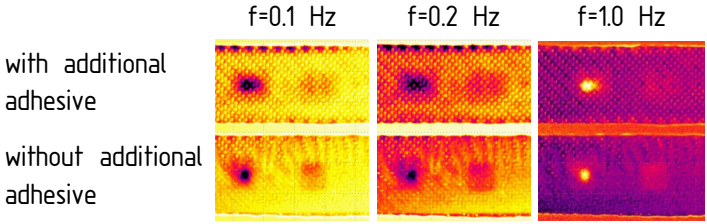

Figure 4.8: Test results of a defect combination at different lock-in frequencies

multidirectional CFRP layer. The adhesive tape used is of type DuploTEC 10400 (Lohmann GmbH & Co.KG, Neuwied, Germany). The metallic component is cleaned with acetone and patches with and without adhesive are applied directly to the component. Weights are put onto the specimens before putting them into a thermal chamber for 30 minutes under $140°C$.
To find out whether LT is capable of detecting both defects at the same time, at first, the appropriate lock-in frequency has to be identified. Fig. 4.8 shows the thermal images for the lock-in frequencies of $f = 0.1$ Hz, $f = 0.2$ Hz and $f = 1$ Hz, each test using 15 lock-in periods. For all frequencies tested, the square defect on the right hand side of each picture is clearly visible. On the left hand sides on the other hand, the square damage as well as the hole in the metal can be detected. This means that the detection of both defect types is possible within a certain range of lock-in frequencies.
It is further obvious that the outlines of the defects are more clearly visible for the bottom row without an additional adhesive layer than for the one with an adhesive layer. For a service application, the additional adhesive and usually also a primer have to be used in order to guarantee a proper bonding. Due to the hazard of contact corrosion, a patch made of CRFP will furthermore never be directly bonded to an aluminium structure without a corrosion inhibiting primer. It is therefore expectable that the adhesive layer has an impact on the monitoring properties. Nevertheless, in the given configuration, defects are visible for both configurations.
In conclusion it can be stated that LT is generally capable to detect a damage in the metallic part of a patch repair that is lying underneath a local disbonding of the patch. Since a hole of ∅ 6 mm is not representative in its dimensions for a fatigue crack, the applicability of this method to detect smaller cracks thus needs to be further analysed. Statements concerning the influence of patch thickness or other material configurations cannot be made

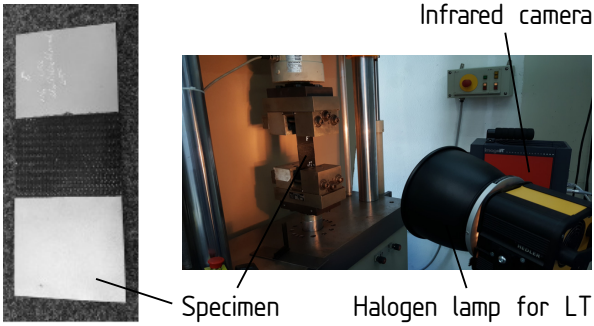

Figure 4.9: Specimen and test configuration DOFS with optional LT

either. Since the layer of the damage at the patch/metal interface is in direct contact to the damage in the metallic structure, the depth range here is very small. Within a frequency range from $f = 0.1$ Hz to $f = 1.0$ Hz, both defects are detectable in a metallic sheet of 4 mm thickness and one layer CFRP patch with the best results for $f = 0.2$ Hz. The procedure of finding the right lock-in frequency is usually very time-consuming. Results show that it is indeed difficult to find the "right" frequency, but it can still be possible to get useful results, even though conditions are not ideal. For the interpretation of the thermal images, it has to be remembered, that these images are a two-dimensional illustration of a depth range so that possible unknown material discontinuities lying within the analysed range can influence the results.

4.4.2 Monitoring Adhesive Damage Progress

To monitor solely adhesive damage progresses, the DOFS specimen was chosen. Four specimens are tested, two monitored with LT and two with passive IrT. The specimens are made of simple steel (St235JR+AR) and patches are made of $+/-45°$ woven CFRP fabric type C W410-TW2/2-E323/42%/6k (Carbon-Werke, Wallerstein, Germany) and a ply thickness of h=0.6 mm. The specimen preparation is the same as used in the preliminary test. The specimen and test configuration are depicted in Fig. 4.9, fatigue loads are listed in Table 4.4. Every 20000 load cycles the specimen is recorded for 5 seconds using passive IrT. Subsequent LT images are recorded. To be able to interpret the thermal images, a first estimation of the origin of the point is made using the quarter model presented in Fig. 3.6. The qualitative stress

Table 4.4: Test parameter for the double lap joint tests

Parameter		Value
mean force	F_{m}	3 kN
force amplitude	F_{a}	2.545 kN
stress ratio	R	0.1
test frequency	f	10 Hz
lock-in frequency	f	0.2 Hz
number of lock-in periods	n	10
framerate Passive IrT	f	40 Hz

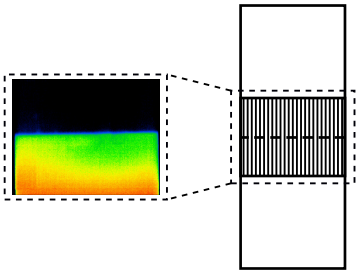

Figure 4.10: Detail shown in the damage evaluation

distribution of such a joint with adherends of different stiffness EA is shown in Fig. 3.7. In the given case, the stiffness of the metallic adherend is bigger than the one of the reinforcing patch $(EA)^{\mathrm{P}} > (EA)^{\mathrm{R}}$. For the chosen specimen configuration, this means that adhesive failure is expected to start from the free ends of the metallic butt joint, where stresses are highest.
To examine the adhesive damage progress, only the part of the specimen covered by the patch is evaluated, as shown in Fig. 4.10. Pictures taken at different load cycles display the damage progress over time. Since the temperature of the entire specimen increases over time, the colour scheme is different for all pictures and can thus not be compared directly. Thus, temperature scales are left out, as they do not give any supplemental information.

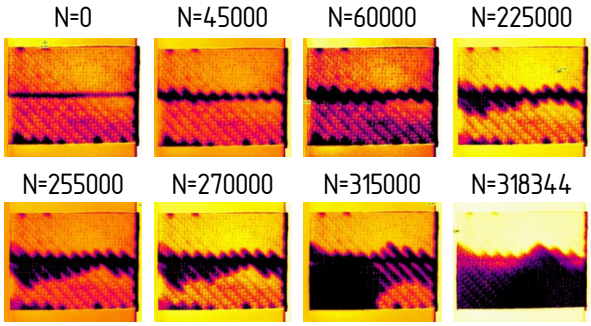

Figure 4.11: Adhesive damage progress under cyclic loading monitored with LT

4.4.2.1 Lock-in Thermography

At first, the method of LT is analysed. A sequence of thermal images from load cycle $N = 0$ to failure at $N = 318344$ depicts the adhesive damage progress, shown in Fig. 4.11. The first image shows the specimen before the test. The horizontal line in the centre shows the butt joint of the two metallic parts of the specimen. The diagonal structure results from the woven fibres. Dark spots at the bottom edge of the patch point to a weak bonding, especially at the left-hand side. The second image, taken after around $N = 45000$ load cycles, shows a first degradation of the adhesive bonding. Around the butt joint, where shear stresses in the adhesive are expected to be highest, dark spots form with outlines described by the diagonal pattern of the fibres. With an increasing number of cycles N, also the dark area expands. From load cycle N =225000 to N=315000 the dark area spreads mostly over the lower part of the specimen, particularly at the left-hand side. Outlines are blurred. This can be explained by the fact that several lock-in excitations are needed to produce one thermal image. The constantly moving piston leads to a slight, burt constantly varying position shift, so that sharp edges cannot be expected.
The last image shows one of the load cycles immediately before final failure of the specimen. The entire part below the butt joint now appears dark. Adhesive damage at the patch/metal interface seems to be visible as dark areas on thermal images gained via LT. To support this perception, a direct comparison between the last thermal image taken and a photograph of the damaged specimen is shown in Fig. 4.12. Looking at the damaged specimen, the first thing that attracts the attention is that the lower metallic plate is

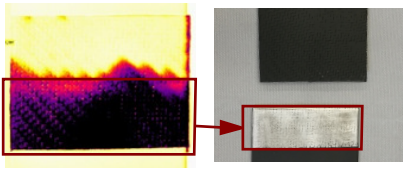

Figure 4.12: Comparison of thermal image (LT) and damaged specimen

completely separated from the patch, while it is still somehow bonded to the upper part. This goes along with the assumption that local disbond of the patch appears dark on the thermal images compared to the areas of proper bonding.
In total, the method of LT can visualize local disbond areas at the patch/metal interface. The displayed area gives a good qualitative idea on where damage is formed and how it propagates. With the operating mode of the monitoring method, or more precisely, with the time it takes to generate one picture, it can be explained that a quantitative measurement is not possible. Nevertheless, it gives a realistic impression of the damage size, as long as the damage progression and the piston movement are slow and small enough. Another observation that can be made, is that the butt joint – that can be seen on the very first image – cannot be distinguished from the disbonded area. Therefore, with the method of LT it might be difficult to detect both, the metallic crack and locally disbonded areas at the same time.

4.4.2.2 Passive Thermography

Secondly, the method of assive IrT is examined. For distinct load cycles the damage progress is illustrated in Fig. 4.13. Again, the first images show the specimen at the very beginning of the test, and again, a horizontal line in the centre assigns the butt joint between the two metallic sheets. Here, it is not identifiable as a dark line, but rather a colour – and thus – temperature difference between the upper and the lower metallic sheet. The woven structure of the patch is not visible and the surface seems to be homogeneous. Only on the right lower edge of the patch a slight shadow seems to be a sign of a weak bonding. The second image indicates that damage forms around the joint line, as expected. In a small area around the horizontal separating line, the diagonal pattern of the patch material appears, marked with a black edging. With increasing number of cycles, the area, where the woven pattern

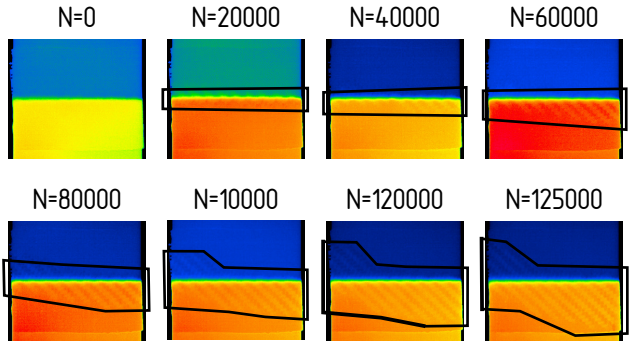

Figure 4.13: Adhesive damage progress under cyclic loading monitored with PT

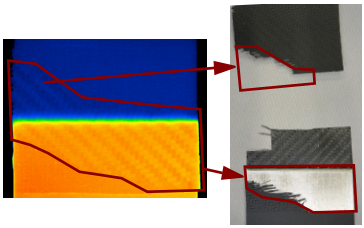

Figure 4.14: Comparison thermal image (LT) and damaged specimen

of the patch is visible, also increases, as can be seen in the following images. In a moving sequence of several pictures, this can be seen even more clearly. The area of local disbond increases mainly in the direction of the right lower edge, but also to the upper left one an increase in size can be detected. The last image shows the last picture taken before final failure. Comparing this image to the damaged specimen shows that observations on the thermal images are in good agreement with the photograph, see Fig. 4.14. Looking at the lower part of the specimen, at the lower left edge the patch is partly attached to the metallic sheet, while the rest of the patch is still bonded to the upper sheet. Loose fibres show that the patch is broken. Contour and size of the attached patch leftovers on the photograph coincide with the area on the thermal image, where the patch pattern on the lower half is not visible. Since the lower sheet is clamped to the moving piston, the temperature in the lower part of the specimens rises over time. The missing thermal bridge between both metallic parts results in an increasing temperature difference between

the upper and lower part, meaning that the butt joint is visible throughout the entire test. The visibility even improves over time.
In conclusion it can be said that passive IrT is capable to monitor the damage progress at the patch/metal interface. For the given specimen configuration, damage can be spotted as surface inhomogeneities showing the woven pattern of the CFRP patch. The distinction between damaged and undamaged areas is more difficult than for LT, but with increasing damage size also the visibility increases. The clear distinction between the upper and the lower metallic sheet leads to the assumption that metallic crack growth can be detected underneath the locally disbonded patch using PT.

4.4.2.3 Comparing Lock-in Thermography and passive Thermography

At last, a direct comparison between PT and LT is presented in Fig. 4.15 for three disctinct load cycles. Since both methods show one and the same specimen, the load cycle cannot be identical. Both methods were applied one after another. The comparison shows that the shape and also the size

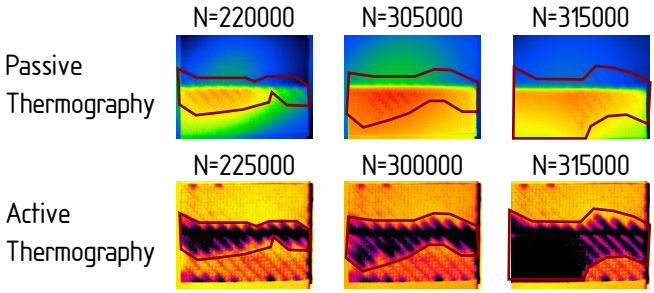

Figure 4.15: Direct comparison of damage visualization in PT and optical LT

of the detected disbond is very similar. The colour differences in the images resulting from the lock-in measurement are more clearly visible than the surface inhomogeneities on the thermal images from passive measurements. The butt joint on the other hand is much better detectable on the images gained with passive IrT. To monitor the overall damage process, it is thus suggested to predominantly use the method of passive IrT. The application of LT is much more effective and as soon as the patch completely detaches from the metallic structure around the crack, the crack tip is not expected to be

visible. Nevertheless, during testing some additional images should be taken to support the detection of local disbonds, especially for small damages.

4.4.3 Monitoring Metallic Crack Growth

All specimens used for this test series are made of Al 5083 (Hydro Aluminium, Oslo, Norway) and patches made of the same woven CFRP fabric as used for the DOFS, but applied in 0/90°-direction. After cleaning the metallic components of the specimen, the patches are applied. Instead of using weights, pressure is applied using vacuum. The specimens are cured for 2 hours under $T = 100°C$. Infrared data is recorded every 10000 load cycles for about 5 seconds. Test specifications are listed in Table 4.5 and the test setup is comparable to the one used before. This specimen and test configuration

Table 4.5: Test parameters combined defects

Parameter		Value
mean Stress	F_m	4 kN
stress Amplitude	F_a	3.272 kN
stress Ratio	R	0.1
test Frequency	f	10 Hz
lock-in frequency	f	0.2 Hz
number of lock-in periods	n	10
framerate passive IrT	f	100 Hz

applies for the test series presented in this and the following section 4.4.4. To see how metallic crack growth appears on thermal images acquired using passive IrT, specimens with single-sided patches monitored from the metallic backside are examined. Specimens with patch are used to be able to compare the crack growth behaviour with the specimens evaluated from the patched side, see section 4.4.4. The metallic crack growth process monitored from the unpatched side is shown in Fig. 4.16. It can be seen that for small cracks, the crack detectability is difficult. The temperature variation on the specimen surface is more or less continuously decreasing from the bottom to the top. The longer the crack grows, the better it can be made out on the thermal image. The crack restrains a continuous temperature distribution. Heat flows around the crack tip, and at the crack flanks the temperature escalates. With increasing testing time, the overall temperature increases and thereby

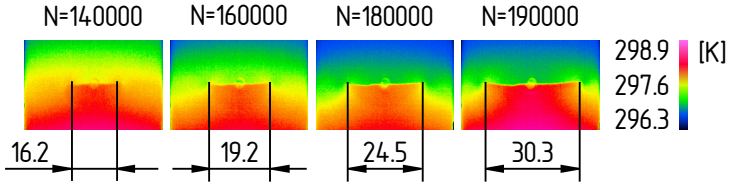

Figure 4.16: Monitoring metallic crack growth of a single-sided patched specimen using passive IrT

also the measurable temperature differences. What is more, the crack length increases and thereby the length of the area with an abrupt temperature rise. Both effects lead to an increased visibility.
In Addition, a circular area around the crack tip can be identified which forms during each loading cycle and vanishes while unloading the specimen. The circular area at the crack tip can be best identified on the last image presented (N =190000 load cycles) of the specimen with patch. It is difficult to measure the size of the circular area around the crack tip. The size varies in the course of a load cycle. Furthermore, contours are not clear cut, due to a rather continuous temperature gradient. The plastic zone was expected to be around $r_P \approx 0.028$ mm. The circular zone at the crack tip on the other hand is considerably bigger ($2 - 4$ mm), but helps to identify the crack tip and thereby to measure the crack length.
As estimated in Section 4.4.2, cracks in the metallic substrate are not visible as thin lines of different temperature. It is rather the increasing temperature difference of the surrounding material above and below the crack that helps to identify the crack. This becomes more visible when monitoring the moving specimen with the cyclic variation of crack opening and crack closure, which unfortunately cannot be displayed here, it can be seen even better. For those tests that monitor a patched specimen from the patch side, it is expected that, both metallic crack growth and local patch disbond can be made out on the thermal images.

4.4.4 Monitoring Metallic Crack Growth together with Adhesive Damage Progress under Fatigue Loading

Finally, this section addresses the essential question of whether or not, and to what extend IrT is capable of monitoring the overall damage process in crack patched structures. At first, the difference of the cyclic crack growth between the measurement from the metallic and the patched side is evaluated. Fig. 4.17 depicts the comparison of two patched specimens, one monitored from the metallic backside and the other one monitored from the patched side. As a matter of comparability, similar load cycles N are chosen. It can

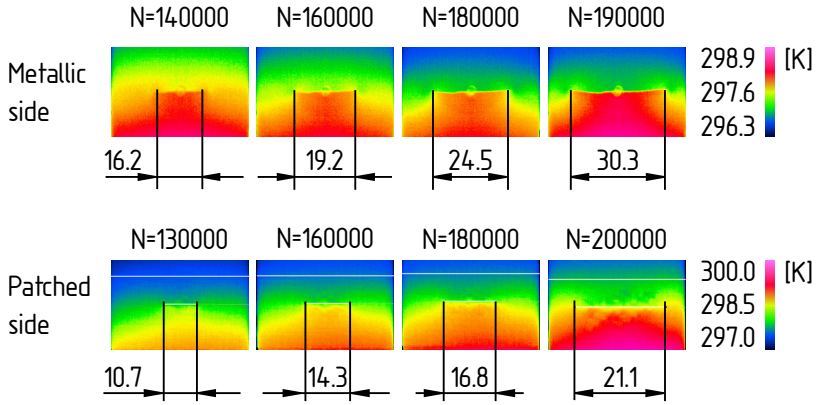

Figure 4.17: Comparison of the cyclic damage progress of one-sided patched specimens monitored from each side with passive IrT

be seen that the subsurface crack in the metal can be identified from the patched side nearly as good as from the metallic side. The temperature difference above and below the crack makes the crack visible and also the heat distribution on the left and right hand side indicate the crack tips. Any local patch disbond, on the other hand, is more difficult to see. For a small crack, the surface looks homogeneous. At load cycles N =160000 and N =180000 a small area around the crack seems to be disbonded, as the patch structure becomes visible. For a longer crack at N =200000 load cycles, the disbonded area is bigger, and thus easier to detect.
To gain additional information, one specimen is monitored with both, pas-

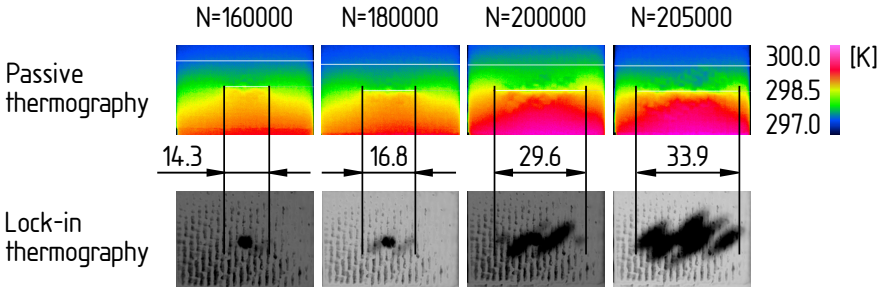

Figure 4.18: Cyclic damage progress monitored with passive IrT and LT

sive IrT and LT. The results can be seen in Fig. 4.18. As expected, the crack tip detection works better with passive IrT. For a small crack, the crack tip can only be guessed on the lock-in images. With increasing crack length also the disbond grows and the crack vanishes behind the dark area. Local patch disbond on the other hand is better identifiable on the lock-in images. The temperature difference between bonded and disbonded areas is easier to see than surface inhomogeneities. For both monitoring methods applies that with increasing disbond area, the capability of identifying adhesive damage increases as well. As both damage procedures can be detected at the same time, the method of IrT offers great opportunities in analysing the overall damage behaviour and possible mutual influences. For different patch configurations, it is possible to identify the driving damage mechanisms. Hence, the method of IrT provides very powerful tools to visualize the subsurface damage procedures of crack patched structures under loading conditions.

4.5 Summary and Discussion

With the NDE method of IrT it is possible to continuously monitor subsurface damage processes of crack patched structures. It has been shown that IrT methods are capable of monitoring the entire fatigue damage process, which includes metallic crack growth and local patch delamination at the same time. To this end, test results are very promising. In comparative studies it has been shown than the methods of passive IrT and optical LT constitute powerful techniques to visualize the entire cyclic damage progress in crack patched structures. Metallic crack growth as well as patch disbond can be identified on thermal images. It can be concluded that the use of LT is

much more laborious that the use of passive IrT. However, the results provide a more illustrative conception of position, size and shape of local disbonds as compared to passive IrT. What is more, the metallic butt joint could be identified even underneath disbonded areas. Due to the laborious handling compared to passive IrT and the uncertainties resulting from the movement of the specimen, passive IrT is preferred, though. Pulse phase thermography could be an alternative to optical LT thermography. Here, the component is activated by one excitation and the cooling behaviour is monitored. Differences in cooling time can be correlated with inhomogeneities.[66] Even though only comparative and qualitative analyses have been performed, results show that this method comprises great opportunities for the evaluation of the heterogeneous damage procedures. Additionally, for both methods, LT and passive IrT, advanced data evaluation methods exist that enable a quantitative assessment of the thermal images. [98, 100, 101] Possible limitations in defect detectability could be overcome by using advanced data processing techniques, which also provide the opportunity to determine quantitative results, see for instance [100, 98, 101]. With such methods, more detailed analyses of damage size and growth can be performed.
The ability to monitor the entire damage process at once enables targeted studies on the damage behaviour of crack patched components. The influence of environmental loads on the damage behaviour can be analysed and this knowledge can in return be used to make more realistic fatigue life estimations. Being able to assess the severity of a damage in a realistic manner can be used to reconsider the definition of patch wear-out. In a next step, the influence of temperature changes or other environmental influences on crack and disbond growth can be evaluated.

5 Conclusion

The goal to fully exploit the capabilities of crack patched components calls for reliable performance predictions. Research still focuses on the theoretical patch design process to get an even more precise description of the stress reduction resulting from the bonded patch. This approach disregards praxis effects that affect patch efficiency during service and thereby limits accuracy and reliability of fatigue life estimations. Additional new studies on patch efficiency centred around the initial stress intensity factor K_{I}^{*} of patched components do not advance the topic of crack patching. Within this research it has been shown that the focus has to be set on service loads and their effect on the damage behaviour of crack patched components.

5.1 Summary

Within this thesis, the goal of increasing the service life of a patch repair has been approached. Its findings can be summarized as follows:

1. **Breakdown of the patch design process**
   A detailed evaluation of the differences between the classical fatigue design process and the patch fatigue process has been performed in order to identify starting points for improvements.The general fatigue design process has been adapted to the specifications of a patched crack and extended to meet the supplementary demands. The disregard of continuous changes in stress intensity during service has been carved out to be the weak spot in conventional fatigue life prediction methods. In addition, two approaches have been identified to increase the service life of a crack patched structure – the reduction of the infant mortality and the delay of the patch wear-out phase. These two approaches have been chosen as starting points for more detailed analyses on the design process and performance prediction.

2. **Assessing the patch design process and predictiapplies that with increasing on methods**
   A test series has been designed to assess the quality of the fatigue life prediction using conventional design methods. The exemplary application of a rivet hole has been tested in a coupon test series with patches that differ in various aspects from the theoretical models used to determine the stress intensity factor K_{I}^{*}. Different patch configurations have been tested and compared with fatigue life estimations using Paris' law and numerical integration. Fatigue tests show that the crack cannot be completely restored with the chosen ring-shaped patch, but crack growth can significantly be reduced. Test results and theoretical predictions correspond well, even though differences between the theoretical model and the actual patch are considerable. Thus, additional studies on a more precise determination of K_{I}^{*} are not expected to have measurable impact on the prediction quality. The effect of a realistic prediction of the service performance is expected to be much more effective and it is therefore recommended to concentrate on the development of reliable fatigue life prediction methods.

3. **A possibility to improve performance predictions**
   In order to be able to redefine the term "patch wear-out", the damage controllability needs to be increased. This can be achieved by an improved understanding of the complex subsurface damage behaviour of crack patched components. The method of IrT has therefore been evaluated concerning its ability to monitor different possible damage processes and possible mutual interactions under service loads. It has been shown that passive IrT and LT are capable of monitoring crack growth and patch delamination under fatigue loading at the same time. With this monitoring technique it is thus possible to perform targeted studies on the damage behaviour under realistic environmental conditions, leading to a comprehensive understanding of the damage behaviour of crack patched components. This understanding can in return be used to increase damage controllability.

5.2 Outlook

The high number of uncertainties during service results in the demand for regular maintenance activities. Accessibility is often limited though and becomes costly when other components have to be removed. Therefore, the need for a robust monitoring system that continuously measures the repair condition comes up. The use of a sensor system by means of structural health monitoring (SHM) can permanently monitor the repair condition during service. Here, it is not necessary to analyse the individual degradation mechanisms separately and to evaluate mutual influences, since a sensor system monitors the response of the structure to the total of all degradation mechanisms. Concerning this, it has to be noted that patch efficiency cannot only be impaired by patch disbond, which is detectable with conventional NDE methods. Also a weak bondings, caused by a poor application conditions or environmental degradation, can lead to accelerated crack growth compared to an ideal bonding. The direct detection of weak bondings is not possible, only the effect of a poor patch quality is measurable in terms of crack growth rate acceleration. [23]
The most reasonable solution is to incorporate a sensor concept into the repair patch, which results in a "smart repair patch". [23, 38, 102]. The following demands on the sensor system can be derived:

- no detraction of patch functionality by the sensor,
- high probability of damage detection,
- reliable damage measurement, even for impaired adhesive bonding,
- robustness against environmental conditions,
- ability to detect adhesive defects and to measure crack length,
- cheap sensor development,
- fast data collection that is performable by any certified worker,
- simple sensor application,
- cheap sensor and
- suitable durability and product life-cycle.

Two philosophies can be followed with smart patches. One is the use of stiffener (not repair) patches for components prone to fatigue cracking. Here, a bonded patch is used to stiffen the structure and to prevent fatigue cracking. Thus, the focus lies on monitoring metallic crack growth. A sensor concept that proved to be capable to monitor metallic crack growth combined with a stiffening CFRP patch is the use of eddy current (EC) sensors. A first feasibility study performed at the "Institute of Structural Mechanics and Lightweight Design" at RWTH Aachen University has shown that EC sensors can be incorporated into CFRP patches using ultrasonic fabrication. A first test series using rivet hole stiffener patches as presented in Chapter 2 with additionally integrated EC sensors showed promising results. [103]
Another philosophy is to monitor the repair efficiency. Against the first impulse of monitoring metallic crack growth, here, the goal is to monitor the adhesive bonding, especially at the tapered ends. [104, 23] Remembering the damage tolerant and the safe life zone of a repair patch, see Fig. 2.12, the severest damage that impairs the patch integrity is patch peel off. Damages in the adhesive of the safe life zone lead to rapid patch disbond including the loss of the repair effect. But, the loss of the patch effect does not lead to instant failure of the metallic structure. In contrast, measuring the crack length gives no time to react. Reaching the critical crack length leads to rapid crack growth that cannot be counteracted. [23] Sensor concepts that seem to be applicable to monitor the adhesive bonding are for instance fibre Bragg grating (FBG) sensors, or piezoelectric transducers (PZT). Both methods have the advantage that they are capable to monitor both, patch disbond, and crack growth and have proven to be effective. [38] In terms of certification, also the combination of a "smart patch" with a preliminary proof test [105, 38] and other hybrid approaches are suggested in literature. [106]
Either way, further studies are needed to improve the performance predictability of bonded repair patches. By collecting data from service applications, the quality of service load estimations can be improved. The collection of general service information can be used as a database ("big data"). Thus, the knowledge of the overall performance of multiple applications helps to improve load and performance predictability by means of statistics. The more data is available, the higher the probability to derive a robust prediction procedure. The collection of damage data helps to predict service loads and the targeted analysis of their effects on the damage behaviour helps to assess the resulting damage behaviour. This results in a decrease of uncertainties concerning the long-term behaviour which can be used to redefine patch wear-out and thereby to extend the "useful time" of a patch repair.

List of Roman Symbols

A, Area, 41
$A_{\bar{\lambda}}$, Absorptance, 72
a, Crack length, 19

B_x, B_y, Patch dimensions in x and y-direction, 26

C, m, Paris constants, 18
c_1, c_2, c_3, Mathematical constants, 59
c_P, Specific heat, 75

d, Diameter, 35
$\mathrm{d}a/\mathrm{d}N$, Crack growth rate, 15

E, Young's modulus, 41

F, Applied load, 44
f, Frequency, 37

G, Shear modulus, 42

I, Moment of inertia, 53

j, Safety factor, 15

K, Stress intensity factor, 5
K^*, Stress intensity factor of a patched component, 11
K_b, Bending factor, 52
K_I, Stress intensity factor, mode I, 13
K_IC, Fracture toughness, mode I, 13
K_∞, Upper bound of the stress intensity factor, 29
$K_{\infty,\mathrm{el}}$, Upper bound with elastic adhesive, 54
$K_{\infty,\mathrm{pl}}$, Upper bound with plastic adhesive, 54
K_It, Stress concentration factor, mode I, 13
K_rms, Root mean square factor, 52

K_{th}, Threshold value, 17
k, Spring constant, 53

l, Length, 35

N, Number of load cycles, 15
$\bar{N}$, Arithmetic mean of number of load cycles, 64
$\tilde{N}$, Number of load cycles at failure, 64

R, Stress ratio, 5
$R_{\bar{\lambda}}$, Reflectance, 72
R_{m}, Static material strength, 46

S, Stiffness ratio, 41
s, Statistical spread, 62

T, Temperature, 75
$T_{\bar{\lambda}}$, Transmittance, 72
$\bar{t}$, Time, 75
t, Thickness, 35, 41

W, Rivet pitch, 37
w, Specimen width, 35

x, y, Cartesian coordinates, 26

Y, Geometry factor, 13

$\bar{z}$, Position of neutral plane of crack patched plate, 53

List of Greek Symbols

β, Adhesive factor, 41

η, Efficiency, 48

θ, Stress reduction factor, 25

κ, Thermal conductivity, 75

λ, Biaxiality, 46
$\tilde{\lambda}$, Wave length, 72

μ, Thermal diffusion length, 76

ν, Poisson's ratio, 43

ρ, Density, 75

σ, Tensile stress, 13
σ_{a}, Stress amplitude, 37
σ_{B}, Material strength, 48
σ_{m}, Mean stress, 37
σ_{Y}, Yield stress, 54

τ, Shear stress, 25

ω, Modulation frequency, 76

List of Acronyms

CCT, Centre cracked tension specimen, 35
CFRP, Carbon fibre reinforced plastics, 34

DOFS, Double overlap-joint fatigue specimen, 22

EC, Eddy current, 98

FBG, Fibre Bragg grating sensor, 98
FE, Finite element, 24

IrT, Infrared thermography, 9

LEFM, Linear elastic fracture mechanics, 11
LT, Lock-in thermography, 71

MROL, UK Aerospace Maintenance, Repair, Overhaul & Logistics Industry, 2

NDE, Non-destructive evaluation, 70
NDI, Non-destructive inspection, 70

PFM, Plastic fracture mechanics, 11
PPT, Pulse phase thermography, 71
PZT, Piezoelectric transducers, 98

QM, Quarter model, 41

SDS, Skin doubler specimen, 22
SHM, Structural health monitoring, 32

UD, Unidirectional, 58

Bibliography

[1] J. Schijve. *Fatigue of structures and materials*. Springer Science & Business Media, 2009.

[2] A.A. Baker and R. Jones, editors. *Bonded repair of aircraft structures*, volume 7. Martinus Nijhoff Publishers, 1988.

[3] J. Schijve. Fatigue of aircraft materials and structures. *International Journal of Fatigue*, 16(1):21–32, 1994.

[4] NORTH ATLANTIC TREATY ORGANIZATION. Aging aircraft fleets: Structural and other subsystem. Technical Report RTO-EN-015 AC/323(AVT-053)TP/33, North Atlantic Treaty Organization, March 2001.

[5] 02 Fatigue Requirements for Aircraft Structures. In *Aircraft Sustainment and Repair*. Butterworth-Heinemann, 2017.

[6] Bis research paper number 275. *UK Aerospace Maintenance, Repair, Overhaul & Logistics Industry Analysis*, (275), 2016.

[7] A.A. Baker. 01 Introduction and Overview. In *Advances in the bonded composite repair of metallic aircraft structure*. Elsevier, 2003.

[8] D. Roach and K. Rackow. 11 Development and Validation of Bonded Composite Doubler Repairs for Commercial Aircraft. In *Aircraft Sustainment and Repair*. Butterworth-Heinemann, 2017.

[9] C.N. Duong and C.H. Wang. *Composite repair: theory and design*. Elsevier, 2010.

[10] T. Stratford, J. Cadei, L. Hollaway, and W.G.Duckett. Ciria c595–strengthening metallic structures using externally-bonded. In *Advanced Polymer Composites for Structural Applications in Construction*, pages 693–700. Elsevier, 2004.

[11] D. Roach. Damage tolerance assessment of bonded composite doubler repairs for commercial aircraft applications. In *Sandia Report*.

[12] R.F. Wegman and T.R. Tullos. *Handbook of adhesive bonded structural repair*. William Andrew, 1992.

[13] A.A. Baker, L.R.F. Rose, and R. Jones. *Advances in the bonded composite repair of metallic aircraft structure*. Elsevier, 2003.

[14] R.Jones, A.A.Baker, N.Matthews, and V.K.Champagne. *Aircraft Sustainment and repair*. Butterworth-Heinemann, 2017.

[15] J.R. Weitzenböck and D. McGeorge. The designer's dilemma: How to deal with the uncertainty about the long-term performance of adhesively bonded joints. *Proceedings of the Institution of Mechanical Engineers, Part M: Journal of Engineering for the Maritime Environment*, 218(4):273–276, 2004.

[16] A. Pizzi and K.L. Mittal. *Handbook of adhesive technology, revised and expanded*. CRC press, 2003.

[17] H.S. Panda, R. Samant, K.L. Mittal, and S.K. Panigrahi. Durability aspects of structural adhesive joints. *Structural Adhesive Joints: Design, Analysis and Testing*, pages 97–134, 2020.

[18] M.D. Banea, M. Rosioara, R.J.C. Carbas, and L.F.M. Da Silva. Multimaterial adhesive joints for automotive industry. *Composites Part B: Engineering*, 151:71–77, 2018.

[19] R.D. Adams and W.C. Wake. The nature and magnitude of stresses in adhesive joints. In *Structural Adhesive Joints in Engineering*, pages 14–114. Springer, 1984.

[20] J. Comyn. Durability of adhesives in wet conditions. In *Adhesives in Marine Engineering*, pages 187–207. Elsevier, 2012.

[21] Y. Diamant, G. Marom, and L.J. Broutman. The effect of network structure on moisture absorption of epoxy resins. *Journal of Applied Polymer Science*, 26(9):3015–3025, 1981.

[22] A. Baldan. Adhesion phenomena in bonded joints. *International Journal of Adhesion and Adhesives*, 38:95–116, 2012.

[23] A.A. Baker, N. Rajic, and C. Davis. Towards a practical structural health monitoring technology for patched cracks in aircraft structure. *Composites Part A: applied science and manufacturing*, 40(9):1340–1352, 2009.

[24] P.P. O'Connor and A. Kleyner. *Practical Reliability Engineering, 5th Edition*. John Wiley & Sons, 2012.

[25] Australian Transport Safety Bureau. How old is too old? the impact of ageing aircraft on aviation safety. Technical Report Aviation Research and Analysis Report – B2005/0205, Australian Government – Australian Transport Safety Bureau, February 2007.

[26] S. Mohammadi. Parametric investigation of one-sided composite patch efficiency for repairing crack in mixed mode considering different thicknesses of the main plate. *Journal of Composite Materials*, 54(22):3067–3079, 2020.

[27] P.S. Shinde, P. Kumar, and V.K. Tripathi. Dependence of repair strength on the size of frp patch bonded to a cracked aluminum alloy panel. *Thin-Walled Structures*, 124:303–311, 2018.

[28] A. Aabid, M. Hrairi, J.S.M. Ali, and A. Abuzaid. Optimization of composite patch repair for center-cracked rectangular plate using design of experiment method. *Materials Today: Proceedings*, 27:1713–1719, 2020.

[29] S.S. Pradhan, U. Mishra, and S.K. Biswal. Experimental study on mechanical performance of cracked aluminum alloy repaired with composite patch. *Materials Today: Proceedings*, 26:2676–2680, 2020.

[30] S.M.A.K. Mohammed, R. Mhamdia, A. Albedah, B.A.B. Bouiadjra, , and F. Benyahia. Fatigue crack growth in aluminum panels repaired with different shapes of single-sided composite patches. *International Journal of Adhesion and Adhesives*, 105:102781, 2021.

[31] H.A. Richard and M. Sander. *Ermüdungsrisse*. Springer, 2009.

[32] D. Gross and T. Seelig. *Bruchmechanik*, volume 5. Springer, 2011.

[33] N.N. Certification specifications for large aeroplanes. Technical Report CS-25, European Aviation Safety Agency, September 2007.

[34] A.A. Baker. Repair efficiency in fatigue-cracked aluminium components reinforced with boron/epoxy patches. *Fatigue & Fracture of Engineering Materials & Structures*, 16(7):735–765, 1993.

[35] L.R.F. Rose and C.H. Wang. 07 Analytical Methods for Designing Composite Repairs. In *Advances in the bonded composite repair of metallic aircraft structure*. Elsevier, 2003.

[36] P.D. Chalkley, C.H. Wang, and A.A. Baker. 05 Fatigue Testing of Generic Bonded Joints. In *Advances in the bonded composite repair of metallic aircraft structure*. Elsevier, 2003.

[37] R. Jones, W.K. Chiu, and S. Hanna. Potential failure mechanisms of bonded composite repairs for metal and concrete. *Theoretical and applied fracture mechanics*, 21(2):107–119, 1994.

[38] A.A. Baker and J. Wang. 06 Adhesively Bonded Repair/Reinforcement of Metallic Airframe Components: Materials, Processes, Design and Proposed Through-Life Management. In *Aircraft Sustainment and Repair*. Butterworth-Heinemann, 2017.

[39] A. Vlot, S. Verhoeven, G. Ipenburg, D.R.C. Siwpersad, and H.J.M. Woerden. Stress concentrations around bonded repairs. *Fatigue and Fracture of Engineering Materials and Structures*, 23(3):263–276, 2000.

[40] J. Wiedemann. *Leichtbau: Elemente und Konstruktion*. Springer-Verlag, 2007.

[41] R. Jones, D. Peng, J.G. Michopoulos, and A.J. Kinloch. Requirements and variability affecting the durability of bonded joints. *Materials*, 13(6):1468, 2020.

[42] R. Jones and D. Hui. 08 Analysis, Design and Assessment of Composite Repairs to Operational Aircraft. In *Aircraft Sustainment and Repair*. Butterworth-Heinemann, 2017.

[43] H. Hosseini-Toudeshky, B. Mohammadi, G. Sadeghi, and H.R. Daghyani. Numerical and experimental fatigue crack growth analysis in mode-i for repaired aluminum panels using composite material. *Composites Part A: applied science and manufacturing*, 38(4):1141–1148, 2007.

[44] W. Hu, R. Jones, and A.J. Kinloch. 12 Computing the Growth of Naturally-Occurring Disbonds in Adhesively-Bonded Joints. In *Aircraft Sustainment and Repair*. Butterworth-Heinemann, 2017.

[45] C.H. Wang and C.N. Duong. *Bonded joints and repairs to composite airframe structures*. Academic Press, 2015.

[46] A.N. Rider, D.R. Arnott, and J.J. Mazza. 07 Surface Treatment and Repair Bonding. In *Aircraft Sustainment and Repair*. Butterworth-Heinemann, 2017.

[47] ASTM Standard. E647, standard test method for measurement of fatigue crack growth rates. *Annual Book of ASTM Standards, Section Three: Metals Test Methods and Analytical Procedures*, 3:628–670, 2002.

[48] Deutsches Institut für Normung e.V. *DIN 6791 – Halbhohlniete mit Flachrundkopf – Nenndurchmesser 1,6 mm bis 10 mm*. Beuth Verlag, Berlin, März 2011.

[49] J. Wiedemann and C. Kranz. Auswirkung eines Klebepflasters auf die Kerbspannungsintensität und dynamische Festigkeit einer angerissenen Scheibe. 1976.

[50] J. Wiedemann and M. Glahn. *Scheibe oder Membran mit Loch und aufgeklebtem Pflaster unter allseitigem Zug*. Universitätsbibliothek d. Techn. Univ. Berlin, Abt. Publikationen, 1974.

[51] O. Volkersen. Die Schubkraftverteilung in Leim-, Niet-und Bolzenverbindungen. *Energie und Technik*, 5(68):103, 1953.

[52] H.J. Bargel and G. Schulze. *Werkstoffkunde*. Springer-Verlag, 2008.

[53] H. Schürmann. *Konstruieren mit Faser-Kunststoff-Verbunden*, volume 2. Springer, 2005.

[54] K. Moser. Entwurf- und Berechnungsgrundlagen. In *Faser-Kunststoff-Verbund*. VDI-Verlag Düsseldorf, 1992.

[55] K.-U. Schröder. Vorlesung Leichtbau. Unpublished lecture notes.

[56] Cytec. FM® 94 Adhesive Film – Technical Data Sheet. Accessed : 2010-03-29, 2010.

[57] ASTM Standard. D2674–72,standard methods of analysis of sulfochromate etch solution used in surface preparation of aluminum. pages 1–3, Reapproved 2012.

[58] U. Martens and K.-U. Schröder. Evaluation of infrared thermography methods for analysing the damage behaviour of adhesively bonded repair solutions. *Composite Structures*, 240:111991, 2020.

[59] U. Martens and K.-U. Schröder. Monitoring multiple damage mechanisms in crack-patched structures using optical infrared thermography. *Fatigue & Fracture of Engineering Materials & Structures*, 2020.

[60] D. Roach. 17 Damage Tolerance Assessment of Bonded Composite Doubler Repairs for Commercial Aircraft Applications. In *Advances in the bonded composite repair of metallic aircraft structure*. Elsevier, 2003.

[61] B. Valseke B. Erhart. Non-destructive evaluation (nde) of aerospace composites: methods for testing adhesively bonded composites. *Composites Science and Engineering*, 2013.

[62] Deutsches Institut für Normung e.V. *DIN EN 16714-1 – Zerstörungsfreie Prüfung - Thermografische Prüfung - Teil 1: Allgemeine Grundlagen*. Beuth Verlag, Berlin, November 2016.

[63] N.P. Avdelidis, C. Ibarra-Castanedo, X. Maldague, D.P. Almond, and A. Seroulou. Thermal NDT & E of composite aircraft repairs. 2004.

[64] A.S. Paipetis, S.A. Grammatikos, E.Z. Kordatos, N.-M. Barkoula, and T.E. Matikas. In service damage assessment of bonded composite repairs with full field thermographic techniques. In *Nondestructive Characterization for Composite Materials, Aerospace Engineering, Civil Infrastructure, and Homeland Security 2011*, volume 7983, page 79831U. International Society for Optics and Photonics, 2011.

[65] A. Moropoulou and N.P. Avdelidis. Active thermography in the assessment of repaired aircraft panels. *Insight*, 44(3):145–149, 2002.

[66] X. Maldague. *Theory and practice of infrared technology for nondestructive testing*. John Wiley and Sons, Inc., New York, 2001.

[67] Deutsches Institut für Normung e.V. *DIN 54192 – Zerstörungsfreie Prüfung – Aktive Thermografie*. Beuth Verlag, Berlin, November 2010.

[68] R. Yang and Y. He. Optically and non-optically excited thermography for composites: A review. *Infrared Physics & Technology*, 75:26–50, 2016.

[69] S. Pavlopoulou, S.A. Grammatikos, E.Z. Kordatos, K. Worden, A.S. Paipetis, and T.E. Matikas. Continuous debonding monitoring of a patch repaired helicopter stabilizer: Damage assessment and analysis. *Composite Structures*, 127:231–244, 2015.

[70] S.A. Grammatikos, E.Z. Kordatos, T.E. Matikas, and A.S. Paipetis. Service and maintenance damage assessment of composite structures using various modes of infrared thermography. In *IOP Conference Series: Materials Science and Engineering*, volume 74, page 012006, Bristol, UK, 2015. IoP Publishing.

[71] S.A. Grammatikos, E.Z. Kordatos, T.E. Matikas, and A.S. Paipetis. On the fatigue response of a bonded repaired aerospace composite using thermography. *Composite Structures*, 188:461–469, 2018.

[72] S. Grammatikos, E. Kordatos andN. M. Barkoula, T. Matikas, and A. Paipetis. Repair integrity monitoring of composite aerostructures using thermographic imaging. In *Nondestructive Characterization for Composite Materials, Aerospace Engineering, Civil Infrastructure, and Homeland Security 2010*, volume 7649, page 76491D. International Society for Optics and Photonics, 2010.

[73] N.P. Avdelidis, A. Moropoulou, and Z.P. Marioli Riga. The technology of composite patches and their structural reliability inspection using infrared imaging. *Progress in aerospace Sciences*, 39(4):317–328, 2003.

[74] S.A. Grammatikos, E.Z. Kordatos, T.E. Matikas, and A.S. Paipetis. Real-time debonding monitoring of composite repaired materials via electrical, acoustic, and thermographic methods. *Journal of materials engineering and performance*, 23(1):169–180, 2014.

[75] T. Kathirvel, V. Raghu Prakash, and B. Krishnan. Thermographic assessment of tensile response of metals subjected to varying levels of plastic deformation. In *12 International Conference on Quantitative InfraRed Thermography*, 2012.

[76] H. Sakamoto, J. Shi, and D. Kumagai. Analysis of heat generation under plastic deformation, crack initiation and propagation. volume 30. WIT Press, 2001.

[77] M. Berković-Šubić, J. Frančeski I. Boras, J. Kodvanj, S. Švaić A. Rodić, and Z. Tonković. Application of ir thermography for determination of material properties. In *QIRT Conference Open Archives*, 2015.

[78] J. Medgenberg and T. Ummenhofer. Ortsaufgelöste Detektion von Ermüdungsvorgängen in metallischen Werkstoffen mit Infrarot-Thermografie. volume 08, pages 1–10. Thermografie-Kolloquium, 2007.

[79] R. Kneer. Vorlesung wärme- und stoffübertragung i. unpublished lecture notes.

[80] NN. *Einführung in Theorie und Praxis der Infrarot-Thermografie.* InfraTec GmbH, Infrarotsensorik und Messtechnik, Dresden, Germany, 2013. Schulungsunterlagen.

[81] P. Fernandez S. Seitl, J. Klusák and A. Fernández-Canteli. Comparison of analysis methods of data from thermographic measurements of al 2024 fatigue limit for r= 0.1. *Transactions of the VŠB – Technical University of Ostrava, Mechanical Series number2*, LIX(1969), 2013.

[82] T. Ummenhofer and J. Medgenberg. On the use of infrared thermography for the analysis of fatigue damage processes in welded joints. *International Journal of Fatigue*, 31(1):130–137, 2009.

[83] R. De Finis, D. Palumbo, and U. Galietti. A multianalysis thermography-based approach for fatigue and damage investigations of ASTM A182 F6NM steel at two stress ratios. *Fatigue & Fracture of Engineering Materials & Structures*, 42(1):267–283, 2019.

[84] J.C. Krapez, D. Pacou, and G. Gardette. Lock-in thermography and fatigue limit of metals. *Office National d'Etudes et de Recherches Aerospostaiales ONERA-PUBLICATIONS-TP*, (187), 2000.

[85] F. Maquin and F. Pierron. Heat dissipation measurements in low stress cyclic loading of metallic materials: From internal friction to microplasticity. *Mechanics of Materials*, 41:928–942, 2009.

[86] W. Weber. Ueber die spezifische Wärme fester Körper, insbesondere der Metalle. *Annalen der Physik und Chemie*, 10:177–213, 1830.

[87] M.P. Luong. Infrared thermographic scanning of fatigue in metals. *Nuclear engineering and design*, 158(2-3):363–376, 1995.

[88] N. Ranc, T. Palin-Luc, P.C. Paris, and N. Saintier. About the effect of plastic dissipation in heat at the crack tip on the stress intensity factor under cyclic loading. *International Journal of Fatigue*, 58:56–65, 2014.

[89] J. Medgenberg. *Investigation of localized fatigue properties in unalloyed steels by infrared thermography.* PhD thesis, Technischen Universität Carolo-Wilhelmina zu Braunschweig, 2008.

[90] A. Read. The internal friction of single metal crystals. *Physical Review*, 58:371–380, 1940.

[91] A.V. Granato and K. Lücke. Theory of mechanical damping due to dislocations. *Journal of applied physics*, 27(6):583–593, 1956.

[92] N. Ranc, T. Palin-Luc, P.C. Paris, and N. Saintier. About the effect of plastic dissipation in heat at the crack tip on the stress intensity factor under cyclic loading. *International Journal of Fatigue*, 58:56–65, 2014.

[93] A. Gleiter. *Mess-und Auswertemethoden für die dynamische Thermografie.* PhD thesis, Universität Stuttgart, 2011.

[94] R. Yang, Y. He, B. Gao, and G.Y. Tian. Inductive pulsed phase thermography for reducing or enlarging the effect of surface emissivity variation. *Applied Physics Letters*, 105(18):184103, 2014.

[95] A. Salazar, L. Zamanillo, M. Colom, A. Mendioroz, U. Galietti, A. Sommier, J.C. Batsale, and C. Pradere. Lock-in thermography on moving samples: amazing mismatch between amplitude and phase. *Quantitative Infrared Thermography Journal*, pages 1–8, 2019.

[96] Y.G. Gurevich, G.N. Logvinov, G. Gerardo, and G.E. López. Physics of thermal waves in homogeneous and inhomogeneous (two-layer) samples. *International Journal of thermal sciences*, 42(1):63–69, 2003.

[97] A. Salazar. Energy propagation of thermal waves. *European journal of physics*, 27(6):1349, 2006.

[98] C.A. Bennett and R.R. Patty. Thermal wave interferometry: a potential application of the photoacoustic effect. *Applied Optics*, 21(1):49–54, 1982.

[99] S. Vedula. *Infrared thermography and ultrasonic inspection of adhesive bonded structures, Overview and validity.* PhD thesis, Clemson University, 2010.

[100] A. Rosencwaig and A. Gersho. Theory of the photoacoustic effect with solids. *Journal of Applied Physics*, 47(1):64–69, 1976.

[101] G. Pitarresi. Lock-in signal post-processing techniques in infra-red thermography for materials structural evaluation. *Experimental Mechanics*, 55(4):667–680, 2015.

[102] Iapetus (innovative repair of aerospace structures with curing optimization and life cycle monitoring abilities). Technical Report final report summary, july 2014.

[103] S. Schmid, U. Martens, W.K. Schomburg, and K.-U. Schröder. Integration of eddy current sensors into repair patches for fatigue reinforcement at rivet holes. *Strain*, page e12387, 2021.

[104] V. Tanulia, J. Wang, G.M. Pearce, A.A. Baker, M. David, B.G. Prusty, et al. Disbond growth assessment for bonded joints and patch repairs of primary airframe structures. *ICCM22 2019*, page 4655, 2019.

[105] A.A. Baker and J. Wang. Proposed through-life management approaches for adhesively bonded repair of primary structures. *International Journal of Adhesion and Adhesives*, 87:151–163, 2018.

[106] J. Wang, A.A. Baker, and P. Chang. Hybrid approaches for aircraft primary structure repairs. *Composite Structures*, 207:190–203, 2019.